

# Advances in Optics and Photonics

# Coherent interactions of free electrons and matter: toward tunable compact x-ray sources

AMNON BALANOV,<sup>1</sup> ALEXEY GORLACH,<sup>1</sup>
VLADIMIR BARYSHEVSKY,<sup>2</sup> ILYA FERANCHUK,<sup>3</sup> HIDEO NITTA,<sup>4</sup> YASUSHI HAYAKAWA,<sup>5</sup> ALEXANDER SHCHAGIN,<sup>6,7</sup> YUICHI TAKABAYASHI,<sup>8</sup> YARON DANON,<sup>9</sup> LIANG JIE WONG,<sup>10</sup> AND AND AND KAMINER<sup>1,\*</sup>

Received February 18, 2025; revised May 26, 2025; accepted May 28, 2025; published November 10, 2025

Compact laboratory-scale x-ray sources still rely on the same fundamental principles as did the first x-ray tubes developed more than a century ago. In recent years, significant research and development has focused on large-scale x-ray sources such as synchrotrons and free-electron lasers, leading to the generation of high-brightness coherent x-rays. However, the large size and high costs of such sources prevent their widespread use. The quest for a compact and coherent x-ray source has long been a critical objective in modern physics, gaining further importance in recent years for industrial applications and fundamental scientific research. Here, we review the physical mechanisms governing compact coherent x-ray generation. Of current interest are coherent periodic interactions of free electrons in crystalline materials, creating hard x-rays via a mechanism known as parametric x-ray radiation (PXR). Over the past decade, x-ray sources leveraging this mechanism have demonstrated state-of-the-art tunability, directionality, and broad spatial coherence, enabling x-ray phase-contrast imaging on a compact scale. The coming years are expected to show substantial miniaturization of compact x-ray sources, facilitated by progress in electron beam technologies. This review compares the most promising mechanisms used for hard x-ray generation, contrasting parametric x-ray radiation with inverse Compton scattering and characteristic radiation from a liquid-jet anode. We cover

<sup>&</sup>lt;sup>1</sup>Department of Electrical and Computer Engineering, Technion—Israel Institute of Technology, Haifa 3200003. Israel

<sup>&</sup>lt;sup>2</sup>Research Institute for Nuclear Problems of Belarusian State University Bobruiskaya Str. 11, 220030 Minsk, Belarus

<sup>&</sup>lt;sup>3</sup>Physics Department, Belarusian State University, Nezavisimosti Ave., 4, 220030, Minsk, Belarus

<sup>&</sup>lt;sup>4</sup>Department of Physics, Tokyo Gakugei University, Koganei, Tokyo 184, Japan

<sup>&</sup>lt;sup>5</sup>Laboratory for Electron Beam Research and Application, Nihon University, Narashinodai 7-24-1, Funabashi 274-8501, Japan

<sup>&</sup>lt;sup>6</sup>Deutsches Elektronen-Synchrotron DESY, Notkestr. 85, 22607 Hamburg, Germany

<sup>&</sup>lt;sup>7</sup>Kharkiv Institute of Physics and Technology, Academicheskaya 1, Kharkiv 61108, Ukraine

<sup>&</sup>lt;sup>8</sup>SAGA Light Source, 8-7 Yayoigaoka, Tosu, Saga 841-0005, Japan

<sup>&</sup>lt;sup>9</sup>Department of Mechanical, Aerospace, and Nuclear Engineering, Rensselaer Polytechnic Institute, Troy, New York 12180, USA

<sup>&</sup>lt;sup>10</sup>School of Electrical and Electronic Engineering, Nanyang Technological University, 50 Nanyang Ave., Singapore 639798, Singapore

<sup>\*</sup>kaminer@technion.ac.il

the most recent advancements, including the development of new materials, innovative geometrical designs, and specialized optimization techniques, aiming toward x-ray flux levels suitable for medical imaging and x-ray spectroscopy at compact scales. © 2025 Optica Publishing Group. All rights, including for text and data mining (TDM), Artificial Intelligence (AI) training, and similar technologies, are reserved.

# https://doi.org/10.1364/AOP.559742

1.		duction	
2.		view of Compact X-Ray Sources	
	2.1.	<b>8 1</b>	
		2.1.1. Classifications of X-Ray Sources by Interaction type	
		2.1.2. Scaling Laws and Spectral Range	
	2.2.	5	
		2.2.1. Comparing X-Ray Sources by Their Brightness	
		2.2.2. Why Brightness Is Not Necessarily the Relevant Metric	736
	2.3.	Search for a Compact and Coherent Source of Hard X-Rays	736
		2.3.1. Challenge of Lasing in the X-Ray Spectrum	736
		2.3.2. Coherent Interactions of Free Electrons with Matter	737
3.	Back	ground on Parametric X-Ray Radiation	738
	3.1.	Basic Mechanism and Motivation for Parametric X-Ray Radiation	738
	3.2.	Milestones in the Development of Parametric X-Ray Radiation	740
	3.3.	Applications of Parametric X-Ray Radiation	
		3.3.1. Applications of High-Coherence X-Ray Sources	
		3.3.2. Demonstration of Imaging Using Parametric X-Ray Radiation	
	3.4.	Fundamentals of Parametric X-Ray Radiation	
		3.4.1. X-Ray Generation Mechanism	
		3.4.2. Dynamical and Kinematical Theories	
		3.4.3. Ultra-Relativistic Electron Beams	
		3.4.4. Moderately Relativistic Electron Beams	
	3.5.	Emission Characteristics of Parametric X-Ray Radiation	
	0.0.	3.5.1. Density Effect in PXR	
		3.5.2. Dispersion and Angular Distribution of PXR	
		3.5.3. Polarization of PXR	
		3.5.4. Main contributions to the radiation yield of PXR	
4	Rece	nt Developments Toward Practical Applications	
т.	4.1.	Progress in PXR Relying on High-Quality Electron Beam Sources	
	т.1.	4.1.1. Effect of Heat Load	
		4.1.2. Requirements from the Electron Beam Source	
	4.2.	Progress in PXR Relying on Material and Geometry Design	
	7.2.	4.2.1. The Challenge of X-Ray Self-Absorption	
		4.2.2. Challenge of Electron Beam Scattering	754
		4.2.3. Overcoming the Challenges by Optimizing the Crystal	134
			756
		Geometry	
_	D 1	4.2.4. Resulting Optimal X-Ray Flux	
5.		map Toward a Compact X-Ray Source	
	5.1.	Design of the Hard X-Ray Source	
	5.2.	System Performance and X-Ray Source Characteristics	/60
		5.2.1. Effects of Geometry and Electron Beam Quality on the	<b>-</b>
		X-Ray Linewidth	760

# Coherent interactions of free electrons and matter: toward tunable compact x-ray sources

AMNON BALANOV, ALEXEY GORLACH, VLADIMIR BARYSHEVSKY, ILYA FERANCHUK, HIDEO NITTA, YASUSHI HAYAKAWA, ALEXANDER SHCHAGIN, YUICHI TAKABAYASHI, YARON DANON, LIANG JIE WONG, AND IDO KAMINER

# 1. INTRODUCTION

Since the discovery of x-ray radiation by Wilhelm Röntgen in 1895 [1], x-rays have revolutionized modern science and played a central role in many commercial and scientific applications. X-rays had a major impact on a wide range of fields, including medical imaging, biology, material science, environmental and earth science, astrophysics, homeland security, and industrial inspection. Indeed, x-ray science is responsible for numerous Nobel prizes in physics, chemistry, and medicine. A list of just part of the physics awards includes the 1901 award to Wilhelm Röntgen for the discovery of x-ray radiation, the 1914 award to Max von Laue for the discovery of x-ray diffraction by crystals, the 1915 award to William and Lawrence Bragg for the development of x-ray crystallography, the 1917 award to Charles Glover Barkla for the discovery of characteristic x-ray of elements, and the 1924 award to Karl Manne Georg Siegbahn for the discovery of the x-ray spectroscopy. It is quite remarkable that most of these discoveries were made using relatively simple sources of hard x-rays based on Röntgen's compact x-ray tube. Notable exceptions include experiments using x-rays from radioactive elements and measurements of x-rays originating from astronomical phenomena in deep space.

Over the past decades, x-ray science has evolved along two distinct paths separated by the types and scales of x-ray sources: large-scale x-ray facilities vs. compact x-ray sources. Synchrotrons and free-electron laser (FEL) facilities, which represent the pinnacle of x-ray technology, provide coherent, tunable hard x-rays with high flux and exceptional beam quality [2,3]. However, these facilities have significant draw-backs, including immense space requirements, high energy consumption, extensive safety measures, and limited accessibility, owing to their scale and cost. In contrast, compact x-ray sources have primarily relied on x-ray tubes, which are widely available and relatively inexpensive but emit isotropic and broadband radiation, lacking the energy tunability and coherence required for many advanced applications. This contrast has driven ongoing research efforts toward novel compact mechanisms of x-ray generation that achieve the coherence and tunability of large-scale facilities without their associated drawbacks.

Overview of coherent x-ray generation at compact scales

The leading mechanisms for compact x-ray sources include high-harmonic generation [4–16], laser-plasma accelerators [17–28], inverse Compton scattering [29–34], radioactive elements, and mechanisms based on the coherent interaction between free electrons and matter. The latter include Cherenkov radiation, Smith–Purcell radiation, channeling radiation, coherent Bremsstrahlung, transition radiation, and parametric x-ray radiation [35,36]. Unlike the conventional x-ray tube, which is broadband and

isotropic, these compact mechanisms offer varying degrees of coherence, flux, and energy tunability. However, they also introduce additional operational complexities, such as precision requirements, shielding considerations, and practical implementation challenges.

The field of compact x-ray science is constantly evolving, with recent years witnessing the emergence of new concepts and mechanisms for x-ray generation. Novel mechanisms include free-electron interactions with graphene surface plasmons, magnetic nanoundulators, metasurfaces, and metamaterials [37–43]. Improved designs of free-electron sources also rely on advanced materials such as carbon nanotubes [44]. Advances in high-intensity pulsed lasers have inspired proposals for laser-undulators of electrons, both in vacuum and in tailored photonic waveguides [45–53]. In the realm of quantum electrodynamics and quantum optics, innovative theoretical proposals include the manipulation of vacuum fluctuations and engineering electron wavefunctions to enhance x-ray generation [54–59]. Recently, parallel efforts showcased pioneering experimental studies of x-ray generation at compact scales that now rely on the precision of electron microscopes, exploring novel structures such as van der Waals materials as electron undulators [60–62]. Contemporary experiments in the optical domain inspired new concepts for x-ray generation, such as Smith–Purcell lenses [63] and radiation enhancement based on photonic crystal flatbands [64].

# Need for compact sources of hard x-rays

Many of these ongoing efforts focus on the generation of *hard* x-rays. A directional hard x-ray source with a narrow spectral linewidth would be highly advantageous for many applications, allowing a significant radiation dose reduction [65]. For example, mammographic examinations using nearly mono-energetic x-rays can reduce the radiation dose by a factor of 10 to 15 compared to conventional x-ray systems [66]. Similar dose reduction estimations apply for angiography and other radiographic studies [66].

Currently, three leading mechanisms show strong potential for producing compact *hard* x-ray sources with adequate coherence and flux for imaging applications: parametric x-ray radiation (PXR), inverse Compton scattering (ICS), and characteristic radiation from liquid jets [67–69], as detailed below. These mechanisms have been analyzed and developed for practical applications in medicine, homeland security, and materials science [68,70–72].

Apart from the practical applications of compact x-ray science, compact x-ray sources have been increasingly used as platforms to explore fundamental science. This type of research is particularly prominent with PXR, which has been employed to study the interaction of free electrons with emerging nanomaterials such as van der Waals layered structures [60–62,73,74], of novel compositions such as WSe<sub>2</sub>, FePS<sub>3</sub>, and NiPS<sub>3</sub> [61,75]. Most recently, quantum recoil effects in electron radiation, which have been debated and analyzed for many decades [76–80], were first demonstrated experimentally using the PXR platform [81,82], proving the viability of these effects for any electron-radiation process.

The goal of this review is to examine the underlying physics of the modern coherent sources of hard x-rays. We focus on the mechanism that has received substantial recent interest, parametric x-ray radiation, which is the prominent mechanism of x-ray generation by coherent interactions of free electrons with matter. Here, we review the physics associated with such interactions and the central mechanism by which they produce hard x-rays. The most recent reviews of this mechanism were conducted from 2001 [83] to 2005 [84]. We specifically highlight the advances made since then, as the field has made substantial progress in the last decade. Below, we present the state-of-the-art science and applications emerging from this field and build a comprehensive

comparison between these mechanisms and other leading mechanisms for the compact generation of hard x-rays.

This review provides an entry point to the broader field of x-ray science and its frontier challenges. It serves the wider community interested in compact, tunable, and directional x-ray sources for different applications and broadens the scope of PXR phenomena, introducing new materials and innovative experimental platforms.

# 2. OVERVIEW OF COMPACT X-RAY SOURCES

This section reviews the mechanisms of x-ray generation at a compact scale. Section 3 focuses on x-ray generation via the coherent interaction of free electrons with matter, and Section 4 highlights the most recent advances. Based on these recent advances, Section 5 draws a roadmap for where the field goes next, toward the realization of a compact source of hard x-rays with sufficient coherence and flux. Section 6 compares the different mechanisms of compact x-ray generation, emphasizing their relative advantages for specific use cases. We conclude the review with an outlook in Section 7.

Most of the mechanisms for producing x-rays rely on energetic free electrons. The term "free electrons" has been widely adopted to characterize a beam of electrons after an initial acceleration stage. Throughout the text, "free electrons" serves as an umbrella term that encompasses equivalent expressions found in diverse scientific literature, including "accelerated electrons," "fast electrons," "relativistic electrons," or "swift electrons." Despite the designation "free," these electrons often undergo interactions with various media or with external electromagnetic fields.

# 2.1. Overview of Mechanisms for Generating X-Rays

# 2.1.1. Classifications of X-Ray Sources by Interaction type

x-ray sources differ in their emission spectrum, power, flux, brightness, size, and cost. They can be classified by four interaction types, as illustrated in Fig. 1 (not accounting for radiation based on nuclear radioactive decay that typically emits gamma rays): (1) Sources based on the incoherent interaction between free electrons and matter, such as bremsstrahlung emitted from an x-ray tube. (2) Sources based on the coherent interaction between free electrons and matter. (3) Sources based on the interaction between free electrons and external electromagnetic (EM) fields. (4) Sources based on the interaction between strong laser fields and matter. This classification, along with descriptions of the different physical mechanisms related to each group and the relevant metrics for comparison, is summarized below.

Sources based on incoherent interaction between free electrons and matter

This group includes the x-ray tube, where electrons emitted from a cathode accelerate and impact a target anode, leading to two central emission processes, both of which rely on local electron interactions with matter that destroy electron coherence: bremsstrahlung and characteristic x-ray radiation. The resulting emission is isotropic and has a broadband spectrum with a few sharp lines produced by the characteristic radiation. Although operationally simple, with low electron energies and relaxed radiation shielding requirements, its isotropic and broadband emission limits the source brightness and the energy tunability.

Sources based on free-electron interaction with an external electromagnetic (EM) field

This group contains synchrotrons, free-electron lasers (FELs) [3,85], and ICS [31,32], all of which rely on periodic electron undulation by external EM fields. In the

#### Figure 1 Sources based on incoherent interaction between Sources based on coherent interaction free electrons and matter (the X-ray tube) between free electrons and matter Exit Window Conventional-anode Cherenkov radiation Rotating-anode Cathode Transition radiation Liquid-jet anode Channeling radiation Coherent Bremsstrahlung Emission mechanisms Electron Anode Smith-Purcell (\*\*) Bremsstrahlung Source Parametric X-ray (\*\*) Periodic Characteristic radiation Structure ~100kV Sources based on interaction Sources based on free-electron interaction with EM fields between laser light and matter Electron bunch Free-electron laser Magnetic High harmonic generation Laser plasma accelerators (LPA) Inverse Compton scattering X-ray plasma lasers Betatron Relativistic flying mirrors Gas \ Plasma

Physical processes for producing x-rays: classification by interaction types. (1) Sources based on the incoherent interaction between free electrons and matter, such as bremsstrahlung emitted from an x-ray tube. (2) Sources based on the coherent interaction between free electrons and matter. (3) Sources based on the interaction between free electrons and an external electromagnetic (EM) field. (4) Sources based on the interaction between strong laser fields and matter.

synchrotron and FEL facilities, this undulation is achieved using low-frequency magnetic undulators, whereas ICS schemes utilize an intense counter-propagating laser beam to undulate the electron [32]. Synchrotron and FEL facilities produce extremely high brightness beams owing to the temporal coherence [86], with FEL reaching even higher brightness through collective emission from microbunched electron beams.

On the frontier of x-ray quantum optics, recent studies predicted that x-ray FELs (XFELs) can generate entangled photon pairs [87] and cat-states of x-rays [88] through coherent emission mechanisms, achieving greater efficiency and tunability than traditional x-ray parametric down-conversion [89–92]. Similar mechanisms have been explored in the terahertz range [93], enabling novel quantum sensing applications and positioning FELs as versatile sources for quantum optics across a broad spectral range.

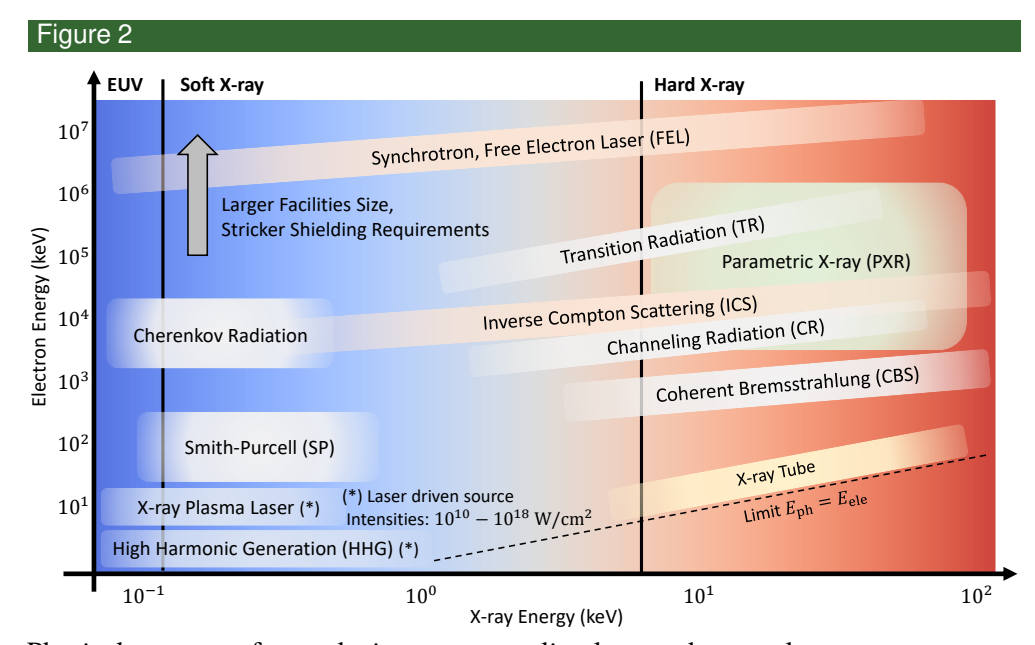
Despite their capabilities, Synchrotron and XFEL sources are limited by their large size and high cost. Recent proposals for compact x-ray sources include XFEL oscillators [94–97] and FELs driven by optical undulators [98–102].

Sources based on coherent interaction between free electrons and matter

This group is based on extended free-electron interactions with matter in a manner that maintains electron coherence throughout its interaction, as in Cherenkov radiation [103,104], transition radiation [105], diffracted transition radiation [106,107], transition x-ray radiation from a stack of foils [36], channeling radiation [108–110], coherent bremsstrahlung [111], Smith–Purcell radiation, and PXR. While some of these mechanisms are promising for producing quasi-coherent directional x-rays with tunable energy, they are currently limited by heat dissipation, self-absorption of the emitted photons in matter, and electron scattering. In Section 4, we describe recent techniques for mitigating these limitations.

Sources based on an interaction between intense laser light and matter

This group relies on external high-intensity laser pulses interacting with matter to produce x-rays [112] and includes high harmonic generation (HHG) [8,10], relativistic



Physical processes for producing x-rays: scaling laws and spectral range.

flying mirrors [19], and plasma-based x-ray lasers [113]. While these sources can produce coherent beams, most of them are limited to soft x-rays: The HHG spectra are restricted by a cut-off typically reaching up to several hundredths of eVs and rarely to a few keVs [11]. The x-ray plasma laser extension to hard x-rays (>10 keV) is challenging due to the short radiative lifetime (estimated transition times ~1 fs ×  $\lambda_x^2$ , where  $\lambda_x$  is the wavelength in angstrom [114]), which requires extremely high pumping intensities. An additional source related to this group is the laser-plasma accelerator, which is described below.

#### 2.1.2. Scaling Laws and Spectral Range

The energy scaling of different x-ray sources unveils a fascinating interplay between the emitted x-ray energy and the energy of the electrons, each governed by distinctive physical characteristics that shape their behavior. We focus on five representative physical processes. Figure 2 provides an overview of the scaling laws and spectral ranges associated with these different x-ray generation processes.

*Undulation mechanisms (synchrotron, free-electron laser, inverse Compton scattering, and coherent bremsstrahlung)* 

In these sources, the emitted x-ray wavelength scales quadratically with the electron energy,  $\lambda_x \propto \lambda_u \cdot \gamma_e^{-2}$ , where  $\lambda_u$  is the undulation period and  $\gamma_e$  is the Lorentz factor. These sources differ in their undulation period: centimeter-scale ( $\lambda_u \sim 1$  cm) for synchrotron and FEL facilities, micrometer-scale arising from the laser wavelength ( $\lambda_u \sim 1-10\,\mu\text{m}$ ) for ICS, and angstrom-scale determined by the crystal lattice ( $\lambda_u \sim 1$  Å) for coherent bremsstrahlung. Thus, ICS and coherent bremsstrahlung require lower electron energies to achieve the same emitted x-ray energy, compared with synchrotron and FEL facilities. However, this advantage comes at the cost of lower brightness.

# Transition radiation

Transition radiation is generated when a charged particle passes through an interface between two different media [115]. While the transition radiation intensity is maximal

in the optical range, its spectrum extends to short wavelengths  $\lambda_x \approx \frac{2\pi c}{\omega_p \gamma_e}$ , where  $\omega_p$  is the plasma oscillation frequency. The linear dependence on the electron Lorentz factor implies that high electron energies are required to produce x-rays.

# Parametric x-ray radiation

For relativistic electron beams, PXR emission energy is almost independent of the electron energy but depends on the crystal properties and the emission angle. This independence allows the production of PXR at the hard x-ray spectrum even with 10 MeV electron energies, relaxing the requirements on the electron source.

# Channeling radiation

Channeling radiation is associated with free electrons passing through a crystal while becoming bounded transversely to the crystal potential [108]. Confined within the lattice potential well, the emitted photon energy depends on the transition energy between two bound eigenstates of the crystal potential, leading to emission with a wavelength dependence of  $\lambda_x \propto \gamma_e^{-\alpha}$ , where  $\alpha$  is typically between 1.5 and 2, depending on the crystal potential (e.g.,  $\alpha \approx 1.7$  for diamond) [110]. We note that a similar configuration also describes coherent bremsstrahlung and PXR; however, the physical process is fundamentally different: electrons pass through the crystal without being bound to its transverse potential and interact longitudinally, resulting in completely different energy-scaling laws.

# Soft x-ray Cherenkov radiation

Cherenkov radiation is emitted by a charged particle when its velocity in a medium with a refractive index n exceeds the phase velocity of light (c/n) [115]. While Cherenkov radiation in the visible and ultraviolet spectra is well known, soft x-ray Cherenkov radiation has historically been excluded since the medium refractive index is generally lower than unity in the x-ray spectrum. However, at some inner-shell absorption edges, the refractive index exceeds unity, allowing the generation of Cherenkov radiation in a narrowband region [116]. The Cherenkov radiation in soft x-rays has been demonstrated up to emission energies of 1 keV [104].

# 2.2. Metrics and Scaling Laws of X-Ray Sources

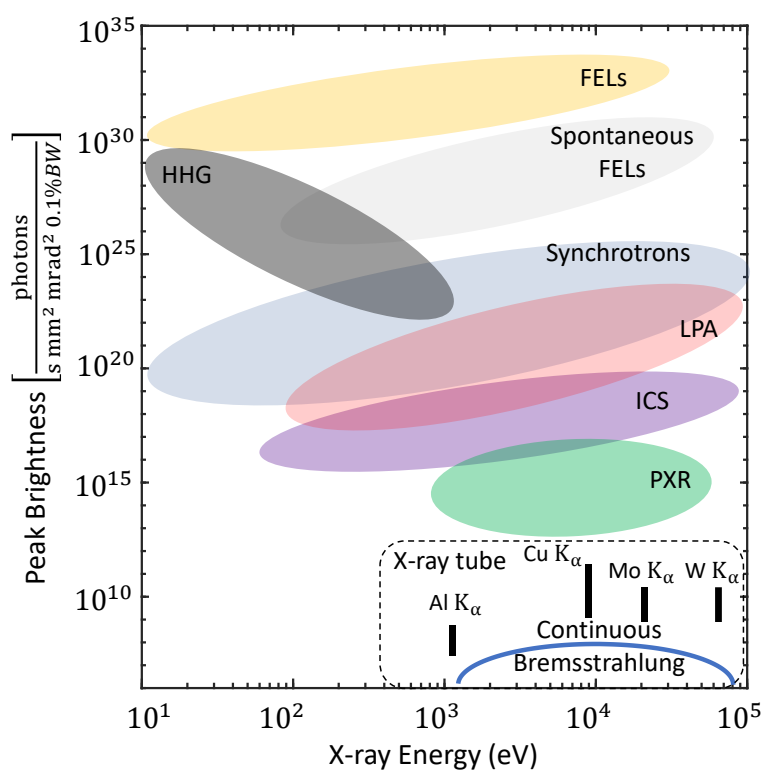
x-ray sources vary in size, beam quality, radiation shielding, safety features, and ease of operation. Among these, beam quality is generally the most significant factor for comparison. The central quality properties of the x-ray beam include the transverse coherence (beam emittance) and longitudinal coherence (beam spectral bandwidth). When evaluating x-ray source properties across different methods, it is useful to consider the spectral bandwidth, transverse coherence, and longitudinal coherence. These factors are combined into a single metric called brightness (also known as brilliance or spectral brilliance), which allows the comparison of x-ray beam quality from various sources.

The brightness for the source is defined as:

Brightness = 
$$\frac{\text{photons/second}}{(\text{mrad})^2 \text{ (mm}^2 \text{ source area) } (0.1\% \text{ BW})},$$
 (1)

where BW denotes the bandwidth. The brightness expression in Eq. (1) includes four terms. The first term denotes the number of photons emitted per second. The second term describes beam collimation, indicating the degree of divergence as the beam propagates, typically measured in milli-radians for both the horizontal and vertical directions. The third term addresses the source area's size; a smaller area allows the x-ray

Figure 3



Peak brightness of different x-ray sources. The comparison includes the synchrotron and free-electron-laser (FEL) facilities [2,94–97], high-harmonic-generation (HHG) [13,16,24], laser-plasma-accelerators (LPA) [22,27,28], inverse Compton scattering (ICS) [29–34], parametric x-ray radiation (PXR) [84], which can be produced up to energies a few hundred keV [159,192], and the x-ray tube [67–69]. The peak brightness is defined in Eq. (1). While the brightness metric is the common metric used for comparison between x-ray sources, it is not necessarily the relevant metric for some applications, such as medical imaging, which require a relatively large field of view.

beam to be focused to a correspondingly smaller image size, usually measured in  $mm^2$  units. The last term represents the spectral bandwidth. Some x-ray sources produce smooth spectra, while others produce peaks at specific photon energies. Therefore, when comparing sources, it is essential to consider the range of photon energies contributing to the measured intensity, which is often standardized to a fixed relative energy bandwidth (0.1% BW).

#### 2.2.1. Comparing X-Ray Sources by Their Brightness

Figure 3 compares the peak brightness of the different x-ray sources. The peak brightness metric represents the brightness in a single pulse. Brightness generally depends on the photon energy and varies significantly across different x-ray sources. For example, while HHG sources produce high peak brightness in the soft x-ray spectrum [13,16,24], their extension to the hard x-rays is challenging and limited. Third-generation undulators (synchrotrons) have a brightness approximately ten orders of magnitude higher than rotating anodes at the  $K\alpha$  line. XFELs achieve even higher peak brightness due to the transverse coherence resulting from coherent emission by microbunched electrons [3]. Further improvements are possible by XFEL oscillators, which have the potential to produce longitudinally coherent beams using narrow linewidth

mirrors based on x-ray monochromators [2,94–97,117,118]. This significant progress has led to a paradigm shift in experimental x-ray science, allowing experiments that were inconceivable only a few decades ago to be performed routinely.

Laser plasma accelerators (LPA) promise to deliver high-brightness x-ray beams in compact setups by accelerating electrons to relativistic energies through the interaction of intense laser pulses with plasma [21,22]. This interaction produces various x-ray radiation mechanisms, including Betatron radiation, Thomson backscattering, and Bremsstrahlung radiation [22,27,28]. Additionally, LPA-accelerated electrons can be injected into a conventional undulator [25]. However, the current limitations of LPAs for producing x-rays include limited flux, broadband energy spectrum, and limited repetition rate [21,22], which restrict their average brightness.

# 2.2.2. Why Brightness Is Not Necessarily the Relevant Metric

Despite brightness being a common metric, it is not universally suitable for all x-ray applications. Imaging applications, for instance, demand a higher x-ray beam flux, with less emphasis on beam emittance due to the necessity of a larger field of view. In contrast, for ultrafast dynamics, high-resolution x-ray spectroscopy, and diffraction applications, the brightness metric is more representative, given the analysis of small-dimension targets. While brightness characterizes the source quality for high-resolution applications, flux holds greater significance for imaging applications due to the advantageous larger field of view. Hence, the choice of beam quality metric should align with the target application. A detailed analysis and comparison between PXR, ICS, and the x-ray tube is presented in Section 6.

# 2.3. Search for a Compact and Coherent Source of Hard X-Rays

Despite the widespread use of laboratory-scale x-ray sources, the physical generation mechanisms remained relatively unchanged since the first x-ray tubes, where electrons emitted from a cathode accelerate and impact a target anode in a vacuum tube. The two main mechanisms in x-ray tubes are bremsstrahlung and characteristic x-ray radiation. The typical x-ray tube emission has a broadband spectrum due to the bremsstrahlung radiation, with a few sharp lines produced by the characteristic radiation. This spectrum depends mainly on the anode material and the applied acceleration voltage between the cathode and the anode [86]. Recent advances have increased x-ray tube brightness using micro-focus sources and liquid-jet anodes [67], enabling new applications in phase-contrast imaging and high-resolution diffraction [71,119]. Notwithstanding these advances, the fundamental limitations in the use of x-ray tubes remained the same, e.g., their low efficiency, broadband, and isotropic emission.

## 2.3.1. Challenge of Lasing in the X-Ray Spectrum

In the past decades, we have witnessed the rise of intense, tunable, and directional x-ray sources in the form of large, expensive synchrotron and free-electron laser facilities [3]. These facilities open the doors to the spectroscopy of material dynamics and biological processes by producing ultrashort x-ray pulses [120]. The coherence of such x-ray sources enables higher-resolution imaging through phase-contrast techniques and the next-generation security inspection of microchips [121]. However, the large size and expense of synchrotrons and free-electron lasers have hindered their widespread adoption in commercial and medical applications.

A long-standing fundamental question at the core of x-ray science is what prevents us from building x-ray lasers based on mechanisms similar to those used in conventional lasers in the visible and infrared spectra. Since the development of lasers in the infrared and visible spectral regions in the 1960s [122], there has been a continuous effort to

extend the generation of coherent electromagnetic radiation to shorter wavelengths, aiming for the x-ray spectrum. However, the conventional atom-based population inversion approach faces significant challenges when scaling to higher emission energies: (1) Shorter lifetimes of excited atom-core quantum energy levels: The radiative lifetime of an x-ray laser transition is estimated to be  $\sim 1 \text{ fs} \times \lambda_x^2$ , where  $\lambda_x$  is the wavelength in angstrom [114]. This extremely short lifetime poses a significant challenge for achieving population inversion. (2) The energy required for inner core excitation: The energy required for hard x-ray photon emission is at least four orders of magnitude larger than that required for optical photon emission. These two factors result in demanding requirements for the pumping powers necessary to achieve population inversion, which is a crucial condition for lasing action. Consequently, current x-ray sources based on classical population inversion are not widely accessible, except for some experimental attempts in the 1980s [123], and the ongoing efforts to use x-ray cavities based on crystal Bragg mirrors [124].

#### 2.3.2. Coherent Interactions of Free Electrons with Matter

What has emerged in recent years as an especially promising mechanism for hard x-ray generation on a compact scale is coherent electron interaction with matter, particularly the hallmark mechanism of PXR. The roots of this field date back to radiation effects in the optical spectrum, including the works of Cherenkov [125], Smith and Purcell [126], and Fainberg and Khizhnyak [127]. Concurrently, the interaction between high-energy electrons and *crystals* has been investigated since 1934 by von Weizsäcker and Williams [128]. The first coherent emission identified from this type of interaction was coherent bremsstrahlung, analyzed by Heitler [129] and Uberall [130], and channeling radiation, which was predicted theoretically by Kumakhov [131] in 1974, and observed experimentally by Terhune and Pantell [132] in 1975. Recently, it has been demonstrated that a charged particle moving in a channeling regime within a periodically bent crystal can produce undulator radiation with energies ranging from keV to MeV, depending on the crystal's bending period [133].

Within the group of sources based on the coherent interaction between free electrons and matter, PXR is one of the most promising mechanisms for producing a directional, monochromatic, linearly polarized, and tunable hard x-ray source at compact dimensions due to its high spectral yield and large field of view [134]. The desired characteristics of PXR are based on the coherent interaction of free electrons with crystals, arising from phase-matching with the periodic crystal structure [135]. PXR thus differs from the conventional x-ray emission mechanisms of bremsstrahlung and characteristic radiation by having the electron maintain its *coherence* during its interaction and emission. Although PXR has been investigated extensively over the decades, it remained limited in usage due to its low flux. For example, practical mammography imaging requires an x-ray beam flux of  $\sim 10^5 - 10^6 \frac{\text{photons}}{\text{s mm}^2}$ , yet the maximal flux achieved in recent PXR experiments is two orders of magnitude lower than this requirement [136].

In the next section, we review the advantages of PXR over other compact x-ray sources. We then explore the latest advancements in the PXR field that have led to significant improvements in flux levels (Section 4). These innovations have propelled PXR into the realm of viability for *in vivo* imaging applications, thereby opening new possibilities in medical diagnostics and research. Finally, we outline a roadmap detailing the steps necessary to achieve a fully realized PXR source (Section 5). This plan will serve as a guide for researchers and engineers, paving the way for implementing this cutting-edge technology for commercial use.

# 3. BACKGROUND ON PARAMETRIC X-RAY RADIATION

One of the most promising mechanisms for producing quasi-coherent and tunable hard x-rays at compact scales is PXR, which was demonstrated experimentally for the first time in 1985 [137]. The last comprehensive reviews of PXR were conducted two decades ago [83,84], but the field has seen a significant revival since then, with fundamental experimental discoveries, refined theoretical models, and new applications [81,82,138–145]. Significant engineering progress has been made toward realizing a compact implementation of the PXR mechanism [145,146]. Of particular importance are x-ray phase-contrast imaging applications, which have been demonstrated using PXR [136,147–149]. These experiments were conducted in large facilities but proved the feasibility of implementing the PXR mechanism in compact setups for practical imaging applications.

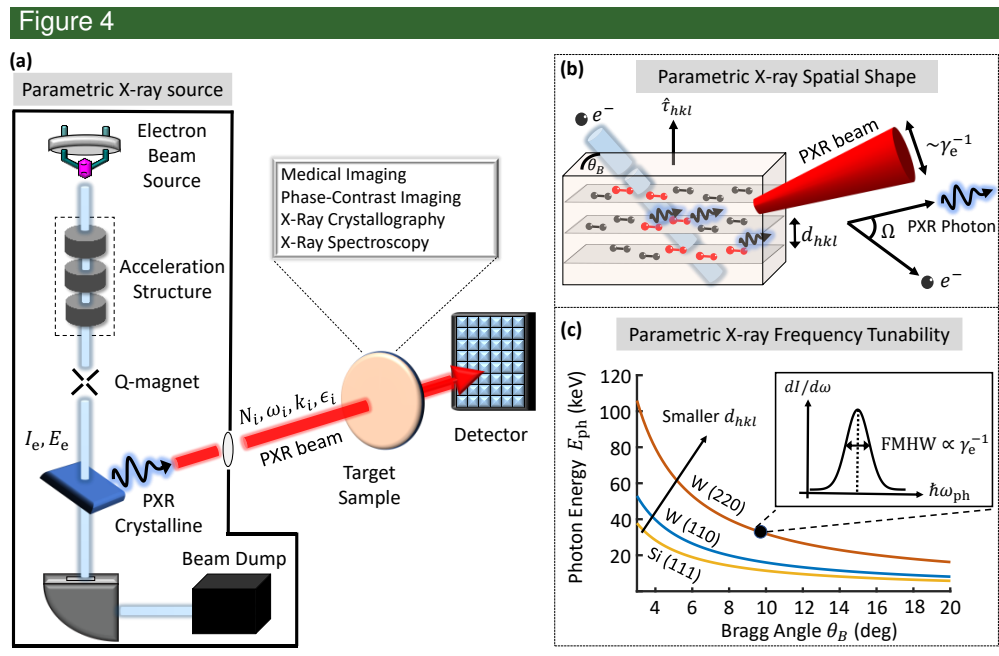
The next phase in the development of a viable, compact, and widespread PXR source for imaging applications has recently become possible due to three central factors: (1) Progress in synchrotron and FEL facilities promoted the miniaturization of relativistic electron acceleration structures that support high brightness, high repetition rate, and high-average current [31,150,151]. (2) Demonstration of PXR imaging applications, such as K-Edge imaging, phase-contrast imaging using differential-enhanced imaging, and computed tomography (CT) [136,147–149]. (3) Theoretical contributions discovered PXR geometries that resolved long-standing limitations and increased the spectral yield [152–155].

This section reviews the central aspects of PXR theory, focusing on its superior yield and beam quality in the x-ray spectrum compared to other electron—matter interaction processes. We begin with the fundamental properties and present the kinematical and dynamical theory of PXR, followed by a discussion of its emission properties, including spatial dispersion, polarization, yield, diffraction efficiency, and spectral linewidth. We also address unique aspects of free-electron interaction with matter, such as electron scattering effects, thermal load on the target crystal, and self-absorption of emitted PXR photons. While PXR is the primary focus of this review, the insights and advancements discussed apply to the other x-ray sources based on coherent electron—matter interactions.

#### 3.1. Basic Mechanism and Motivation for Parametric X-Ray Radiation

PXR is produced by the interaction between relativistic electrons and a periodic crystalline structure (Fig. 4) [84]. It possesses several desirable properties that can serve various applications. (1) The x-ray spectrum has a narrow linewidth, i.e., it is quasimonochromatic. (2) The x-ray photon energy can be tuned by crystal orientation, composition, and strain. (3) The x-ray photon energy is practically independent of the incident electron energy in the relativistic regime. (4) The x-ray beam has low spatial divergence, which is inversely proportional to the incident electron energy ( $\gamma_e^{-1}$ ) for a wide range of parameters (see Section 3.5.1) [156].

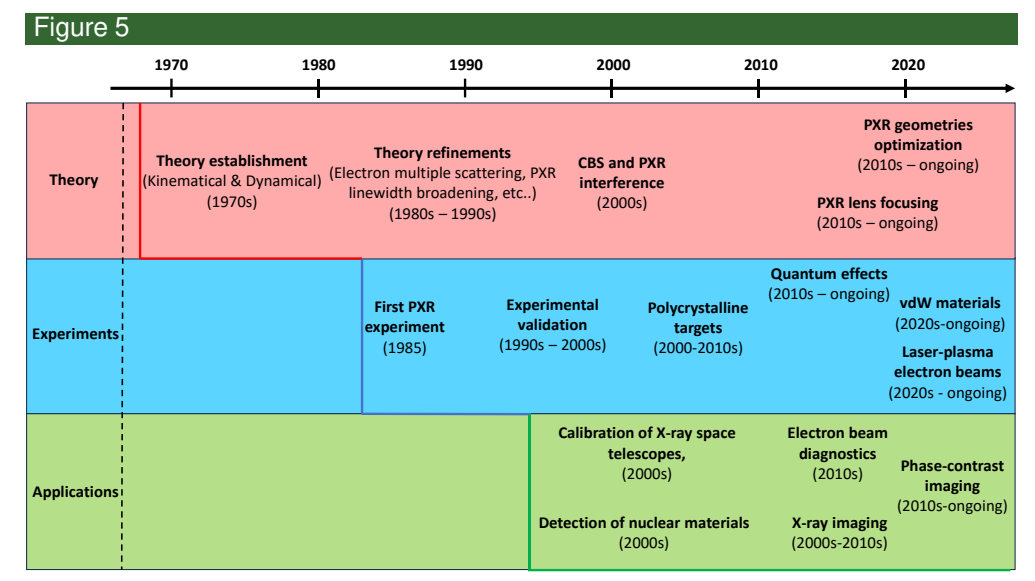
Compared to other x-ray sources based on interactions with free electrons, such as transition radiation and synchrotron radiation, hard x-ray generation from PXR requires a much lower electron-beam energy. For example, to produce 10 keV x-ray photons, synchrotron sources require electron beam energy of a few GeV, while transition radiation requires a few hundredths MeV (Fig. 2). PXR, on the other hand, occurs even at energies below 10 MeV [140,157]. This advantage is directly attributed to the nanoscale and sub-nanoscale periodicities encountered by the electron in the PXR scheme, as opposed to the centimeter scale periodicities typically found in traditional undulators. The low electron energy makes the PXR source considerably more compact and less



Parametric x-ray (PXR) source: spatial shape and energy tunability. (a), (b) PXR source scheme. A collimated electron source beam impacts a crystal and induces polarization currents on the target material atoms. Each excited atom can be treated as a radiating dipole. When the Bragg condition of constructive interference between the dipoles array holds, an intense, directional, and quasi-monochromatic x-ray beam is emitted at a faraway angle from the electron velocity direction. (b) The PXR spatial emission. The incident electron beam impacts the crystal Bragg plane  $\hat{\tau}$  with an angle  $\theta_B$ . The PXR photon is produced with an angle  $\Omega$  relative to the electron trajectory. The Bragg condition holds for  $\Omega = 2\theta_B$ . The PXR photons are emitted within an angular divergence of  $\theta_{\rm ph}^2 = \gamma_{\rm e}^{-2} + \left(\omega_p/\omega\right)^2$ , where  $\omega_p$  is the plasma frequency and  $\omega$  is the emission PXR frequency. For most applications of PXR,  $\gamma_{\rm e} \ll \omega/\omega_p$ , such that the beam divergence can be approximated by  $\theta_{\rm ph} \sim \gamma_{\rm e}^{-1}$ . (c) PXR frequency tunability. The PXR photon's energy is tuned by altering the Bragg angle and choosing the Bragg plane. When reducing the interplane distance  $d_{\rm hkl}$ , the emitted photon energy increases for a fixed Bragg angle. The typical spectral linewidth of the PXR can be as low as 1%.

expensive than the synchrotron sources. At higher electron energies, the PXR mechanism is still applicable, and indeed, tunable PXR was observed with photon energies up to 400 keV from electron beams of 1.2 GeV [158,159].

The PXR source spectral yield (i.e., the average number of photons produced per electron) is up to four orders of magnitude greater than that of other x-ray sources, such as bremsstrahlung, transition radiation, and coherent bremsstrahlung [134]. The PXR emission spectral linewidth is narrow and proportional to  $\propto \gamma_e^{-1}$  at moderate and high electron energies, making it suitable for phase-imaging applications [160]. In contrast, coherent bremsstrahlung and channeling radiation have a much higher spectral linewidth [36]. The linewidth of these sources is inversely proportional to the number of undulation periods. Since the electron energies required for these sources in the x-ray spectrum are below a few tens of MeV (Fig. 2), the electron scattering in the crystal is significant, limiting the number of effective undulation periods to the order of 10 (i.e., their linewidth is 10%) [36].



Timeline of developments in the field of parametric x-ray radiation (PXR), from its inception to the most recent ongoing efforts.

Moreover, channeling radiation, coherent bremsstrahlung, and transition radiation are emitted in the forward direction, parallel to the direction of the electron velocity. If the target material is thick, the emitted photons are self-absorbed in the material, limiting the source yield. On the other hand, PXR emits at a large angle relative to the electron velocity, enabling tailored geometries where the self-absorption effects are less considerable. In addition, the large emission angle eliminates the need for a strong magnetic field to separate the electrons from the x-rays and minimizes the bremsstrahlung background radiation.

Except for the energy tunability by crystal rotation, the PXR radiation has other characteristics that make it a promising physical mechanism for a compact x-ray source. The PXR emission is directional, polarized, and partially coherent, as discussed in the next section. Furthermore, its polarization and spatial shape can be designed and shaped (Fig. 8(a)) [161]. For instance, the PXR beam can have either a radial polarization with a circular shape peak or a linear polarization with a two-lobed shape, depending on the emission angle. The PXR spectrum is practically independent of the incident electron energy for relativistic electrons, enabling integration with high-energy-spread electron sources [75]. PXR radiation angle can be as large as 180 degrees (backscattering), and there are no theoretical limits for the energy of the incident electrons.

#### 3.2. Milestones in the Development of Parametric X-Ray Radiation

Figure 5 summarizes the main milestones in the development of PXR since the theory's establishment at the beginning of the 1970s [162–167]. After the first observation of PXR in 1985 [137,168], its basic mechanism was tested and analyzed experimentally, leading to additional refinements of the theory in the 1990s and the 2000s [83,139,142,169–181]. Since the beginning of the 2000s, the focus has shifted to PXR applications, especially for x-ray imaging [149,182–187] (Table 1 and Fig. 6), as well as for pulsed PXR sources [188], electron beam diagnostics [106,189,190], PXR lens focusing by bending crystals [73,74,191], calibration of x-ray space telescopes [192], detection of nuclear materials [193], and measurement of the crystalline grains size in polycrystals [194].

Table 1. PXR Experiments for Imaging Applications<sup>a</sup>

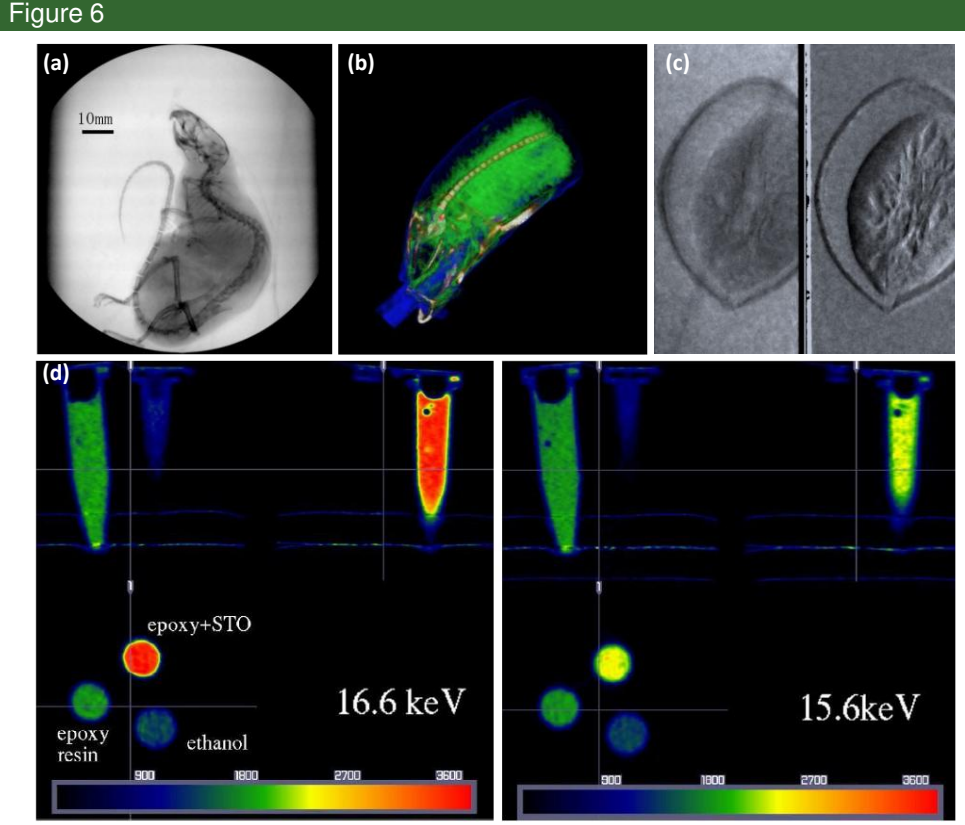
	3 3 11						
	Parameter	Hayakawa <i>et al</i> . [160,187]	Sones et al. [182–184]				
	Year	2004-current	2002–2009				
General	Facility	LEBRA, Nihon University	Rensselaer Polytechnic Institute				
	Energy	100 MeV	56 MeV				
	Energy spread	≤ 1%	≤ 15%				
	Electron pulse duration	4–5 μs	30 ns				
Electron	Peak current	120–135 mA	1.5 A				
source	Repetition rate	2–5 Hz	400 Hz				
	Average beam current	1–5 μΑ	0.01–6 μΑ				
	Normalized emittance	$\sim$ 15 $\pi$ mm mrad	Not reported				
	Electron beam size on target (diameter)	0.5–2 mm	~1 cm				
	Materials	Silicon	Lithium fluoride (LiF)				
Target	Thickness	200 μm	500 μm				
crystal	Geometry	Bragg/Laue	Bragg/Laue				
	Bragg angle	5.5° – 30°	15°				
X-ray	Photon energy	Si (111): 4–20 keV Si (220): 6.5–34 keV	6–35 keV				
photon	Total X-ray photon rate (photons/s)	~10 <sup>7</sup>	~106				
	Distance from PXR source	~10 m	~3 m				
Target sample	Beam diameter on target	~100 mm	~3 mm				
	Total X-ray photon flux (photons/mm <sup>2</sup> /s)	$\sim 10^3$	~75				

<sup>&</sup>lt;sup>a</sup>The electron source, target crystal, x-ray emission spectrum, and target sample dimensions are compared.

The first experimental realization of PXR was performed in 1985 by Baryshevsky *et al.* [137,168] using a 900-MeV electron beam from the Tomsk synchrotron to produce a 6.96-keV PXR from a diamond crystal. Since then, numerous studies have been conducted to characterize PXR from different materials, such as: silicon (Si) [170], germanium (Ge) [195], molybdenum textured polycrystal (Mo) [196,197], highly oriented pyrolytic graphite (HOPG) [198–200], diamond [201], tungsten (W) [202], copper (Cu) [203], aluminum (Al) [204], lithium fluoride (LiF) [182,183], and gallium arsenide (GaAs) [205]. A detailed review of experiments conducted before 2005 can be found in [206]. Later years have also characterized PXR from novel materials such as various polycrystalline solids [140,207,208], multilayer x-ray mirrors [209], van-der-Waals materials [61,62], and even powders [141], instead of the traditional monocrystal bulk solids. An additional focus in the last years has been on optimizing the PXR geometry [152–155] and demonstrating quantum effects [81,82].

The earliest PXR experiments were conducted at synchrotron facilities using electron beams with energies in the hundreds of MeV range [137,168,170]. Subsequent studies employed linear accelerators operating with electron energies in the tens of MeV range [160,183,184,186,187,210]. More recently, PXR has been demonstrated using lower-quality electron beams generated by laser-plasma interactions, highlighting the potential of plasma-based electron sources [75]. Additionally, proof-of-concept experiments have been carried out with electron microscopes operating at energies from tens to hundreds of keV [60–62,82].

These recent theoretical and experimental contributions pave the way toward a compact PXR source, using moderate electron energies [61,211,212]. At lower energies, the interference between PXR and coherent bremsstrahlung becomes significant. However, the yield and brightness in these lower-energy regimes are significantly lower than those of PXR with relativistic electrons [211,212]. Consequently, sources aimed



Snapshots from PXR imaging experiments. (a) An absorbing x-ray image of a mouse was observed using a 25.5-keV PXR beam. (b) 3D tomography for a raw fish sample. The tomogram was reconstructed from 180 projection images using a 17.5-keV PXR beam. (c) Absorption-contrast (left) and phase-gradient (right) images from 34 keV PXR beam. (d) K-Edge subtraction CT image taken with 16.6 and 15.6 keV PXR beams. Panels (a)–(c) reprinted from Hayakawa *et al.*, J. Instrum. **8**, C08001 (2013) [136] © IOP Publishing. Reproduced with permission. All rights reserved. panel (d) reprinted from [148].

at x-ray applications (rather than fundamental demonstrations of novel concepts) focus on regimes of relativistic electrons, where PXR dominates over coherent bremsstrahlung. In the next section, we review the central aspects of PXR theory, the experimental progress, and recent application achievements of x-ray imaging.

#### 3.3. Applications of Parametric X-Ray Radiation

PXR is a prospective mechanism for producing quasi-coherent x-ray radiation. High-coherence x-ray sources are promising for numerous applications, ranging from medical imaging to high-spatial-resolution imaging of biological samples and nanocrystals. Figure 6 shows examples of snapshots from different PXR imaging experiments. The most notable applications are listed below.

# 3.3.1. Applications of High-Coherence X-Ray Sources

**Phase-contrast imaging** utilizes the phase shift that occurs during the x-ray transmission and scattering by an object [70]. Extracting the x-ray beam's phase shift enables the creation of high-contrast images, which is particularly beneficial for visualizing details in specimens with weak absorption contrast, such as soft tissues like lungs and breast tissue (Fig. 6(a)).

**K-edge imaging** enhances the element contrast by using the significant differences in the sample's photo-electric attenuation coefficient above the K absorption edge [213]. Monochromatic x-ray beams slightly below and above the K-edge produce two images with distinct intensity maps, facilitating the detection of fine structures and improving the overall image contrast (Fig. 6(d)).

Coherent diffraction imaging (CDI) is a powerful technique for reconstructing the high-resolution structures of samples [214]. CDI enables the extraction of both amplitude and phase information from non-crystalline samples, expanding the range of studied specimens to those that are impossible to crystallize, such as various biological samples [215], and provide valuable insights into the nanoscale and atomic structures of diverse materials.

Besides imaging applications, coherent x-ray sources can be beneficial for x-ray scattering and spectroscopy applications, such as small angle x-ray scattering (SAXS) [216], x-ray absorption spectroscopy (XAS), and x-ray absorption fine structure (XAFS) [217].

# 3.3.2. Demonstration of Imaging Using Parametric X-Ray Radiation

While the applications listed above operate optimally in the large and expensive synchrotron and FEL facilities, a substantial effort has been made to produce a compact, high-coherence x-ray source. In the last two decades, PXR sources have been demonstrated for imaging applications. Two laboratories have shown the PXR feasibility as a compact and tunable source for imaging—the first group is from Rensselaer Polytechnic Institute (RPI) (2002–2009) [182,183,203], and the second group is from LEBRA, Nihon University, which has been active since 2004 [149,185–187].

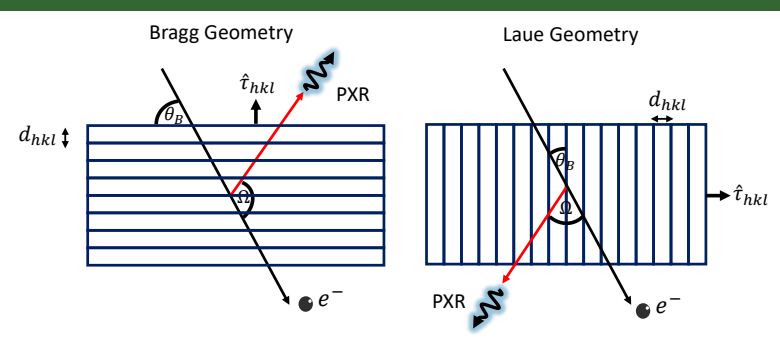
In these studies, images capturing the absorption of computer chips and animals were obtained (Fig. 6(a)). Furthermore, experiments demonstrated phase-contrast imaging (Fig. 6(c)) and 3D tomography (Fig. 6(b)), successfully capturing K-Edge subtraction CT images (Fig. 6(d)) [148]. These results suggested that PXR has spatial coherence and is a suitable x-ray source for imaging. Despite the significant progress made in these experiments, they were still limited by the requirement for a long exposure time (tens of seconds) due to insufficient flux levels (Table 1).

#### 3.4. Fundamentals of Parametric X-Ray Radiation

PXR radiation occurs when a relativistic charged particle passes through an aligned crystal (Fig. 4). In this review, we discuss an electron source beam; however, other charged particles, such as protons, exhibit similar phenomena [143,218–221]. The PXR production mechanism has been studied since 1970 by Ter-Mikaelian [167,222], Baryshevsky and Feranchuk [163,166], and Garibyan and Yang [162,164]. The most immediate feature that made PXR stand out relative to other x-ray emission mechanisms was a sharp x-ray emission at a large angle relative to the electron motion direction. This large emission angle contrasts with other x-ray radiation sources, such as bremsstrahlung and transition radiation, that emit nearly parallel to the direction of the electron motion.

The PXR emission is also spatially narrow and confined to a cone shape that is inversely proportional to the Lorentz factor of the electron  $\gamma_e^{-1}$  at moderate electron energies (Fig. 4(b)). Baryshevsky and Feranchuk gave this radiation the name PXR by analogy to the optical radiation, considered by Fainberg and Khizhnyak [127], but additional names are also in use: dynamical radiation, resonance radiation, quasi-Cerenkov radiation, or dynamical Cerenkov radiation [172].

# Figure 7



Two configurations of parametric x-ray radiation (PXR): Bragg and Laue geometries. The electron beam impinges the crystal through the front surface and exits through the rear surface. In Bragg geometry, the PXR reflection is emitted from the front (top) surface of the crystal, while in Laue geometry, it is emitted from the rear (bottom) surface.

#### 3.4.1. X-Ray Generation Mechanism

Several equivalent descriptions exist for the PXR phenomenon. In one description, a collimated electron source beam impacts a crystal and induces polarization currents on the target material atoms. Each excited material atom acts as a radiating dipole. When the Bragg condition of constructive interference between the dipoles array holds, an intense, directional, and quasi-monochromatic x-ray beam is emitted at a large angle relative to the electron velocity direction (Fig. 4). The maximum PXR production occurs when two conditions are satisfied simultaneously: the Smith–Purcell condition for the dipoles parallel to the electron trajectory axis and the requirement of transverse plane dipoles' constructive interference [161,179].

An equivalent description of the PXR phenomenon is the diffraction of the electron's virtual photon field by an array of atoms in the crystal. The diffracted virtual photons appear as real photons at the Bragg angle corresponding to the diffraction of x-rays, i.e., the virtual photons diffract from the crystal planes in the same manner as real photons. The Bragg law governs the x-ray diffraction conditions and relates the photon energy, the interplane d-spacing between crystal planes, and the incident angle between the photons and the diffraction plane. Consequently, continuously tunable PXR production is possible with the rotation of the target crystal (Fig. 4(c)).

Two configurations are commonly employed for generating PXR, analogous to those used in x-ray crystallography: Bragg and Laue geometries (Fig. 7). The two configurations differ according to the direction of x-ray emission relative to the crystal "front" surface through which the electron enters the crystal. In Bragg geometry, the PXR reflection is emitted from the front surface of the crystal [149,160,185–187,223,224] (top in Fig. 7), whereas in Laue geometry, it is emitted from the rear surface [181,225] (bottom in Fig. 7). The change in the emission angle arises from the specific choice of families of crystallographic planes with which the electrons interact.

#### 3.4.2. Dynamical and Kinematical Theories

The theoretical framework of PXR can be divided into kinematical and dynamical theories (similar to the division in the x-ray diffraction theory [86,226]). The PXR dynamical theory was developed by Baryshevsky and Feranchuk [163,166], Garibyan and Yang [162,164], and Caticha [172,227] and considers all PXR multiple scattering effects, including refraction, extinction, and interference effects, which alter the shape and width of the PXR peaks. In contrast, the simplified kinematical theory

ignores these effects, as done in the description of Ter-Mikaelian [167,222], Feranchuk and Ivashin [169], and Nitta [171,173,174,177], and was recently rederived for heterostructures [161]. The kinematic theory is based on the framework of classical electrodynamics, while Nitta's work provided a quantum derivation that aligns with the classical predictions.

The dynamical theory of PXR extends the kinematic theory but is more challenging to apply in practice. Generally, the dynamical theory provides the most accurate predictions for the total radiation intensity. The differences between the dynamical and kinematic theories are most significant near the Bragg peaks, particularly in thick crystals, where refraction, extinction, and interference effects should be considered [228]. While the kinematical theory is valid for thin materials below the extinction length ( $L_{\rm ext} \sim 1 \, \mu \rm m$ ) [84], ongoing efforts aim to define the boundaries where the kinematic theory remains accurate [142,229]. Studying these boundary effects in specialized PXR setups like bent crystals is especially interesting, as they can cause Bragg and PXR peaks to overlap. This overlap challenges the assumptions of kinematic theory and may expose new resonances that only the dynamical theory can explain [230].

While more precise PXR experiments can help clarify these boundaries, extensive research during the 1990s and 2000s refined the PXR kinematic theory to better align with experimental results for thicker materials [183]. Consequently, the refined PXR kinematic theory has become the most commonly used in practice. Throughout this review, we will use this refined PXR kinematic theory.

#### 3.4.3. Ultra-Relativistic Electron Beams

The PXR emission energy is closely related to the Bragg law governing the diffraction of an incident x-ray beam from a crystal. The Bragg law relates the incident x-ray beam energy  $\hbar\omega_B$  and the Bragg angle  $\theta_B$  between the incident x-ray momentum vector and the reflective crystallographic plane [86]:

$$E_{\rm B} = \hbar \omega_{\rm B} = \frac{\pi \, \hbar c}{d_{\rm hkl}} \frac{1}{\sin \left(\theta_{\rm B}\right)},\tag{2}$$

where  $d_{hkl}$  is the d-spacing of the Bragg plane corresponding to Miller indices (hkl).

Similarly, the expression for the PXR emission energy as a function of the Bragg polar angle  $\theta_B$ , for ultra-relativistic electrons, can be derived from the energy and momentum conversation lows in a crystal [167]:

$$E_{\rm PXR} = \hbar \omega_{\rm B} = \frac{2\pi \, \hbar c}{d_{\rm hkl}} \frac{\sin \theta_{\rm B}}{1 - \sqrt{\epsilon} \, \beta \cos \Omega},$$
 (3)

where  $\beta = v/c$  is the normalized velocity of the electron ( $\beta \approx 1$  for ultra-relativistic electrons) and  $\epsilon$  is the constant part of the medium permittivity ( $\epsilon \approx 1$  for hard x-rays).  $\Omega$  is the emission polar angle of the PXR photons relative to the electron beam, with Bragg's law imposing practical phase matching satisfied at the polar angle  $\Omega = 2\theta_{\rm B}$ , around which the maximum PXR intensity is obtained. Equation (3) can be derived from Huygens' construction [181] and can be interpreted as the expression for a Doppler frequency in a medium [222,231].

Both Bragg diffraction (Eq. (2)) and PXR emission frequency (Eq. (3)) are obtained via phase-matching arguments. The Bragg diffraction considers an incident x-ray beam (i.e., an incident photon), while the PXR diffraction considers an electron moving at a constant velocity as the source of the electromagnetic field. This assumption of constant velocity is a common classical assumption that holds for a broad range of parameters, enabling us to reach analytical results. Thus, the Bragg law (Eq. (2)) and the PXR energy (Eq. (3)) are closely related: the Bragg frequency in Eq. (2) is

obtained for an incident x-ray beam corresponding to  $\beta \sqrt{\epsilon} = 1$  and an observation angle of  $\Omega = 2\theta_{\rm B}$ , rather than  $\beta\sqrt{\epsilon} < 1$  for the incident electrons. In other words, the constructive interference conditions for Bragg law and the PXR emission are similar, with the main difference being the slightly lower velocity of an incident electron compared to an x-ray photon. As a result, the Bragg frequency is slightly higher than the PXR frequency [142,232]. We note that Eq. (3) also holds for other types of radiation emitted from interaction of a fast charged particle with a periodic structure, such as coherent bremsstrahlung, transition radiation from stacked foils, and Smith-Purcell radiation [231]. Further details and comparison between the Bragg frequency and PXR frequency can be found in [170,181,225,232,233].

An additional constraint limits the azimuthal angle of the emission, arising from the transverse (relative to the electron motion direction) phase matching with the crystal lattice. For instance, in a hexagonal lattice, there is an azimuthal symmetry of  $\pi/3$  [161]. The emission is confined around discrete emission angles with an opening angle proportional to  $\propto \gamma_e^{-1}$  (at moderate and high incident electron energies), as shown in Fig. 4(b). This relation allows PXR energy tunability in experiments by rotating the PXR crystal, i.e., altering the  $\Omega$  and  $\theta_B$  angles [183]. In particular, the PXR photons' energy is almost independent of the incident electron energy for relativistic electrons with energies greater than 5 MeV. At these highly relativistic electron energies, the photon energy is determined solely by the spacing between the crystal planes and the experimental geometry that determines the angles.

#### 3.4.4. Moderately Relativistic Electron Beams

The first decades of PXR studies focused mostly on ultra-relativistic electron energies (a few tens of MeV and above) in synchrotrons, storage ring facilities, and linear accelerators. Recent years have shown a significant growing interest in moderate electron energies of only a few hundredths keV and even below, with PXR being observed down to a few tens of keV [60,62,73,82]. Such moderate electron beam energies would provide many opportunities, including compact electron sources with reduced source shielding requirements.

The expression for the PXR emission energy as a function of the polar angle, for moderately relativistic electrons, is similar to that in Eq. (3) [167]. Unlike the similarity of the polar-angle dependence, the other properties of PXR differ substantially from those of the ultra-relativistic regime. These properties include the emission spectrum, the spatial shape of the radiating beam, and the angular distribution. Specifically, the emission is not confined to discrete directions but spreads across a wide range of angles. This emission spread occurs because there are no phase-matching conditions imposed along the transverse plane (perpendicular to the electron motion direction). Another difference from the ultra-relativistic regime is that in the moderately relativistic regime, the interference between PXR and coherent bremsstrahlung (CBS) becomes considerable [211,212], as was studied and observed experimentally in [234,235].

The same polar-angle dependence of Eq. (3) applies to a wider family of electron radiation phenomena besides PXR, including coherent Bremsstrahlung and Smith-Purcell radiation [161]. The latter is emitted from electrons passing by a periodic optical structure and satisfying phase matching along their direction of motion. Smith-Purcell radiation was observed in the radiofrequency [236], optical [237], terahertz [238], and more recently ultraviolet [239] spectra; its analogy to PXR is characterized in [161]. This connection highlights the universality of PXR physics.

Interestingly, the quantum-recoil effects can cause deviations from Eq. (3) [240] for any of the mechanisms applied. This universal quantum effect was recently observed

for the first time using a PXR experiment [82], using electron energies of tens of keV. In this regime, the output x-ray energy deviates substantially from Eq. (3), allowing greater versatility in controlling the x-ray spectrum [82]. In this review, however, we focus on the regimes most prevalent in experiments, where Eq. (3) accurately predicts PXR.

# 3.5. Emission Characteristics of Parametric X-Ray Radiation

In this section, we present the PXR spatial shape, dispersion, polarization, and yield for different crystal materials. The PXR yield depends on several factors, including the target material, the crystal geometry, the diffraction efficiency, and the thermal load on the crystal. In the framework of the kinematical theory, the photon distribution emitted from a single electron is given by [180]

$$\frac{dN_{\rm PXR}}{d\theta_x d\theta_y} = \frac{\alpha}{4\pi} \frac{\omega_B}{c \sin^2 \theta_B} f_{\rm geo} \chi_g^2 e^{-2W} N\left(\theta_x, \theta_y\right), \tag{4}$$

where  $\alpha$  is the fine-structure constant,  $\omega_B$  is the emitted PXR photon energy, c is the speed of light,  $\theta_B$  is the Bragg angle,  $e^{-2W}$  is the Debye-Waller factor that captures thermal effects,  $\chi_g$  is the Fourier expansion of the electric susceptibility as a function of the reciprocal vector g, describing the diffraction efficiency (Eq. (7)),  $N\left(\theta_x,\theta_y\right)$  is the PXR angular dependence (Eq. (5)), and  $f_{\rm geo}$  is the geometrical factor that describes the self-absorption of the PXR photons during the emission process (Eq. (10)).

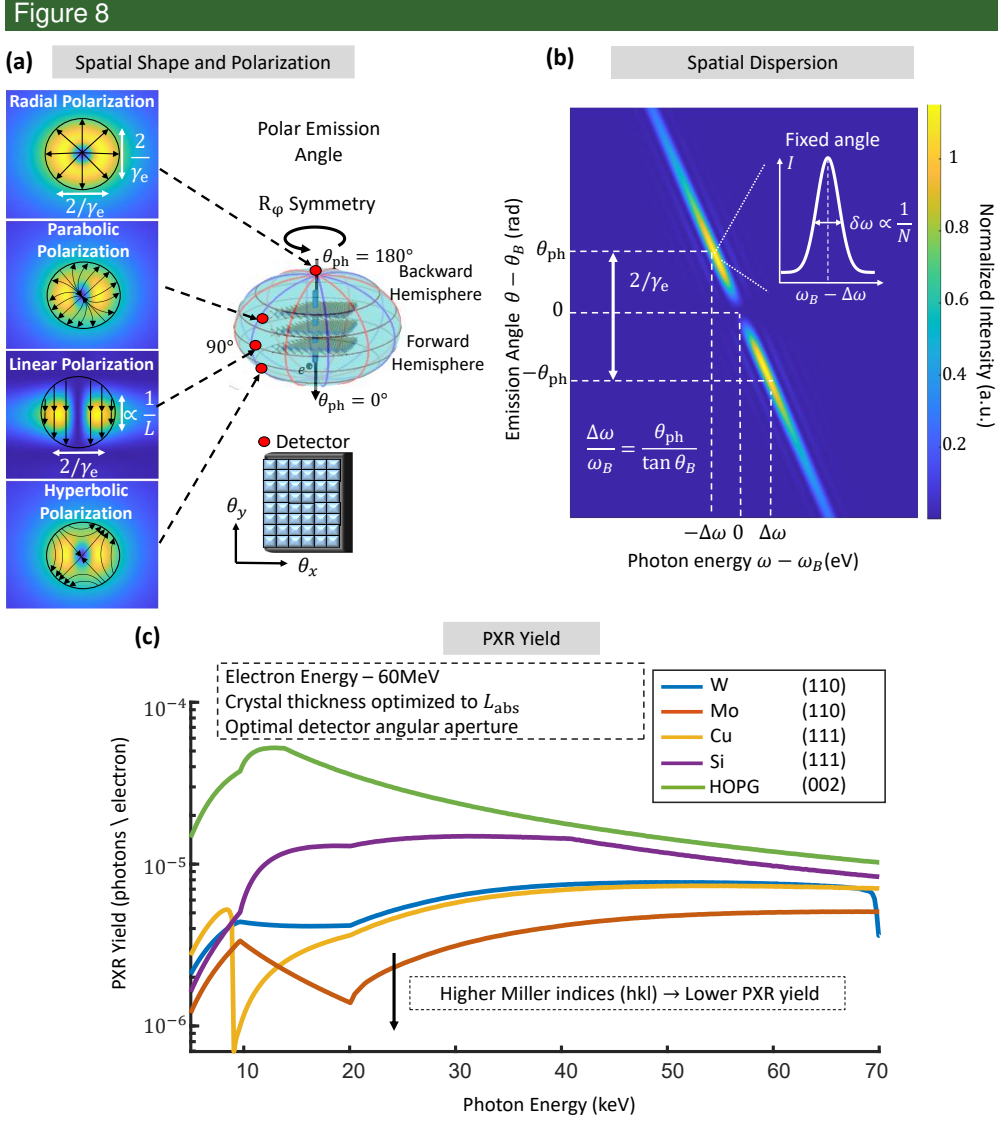
The PXR photon energy  $(\omega_B)$  and the Bragg angle are related by the condition for constructive interference between the material's dipoles (Eq. (3)). The PXR angular dependence  $N(\theta_x, \theta_y)$  is given by

$$N(\theta_x, \theta_y) = \frac{\theta_x^2 \cos^2(2\theta_B) + \theta_y^2}{\left(\theta_x^2 + \theta_y^2 + \theta_{ph}^2\right)^2},$$
 (5)

where  $\theta_x$  is the angle in the diffraction plane,  $\theta_y$  is the angle perpendicular to  $\theta_x$  in the diffraction plane, and  $\theta_{\rm ph}^2 = \gamma_{\rm e}^{-2} + \left(\omega_p/\omega\right)^2$ , where  $\omega_p$  is the plasma frequency of the material. Equations (4) and (5) describe the radiation yield for PXR emission near the resonant Bragg angles in both the forward and backward hemispheres; these near-Bragg conditions are the most favorable for efficient PXR. Studies on the PXR yield at large deviations from the Bragg angles are discussed in [233]. The specific shape of the PXR emission perpendicular to the incident electron velocity vector is detailed in [241]. Equation (5) describes the spatial profile in the diffraction plane, as shown in Fig. 8(a) for different Bragg angles.

# 3.5.1. Density Effect in PXR

The PXR angular dependence, described in Eq. (5), shows a saturation for electron energies exceeding  $\gamma_e \ge \omega/\omega_p$ . This saturation phenomenon, attributed to the density effect, arises owing to the corrections of PXR from ultra-relativistic particles [225,242]. Two central explanations exist for this phenomenon; both predict the same behavior. The first explanation is analogous to the Fermi density effect of ionization energy losses of a fast particle in a condensed medium. In dense media, numerous atoms lie between the incident electron and a far atom in the plane perpendicular to the electron trajectory. These atoms, influenced by the fast particle's fields, produce perturbing fields at the chosen atom's position, modifying its response to the fields of the fast electron. Essentially, each atom is affected by its neighbors, altering its polarizability relative to its free-space value [161]. A different approach for describing this phenomenon has been proposed in several studies and attributed to the Ter-Mikaelian longitudinal



Parametric x-ray angular distribution, polarization, spatial dispersion, and yield. (a) PXR spatial shape (i.e., angular distribution) and polarization. The PXR spatial shape, as described by Eq. (5), can be either a donut shape or a two-lobes shape, depending on the emission angle, whereas the polarization can be radial, linear, parabolic, or hyperbolic. The yield and polarization are shown for the forward and backward hemispheres, as well as for the perpendicular emission. (b) PXR spatial dispersion shape. The angular distribution emission width (HWHM) scales as  $\sim \gamma_e^{-1}$  at moderate and high impinging electron energies. This type of angular emission is often called PXR reflection [181]. The polar-angle dependence of the emitted energy is given by Eq. (3). When looking at a fixed emission angle, and at an ideal experimental resolution  $\Delta \theta_d = 0$ , the intrinsic spectral linewidth is proportional to  $\delta \omega / \omega \propto 1/N$ , where N is the number of crystallographic planes. (c) PXR yield for tungsten (W), molybdenum (Mo), copper (Cu), silicon (Si), and highly oriented pyrolytic graphite (HOPG), denoting the chosen d-spacing  $d_{\rm hkl}$  of each material. The calculation assumes an ultra-relativistic electron beam (60 MeV). The crystal thickness is optimized to the absorption length of each of the materials for each PXR energy. For smaller d-spacing, the yield decreases due to lower momentum transfer efficiency (Eq. (8)). The parameters of each material are presented in Table 2. The PXR yield is up to four orders of magnitude greater than other x-ray sources, such as bremsstrahlung, transition radiation, and coherent bremsstrahlung [134]. Panels (a) and (b) are adapted from [161].

density effect [156,167,225,242]. This approach explains the phenomenon using the formation length [222,243], and by the electromagnetic field modification of the particle in a medium, i.e., modification of the angular distribution of the virtual photons accompanying the particle in a medium [225,242].

The density effect impacts both the peak intensity and the angular divergence, setting an upper limit to these quantities, which does not change even with a further increase in electron acceleration energies. This effect is considerable for electrons with a Lorentz factor  $\gamma_e \ge \omega/\omega_p$ , resulting in a saturation of the intensity and beam divergence. Below, we focus on the regime in which the density effect is negligible, i.e., electron energies that satisfy  $1 \ll \gamma_e \ll \omega/\omega_p$ , leading to  $\theta_{\rm ph} \approx \gamma_e^{-1}$ .

# 3.5.2. Dispersion and Angular Distribution of PXR

In the PXR emission process, two energy linewidths are of primary interest. The first is the full PXR energy linewidth, commonly referred to as the total PXR reflection linewidth, and denoted by  $\Delta\omega/\omega$ . The second is the intrinsic PXR spectral linewidth, also called the spectral peak linewidth, represented by  $\delta\omega/\omega$  (see Fig. 8(b)). The full PXR energy linewidth,  $\Delta\omega/\omega$ , relates to the energy linewidth emitted from the entire reflection of the PXR across the entire angular opening of  $\propto \gamma_e^{-1}$ . In contrast, the intrinsic spectral linewidth,  $\delta\omega/\omega$ , represents the linewidth for a fixed (infinitesimal) emission angle. Due to the PXR's spatial dispersion, the intrinsic spectral linewidth  $\delta\omega/\omega$  is typically much narrower than the full PXR linewidth  $\Delta\omega/\omega$ . This section details the characteristics of both the full PXR linewidth and the intrinsic linewidth, analyzing the PXR dispersion and angular distribution near each resonant (Bragg) emission point.

The specific resonant points are governed by the Bragg conditions (Eq. (3)). The dispersion relationship in Eq. (3) enables extracting a relation of the angular spread and energy spread from the entire reflection region:

$$\frac{\Delta\omega}{\omega} = \frac{\Delta\theta_B}{\tan\theta_B},\tag{6}$$

where  $\Delta\theta_B$  is the angle deviation from the Bragg angle  $\theta_B$ , and  $\Delta\omega$  is the energy deviation from the Bragg energy  $\omega_B$  [163,170,244].

Figure 8(b) presents the PXR spatial dispersion around the resonant point  $\Omega = 2\theta_B$ . The PXR resonant energy  $(\omega_B)$  and resonant angle  $(\theta_B)$  are related by Eq. (3). The PXR emission has an angular opening of  $\sim 2\gamma_e^{-1}$ , where the peak intensity is located at an angle  $\theta_{\rm ph} = \pm \gamma_e^{-1}$  relative to the Bragg angle. Thus, the full PXR linewidth is  $\Delta \omega/\omega \sim \gamma_e^{-1}/\tan\theta_B$ . This angular distribution of the PXR yield is often called PXR reflection [181].

At the resonant point  $(\omega_B, \theta_B)$ , the emission intensity is zero because of symmetry considerations: an electron penetrating the target material excites the material dipoles symmetrically, causing the dipole fields to cancel each other at the resonant point [161]. Therefore, the PXR geometry produces either a double lobe or a donut shape (Fig. 8(a)) with a hole in the center. Other geometries break the symmetry and produce a PXR beam with peak intensity at the resonant point [161].

The PXR spatial dispersion is analogous to the transfer function of a crystal monochromator with the same parameters (i.e., the same material, Bragg plane, and angle). This property is advantageous for the PXR source since it allows excellent noise filtration schemes, analogous to the double monochromator scheme used in synchrotron facilities [185]. Further analysis and applications of this property are discussed in Section 5.3.

Under practical conditions, the observed width of the intrinsic PXR spectral linewidth,  $\delta\omega/\omega$ , at a specific observation angle  $\Omega$  is determined primarily by the experimental geometrical angular resolution  $\Delta\Omega_{\rm geo}$ . This angular resolution is influenced by factors such as the beam spot size on the crystalline target, size of the x-ray detector, and distance between them. The relationship between the PXR spectral linewidth and the angular resolution is given by  $\Delta\omega/\omega = \Delta\Omega_{\rm geo}/\tan\theta_{\rm d}$ , as shown experimentally in [170,244]. Section 5.2 provides a detailed discussion of the effective PXR linewidth, considering the experimental parameters such as the electron beam spot size, detector size, and the distance between the PXR crystal and the detector.

At an ideal angular resolution ( $\Delta\Omega_{\rm geo}=0$ ), the intrinsic PXR spectral linewidth  $\delta\omega/\omega$  is determined by the number of crystallographic planes N contributing to the PXR emission. This number is defined by the absorption length in the crystal (according to the kinematical PXR theory) or by the extinction length (according to the dynamical PXR theory). In cases where these lengths are longer than the electron mean-free path, N is instead determined by the mean-free path. The natural PXR linewidth is related to the number of crystallographic planes by  $\delta\omega/\omega \propto N^{-1}$ , which can be derived from both classical approaches and from the Heisenberg uncertainty principle [191]. An extremely narrow intrinsic PXR linewidth of  $\delta\omega/\omega \sim 10^{-8}$  is achievable when relativistic particles moving in a channeling regime within a bent crystal emit a focused PXR beam [191]. However, for a non-ideal angular resolution,  $\Delta\Omega_{\rm geo}\neq0$ , the intrinsic PXR linewidth,  $\delta\omega/\omega$ , becomes significantly broader, primarily influenced by the geometry of the PXR system, as discussed further in Section 5.2.

#### 3.5.3. Polarization of PXR

Figure 8(a) shows the angular shape and polarization of PXR for different polar emission angles. The PXR polarization is linear at every point of the PXR reflection. The polarization structures differ between the PXR emissions in the forward hemisphere, backward hemisphere, and perpendicular direction to the incident particle beam. The polarization structure has a hyperbolic shape in the forward hemisphere and a parabolic shape in the backward hemisphere. In the exact backward direction, the parabolic shape becomes a radial polarization structure similar to that of Cherenkov radiation or transition radiation. The polarization structure in the PXR reflection emitted at a perpendicular angle to the particle beam has a specific shape [176], but most of the radiation is polarized in only one direction. The kinematical PXR theory of polarization is in good agreement with the experimental results [175,176,178].

#### 3.5.4. Main contributions to the radiation yield of PXR

The PXR yield is provided in Eq. (4) and depends on the diffraction efficiency and the geometrical factor  $f_{\rm geo}$ . The diffraction efficiency describes the PXR photons production per unit length. The geometrical factor,  $f_{\rm geo}$ , captures the self-absorption of the PXR photons within the crystal during the emission process. Heavy materials have higher diffraction efficiency but are limited due to their lower absorption length, which results in a smaller geometrical factor. Table 2 shows this tradeoff for the different materials discussed in this review. For example, highly oriented pyrolytic graphite (HOPG) has a low atomic number and thus low diffraction efficiency, but it also has a higher absorption length and, thus, a higher geometrical factor.

The diffraction efficiency is calculated by the Fourier expansion of the electric susceptibility  $\chi_g$  [86]:

$$\chi_g^2 = \frac{\lambda_x^4 r_e^2}{\pi^2 V_c^2} S_{hkl}^2 \left[ (F_0 (\mathbf{g}) + f_1 - Z)^2 + f_2^2 \right], \tag{7}$$

	Atomic Number (Z)	Lattice Type	Unit Cell Dimensions (Å)	Absorption Length at 30 keV L <sub>abs</sub> (mm)	Radiation Length X <sub>0</sub> (mm)
Graphite	6	Hexagonal	$d_0 = 2.461$ c = 6.708	80.7	164
Aluminum	13	FCC	4.04	4.33	89.9
Silicon	14	FCC	5.43	3.77	94.8
Copper	29	FCC	3.61	0.11	14.7
Molybdenum	42	BCC	3.14	0.036	9.8
Tungsten	74	BCC	3.165	0.024	3.5

Table 2. Materials Parameters for PXR Yield Calculations in Fig. 8

where  $\lambda_x$  is the emitted PXR wavelength,  $r_{\rm e}$  is the classical electron radius,  $V_c$  is the volume of the crystal unit cell,  $S_{\rm hkl}$  is the structure factor, Z is the atomic number,  ${\bf g}$  is the reciprocal lattice wavevector, and  $F_0({\bf g})$ ,  $f_1$ ,  $f_2$  are the atomic form factors.

The term  $F_0(\mathbf{g})$  is the momentum transfer efficiency of the beam and can be described semi-analytically using the following expression [245]:

$$F_0(s) = \sum_{i=1}^4 a_i \exp(-b_i s^2) + c,$$
 (8)

where  $s = \frac{\sin \theta_B}{\lambda_x} = \frac{1}{2d_{\rm hkl}}$ , and  $a_i, b_i, c > 0$  are the Cromer–Mann coefficients [245,246]. Since  $F_0(s)$  depends on  $\exp(-b_i s^2) \propto \exp\left(-b_i \left(\frac{\sin \theta_B}{\lambda_x}\right)^2\right)$ , the PXR yield decreases for higher PXR energies and larger PXR emission angles  $\Omega$ . Equivalently, the momentum transfer efficiency reduces for a lower interplane distance  $d_{\rm hkl}$ . This term limits the production of PXR at high x-ray energies. To cope with this challenge, it is necessary to reduce the Bragg angle. The atomic form factors  $f_1$  and  $f_2$  are the dispersion corrections that describe the behavior due to the bound inner-shell electrons; thus, they are independent of the wavevector  $\mathbf{g}$  but depend only on the x-ray energy.

The geometrical factor is proportional to  $f_{\rm geo} \propto L_{\rm abs} \propto 1/Z^4$  (Section 4.2), whereas the diffraction efficiency is proportional to  $\chi_g^2 \propto Z^2$ , leading to a PXR yield dependence of  $N_{\rm PXR} \propto f_{\rm geo} \chi_g^2 \propto 1/Z^2$ . Therefore, lighter materials are preferable for producing more PXR photons. Figure 8(c) presents the PXR yield for various materials. Graphite (HOPG) is the lightest material examined (Z = 6) and thus exhibits the highest yield. The typical values of PXR yield are  $\sim 10^{-5} - 10^{-6}$  photons/electron and are calculated for optimal material thicknesses considering the absorption length. The jumps in the PXR yield (e.g., at 8 keV in Cu and at 70 keV in W) are due to the dispersion correction of the bound inner-shell electron cross-section (the  $f_1$  and  $f_2$  terms).

# 4. RECENT DEVELOPMENTS TOWARD PRACTICAL APPLICATIONS

In this section, we present recent experimental and theoretical developments in PXR sources for increasing the flux to suit *in-vivo* biomedical applications. Two parameters determine the PXR source flux—the yield (i.e., the average number of photons produced per single electron) and the electron source current (i.e., the number of electrons that pass through the target crystal per time unit). Even though the PXR yield is high relative to other electron-driven sources [134], the self-absorption of the emitted x-ray photons within the thick PXR crystal limits its yield [247]. Moreover, the thermal load on the PXR crystal restricts the maximal incident electron beam current [248].

We address these limitations in the following steps. In Section 4.1, we present the progress in high-quality electron beam sources and their impact on the thermal load in the PXR target crystal. We discuss how state-of-the-art and next-generation electron sources can fit the thermal load requirement. In Section 4.2, we review different PXR geometries that overcome the PXR photons' self-absorption limitation, enabling higher interaction lengths and higher spectral yield.

While the challenges and mitigation in this section are related to the PXR emission, the insights and advancements discussed can be extended to other sources such as Smith–Purcell radiation, Cherenkov radiation, channeling radiation, and coherent bremsstrahlung [249].

# 4.1. Progress in PXR Relying on High-Quality Electron Beam Sources

In recent years, progress in electron sources and acceleration structures has paved the way for high brightness, high-current electron sources, with practical applications for XFELs, ultrafast electron microscope (UEM), and ultrafast electron diffraction (UED) applications [151]. This progress leads to high electron source currents in compact acceleration structures. By using these novel high-current electron sources, the primary limiting factor transitions to the thermal load on the PXR crystal. Intuitively, the PXR source brightness increases with the number of electrons passing through the PXR crystal with the smallest possible spot size. However, the electron flux deposits energy in the crystal, leading to significant crystal heating and thermal vibrations that decrease the PXR yield. These considerations create a trade-off with a specific optimum. A recent quantitative analysis of this trade-off identified the optimal parameters, highlighting the prospects of a practical PXR source.

# 4.1.1. Effect of Heat Load

Relativistic lectrons lose a small fraction of their kinetic energy when they pass through a target. The energy loss partially goes into radiation emission (i.e., bremsstrahlung) and partially into heat. The heat from a single electron pulse is deposited in a volume determined by the electron beam spot size and the thickness of the PXR crystal. The thermal load causes crystal lattice vibrations, leading to a phase mismatch between the atoms, and a loss of constructive interference between the dipoles.

The PXR yield dependence on the crystal temperature is described by the Debye–Waller factor  $e^{-2W}$  (Eq. (4)) [86]. Two distinct phenomena cause crystal lattice vibrations. The first is purely quantum mechanical and arises from the uncertainty principle. These vibrations are independent of the temperature and occur even at absolute zero temperature, known as zero-point fluctuations. At finite temperatures, elastic waves (or phonons) are thermally excited in the crystal, increasing the amplitude of the vibrations. Those thermal vibrations cause PXR phase loss between the lattice dipoles, decreasing the PXR yield. This effect depends on the material-specific Debye temperature,  $T_D$ , the material temperature,  $T_D$ , and the  $T_D$  and the  $T_D$  is effect diffraction plane of interest,  $T_D$ , the material temperature,  $T_D$ , and the  $T_D$  is effect depends on the diffraction plane of interest,  $T_D$ , the material temperature,  $T_D$ , and the  $T_D$  is effect depends on the material plane of interest,  $T_D$ , the material temperature,  $T_D$ , and the  $T_D$  is effect depends on the diffraction plane of interest,  $T_D$ , the material temperature,  $T_D$ , and the  $T_D$  is effect depends on the material plane of interest,  $T_D$ , the material temperature,  $T_D$ , and the  $T_D$  is effect depends on the material plane of interest,  $T_D$ , the material temperature,  $T_D$ , and the  $T_D$  is effect depends on the material plane of interest.

The crystal thermal vibration mean square amplitude is given by [248]

$$u^{2}(T) = \frac{3\hbar^{2}}{4Mk_{B}T_{D}} \left[ 1 + 4\left(\frac{T}{T_{D}}\right)^{2} \int_{0}^{T_{D}/T} \frac{y}{e^{y} - 1} dy \right],$$
 (9)

where M is the material mass, and  $k_B$  is the Boltzmann constant. The Debye–Waller term  $(e^{-2W})$  is derived from the thermal vibration mean square amplitude  $(u^2(T))$  and the reciprocal lattice vector  $(\tau = 2\pi/d_{\rm hkl})$ , and equals  $e^{-2W} = \exp\left(-\tau^2 u^2(T)\right)$ . This

relation with Eq. (9) leads to an exponential decrease in the PXR yield as the temperature increases. Due to this effect, there is an optimal electron current maximizing the PXR yield.

Previous PXR experiments were limited to average electron source current below 5  $\mu$ A (Table 1). As stated in these experiments, using a greater electron charge per pulse caused damage to the PXR crystal [136]. However, by carefully optimizing the electron source parameters, it is possible to increase the repetition rate of the electron source without damaging the PXR crystal. In essence, by refining the heat dissipation process, the optimal average electron source current varies depending on the PXR crystal material, falling within the range of 500–3000  $\mu$ A. This represents an increase of up to 2–3 orders of magnitude compared with the currents involved in prior x-ray imaging experiments (Table 1).

# 4.1.2. Requirements from the Electron Beam Source

Beam instabilities may emerge when increasing the electron source peak current. This phenomenon is known as the beam blow-up (BBU) or the beam break instability [250]. It arises from the interaction between the electron beam and the cavity modes of the accelerating cells [251]. In this case, the electron beam is subject to density and velocity perturbation, increasing the beam emittance and energy spread. The higher the peak current, the more unstable the beam [252]; thus, to mitigate the electron BBU instabilities, a higher repetition rate with a lower peak current in each pulse is preferable. Indeed, next-generation XFEL electron sources are designed to operate at a high repetition rate of 1 MHz [151].

It is important to highlight that a higher repetition-rate electron source is advantageous for the PXR scheme brightness due to the inverse relation between the optimal repetition rate and the electron beam spot size, leading to a smaller x-ray source spot size. For example, the optimal beam spot size for an electron source with a repetition rate of 1 MHz and a pulse charge of 1 nC is  $\sigma_x \approx 40 \, \mu m$ . Notably, state-of-the-art and next-generation electron sources fulfill the optimal requirements [150,253,254].

Additionally, it is worth noting that even if the electron beam quality has moderate degeneration, it would still meet the PXR source requirements. In contrast to the strict requirements of the x-ray FEL electron source, which must be satisfied for electron micro-bunching [3], the requirements for the PXR scheme are more relaxed, as discussed in Section 3.5.

To further enhance the electron source peak current, an approach similar to that of the x-ray rotating anode tube can be used. x-ray tube machines experience similar heating challenges to those experienced by PXR crystals. The solution used in these machines is based on a rotating anode [86,255,256]. This method increases the effective heat dissipation area since the electron beam interacts with different positions of the target material. A similar approach can be used for the PXR heat dissipation solution. The main difference between the machines is that the target material for the PXR source should be modified by translation and not by rotation, since a rotational change of the PXR crystal alters the x-ray emission direction. An additional crucial difference between the x-ray tube and the PXR source is that precision alignment is unnecessary with the x-ray tube, but is critical for the PXR crystal. The alignment process can be similar to the double crystal monochromator scheme used in synchrotron facilities [257], where large crystals are available. These wafers can be translated much like a rotating anode so that the electron beam is concentrated near the outer edge of the wafer. This scheme can further increase the PXR flux, yet further studies should explore the possible artifacts of a moving crystal target (such as blurring), as it has never been used before for PXR production.

# 4.2. Progress in PXR Relying on Material and Geometry Design

The emergence of new heterostructures and materials geometries, such as van-der-Waals materials, has led to the development of precise and versatile methods for fabricating devices with atomic-scale accuracy. Hence, these materials have shown much promise for different technologies, including photodetectors, photocatalysis, photovoltaic devices, ultrafast photonic devices, and field-effect transistors [60]. By leveraging these advancements, the PXR crystal yield can be optimized to address challenges such as the self-absorption of PXR photons within the crystal. This section reviews recent breakthroughs and demonstrates the promising outcomes of utilizing such geometries.

# 4.2.1. The Challenge of X-Ray Self-Absorption

For a thick PXR crystal, the emitted PXR photons are self-absorbed within the crystal, limiting the contribution of all the crystal layers to the PXR intensity (Fig. 9(a)). This phenomenon is captured by the geometrical factor, which sets an upper bound on the PXR yield. This limitation is especially significant for high-Z materials with shorter absorption lengths.

Any x-ray beam is attenuated during its interaction with a thick target material. The attenuation is caused by several physical mechanisms but is mainly due to photoelectric absorption, Compton scattering, and elastic scattering [258]. The same phenomenon occurs for the emitted PXR photons within the crystal. Close to the crystal surface, the number of PXR photons produced is linearly proportional to the material thickness. However, PXR photons emitted in deeper regions must traverse through the entire crystal, contributing significantly less than PXR photons produced at the surface of the crystal. Hence, the material absorption length limits the PXR yield.

The x-ray attenuation is exponential with an attenuation coefficient  $\mu$ , resulting in the following geometrical factor term expression [233]:

$$f_{\text{geo}} = L_{\text{abs}} \left| \frac{\hat{n} \cdot \hat{\Omega}}{\hat{n} \cdot \hat{v}} \right| \left( 1 - e^{-L/\left(L_{\text{abs}} | \hat{n} \cdot \hat{\Omega} | \right)} \right), \tag{10}$$

where  $L_{\rm abs}=1/\mu$  is the absorption length of the material,  $\hat{n}$  is the normal to the crystal surface through which the electron beam traverses,  $\hat{\Omega}$  is the emission direction of the emitted PXR photon,  $\hat{v}$  is the direction of the electron beam, and L is the crystal thickness. The attenuation coefficient is proportional to  $\mu \propto \frac{Z^4}{\omega^3}$ , depending on the x-ray energy, the material atomic number Z, and the material mass density; thus, heavier materials have much larger attenuation.

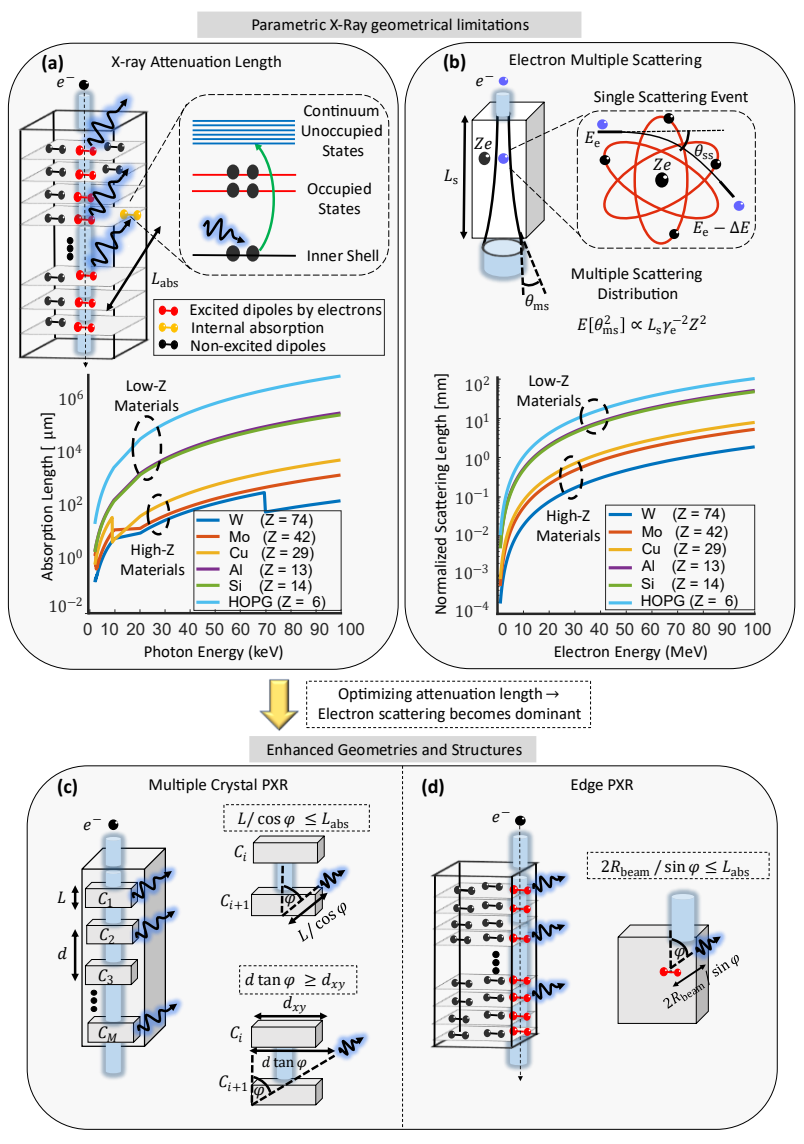
#### 4.2.2. Challenge of Electron Beam Scattering

When an electron passes through the PXR crystal, it gradually deviates from its initial trajectory due to the electrostatic forces applied by the material atoms. The electron scattering affects the PXR angular broadening, similar to the effect of the electron beam divergence. This scattering process has a random walk profile, for which the likelihood and the degree of the electron scattering is a probability function of the crystal thickness and the radiation length (i.e., the mean free path) [259].

In particular, the scattering angle is modeled with Gaussian probability with zero mean scattering and standard deviation. The following formula was empirically determined to accurately capture the standard deviation of the scattering angle as a function of the electron energy  $E_{\rm e}$ , material type, and thickness L [260]:

$$\sigma_{\theta_{ms}} = \frac{13.6 \,\text{MeV}}{E_{\text{e}}} \sqrt{\frac{L}{X_0}} \left( 1 + 0.038 \ln \left( \frac{L}{X_0} \right) \right), \tag{11}$$

Figure 9



PXR schemes for enhancing the PXR yield. (a) x-ray attenuation length. The excited radiating dipoles produce PXR photons through all the crystal layers, yet the photons traversing the whole crystal attenuate. The absorption length is shown for different materials as a function of the PXR energy. High-Z materials have shorter absorption lengths; thus, a smaller volume of the PXR crystal contributes to the emission. The absorption length is longer for higher PXR energies. (b) Electron beam multiple scattering. The electrons slightly deviate from their initial trajectory due to the electrostatic forces applied by the material atoms. The scattering length increases with higher electron energies. For heavier crystals, the scattering length is shorter. (c) Multiple crystals PXR scheme. The crystals are stacked upon each other with two fabrication conditions: 1) Each crystal should be thinner than the absorption length. 2) The distance between the crystals should be larger than the escape path of the emitted photon. (d) Edge PXR. The electron beam passes within the crystal parallel to the crystal edge. To overcome the self-absorption of the emitted PXR photons, the beam spot size should be smaller than the attenuation length of the material. Another method for minimizing multiple scattering involves generating focused PXR through the channeling of positively charged particles, such as positrons, in a long, bent, thin crystal [191]. This approach is attractive as positrons have a significantly longer channeling length compared to electrons [221]. Reprinted from [146].

75

where  $X_0$  is the radiation length, which depends on the material type. Figure 9(b) shows the electron scattering lengths for the different materials and electron energies. Higher electron energies and lighter materials have lower scattering angles since  $\sigma_{\theta_{ms}} \propto X_0^{-1/2} \gamma_{\rm e}^{-1}$ . The electrons' multiple scattering broadens the PXR angular shape, resulting in a higher PXR spectral linewidth (Eq. (6)).

Several methods have been developed to evaluate the angular broadening of PXR, including standard Monte Carlo numerical simulations [169,261,262]. Here, we present the Potylitsyn method, which has shown good agreement with experimental results [173]. This method involves convolving the Gaussian distribution of the electron scattering with the PXR angular shape  $N\left(\theta_x,\theta_y\right)$  (as defined in Eq. (5)):

$$\tilde{N}\left(\theta_{x},\theta_{y}\right) = \frac{1}{2\pi\sigma_{\theta_{\text{ms}}}^{2}} \int_{-\infty}^{\infty} d\phi_{x} d\phi_{y} N\left(\theta_{x} - \phi_{x}, \theta_{y} - \phi_{y}\right) \exp\left\{-\frac{\left(\phi_{x}^{2} + \phi_{y}^{2}\right)}{2\sigma_{\theta_{\text{ms}}}^{2}}\right\}, \quad (12)$$

where  $\sigma_{\theta_{ms}}$  is defined in Eq. (11). The electron multiple scattering leads to a spatial shape and dispersion broadening, which decreases the PXR source brightness, as discussed next.

# 4.2.3. Overcoming the Challenges by Optimizing the Crystal Geometry

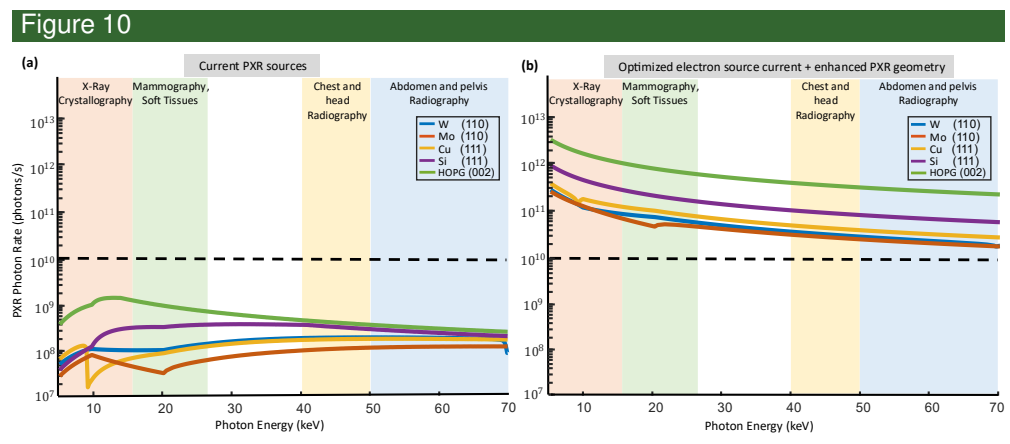
We review two PXR schemes to cope with the limitations of the self-absorption of PXR photons within the crystal. In these geometrical schemes, instead of self-absorption, electron beam scattering is the limiting factor (Fig. 9(b)). The electron beam scattering leads to the PXR angular emission broadening and limits the number of emitted photons that hit the detector within the angular aperture. Assuming that the self-absorption phenomenon is negligible, the optimal PXR crystal thickness is  $L\approx 0.1X_0$ . Above this crystal thickness, the PXR flux gain becomes small, and the source brightness decreases. This optimal material thickness is up to an order of magnitude larger than the absorption length for heavy materials. Since the x-ray attenuation coefficient is higher for lower x-ray energies, these schemes have a considerable gain for lower x-ray energies.

The first scheme is a stacked multiple crystals structure (Fig. 9(c)), and the second is an edge PXR structure (Fig. 9(d)). In the first scheme, two conditions should be fulfilled: (1) The thickness of each crystal should be thinner than the absorption length. (2) The distance between the crystals should be sufficiently large so that the emitted photons do not pass through the adjacent crystal.

The "edge PXR" structure, which is also called "grazing PXR" or extremely asymmetric diffraction PXR [153–155], is based upon transmission of the electron beam within the crystal, parallel to the crystal edge surface. In this structure, the electron spot size should be shorter than the absorption length so that the emitted PXR photon would traverse a shorter distance than the absorption length. This structure has been examined experimentally for silicon crystals, where a PXR yield gain of a factor of 5 was reported, which fits well with the theoretically expected gain [152].

# 4.2.4. Resulting Optimal X-Ray Flux

Figure 10 compares the PXR photon rate between the standard PXR scheme and enhanced PXR schemes for different PXR materials. The x-ray spectrum is divided into the following target applications: x-ray crystallography (<15 keV), mammography (10–25 keV), chest and head radiography (40–50 keV), and abdomen and pelvis radiography (50–70 keV). The dashed line represents the photon rate necessary for *in-vivo* imaging. The target angular aperture used for the flux derivation is  $\theta_{\rm D} \sim 3\gamma_{\rm e}^{-1}$ . The gain is considerable for lower x-ray energies due to the higher self-attenuation in



Optimized PXR photon rate for optimized PXR geometries and electron source currents. Photon rate comparison between a classic PXR scheme (a) and enhanced PXR schemes (b) for different materials, assuming an optimal electron source current and optimized geometries. The assumptions are: 1) the maximal interaction length is 10 mm (in both schemes). 2) The incident electron energy is 60 MeV. 3) The detector's angular aperture is  $\theta_D = 3\gamma_e^{-1}$ . 4) The material thickness in the regular PXR scheme is the material absorption length, while in the enhanced PXR geometry is  $0.1X_0$ , where  $X_0$  is the material radiation length. The spectrum is split into regions for different applications. The dashed line marks the photon rate needed for practical applications. The enhanced PXR geometries have a more significant gain for lower PXR energies since the absorption length is shorter in these regions. Reprinted from [146].

this region. At higher x-ray energies, the flux decreases due to lower diffraction efficiency. Overall, the PXR flux for the different PXR crystals is adequate for practical applications.

Such PXR schemes are limited by several factors. In the multiple PXR crystals scheme, the final image may have a blurring artifact due to the many beams' emissions from each sub-crystal. Image processing techniques can reduce this artifact [66]. Moreover, the multiple crystals' alignment relative to the electron beam should be the same, which may be experimentally challenging. In the edge PXR scheme, the necessity for a precise alignment between the electron beam and the PXR crystal edge can face a challenge, yet earlier experiments demonstrated this [152]. Despite the PXR source flux growth, the PXR source signal-to-noise ratio remains the same between the standard and the enhanced schemes since both PXR and bremsstrahlung increase linearly with the material thickness.

It is important to highlight that recent experimental setups have employed a wedge-shaped crystal plate as the PXR radiator [136,223]. In the case of a rectangular edge shape, PXR beams emitted from the front and side surfaces have different refraction properties. The superposition of these beams strongly disturbs phase-contrast imaging. Therefore, apart from enhancing the flux, the primary motivation for using wedge-shaped crystal plates lies in suppressing multi-beam effects.

# 5. ROADMAP TOWARD A COMPACT X-RAY SOURCE

This section presents the applied aspects involved in developing compact sources of hard x-rays, with the ultimate goal of enabling applications such as phase-contrast imaging. Key experimental considerations include the electron beam quality, radiation safety, x-ray source geometry and dimensions, calibration process, and diagnostic systems. We specifically illustrate these considerations through the design of a com-

pact PXR source, based on recent advances in the field. However, while the discussion centers on PXR, the same principles apply to other compact x-ray sources, such as ICS [31].

Section 5.1 presents the proposed design for a compact x-ray source. Section 5.2 analyzes the system performance and the emitted x-ray characteristics, and Section 5.3 addresses techniques for filtering noise from the x-ray source.

# 5.1. Design of the Hard X-Ray Source

Figure 11 describes the compact source of hard x-rays based on the PXR mechanism. The electron source, which is based on a thermionic RF-gun and a linear acceleration structure, produces the relativistic electron beam. Two Q-magnets focus the electron beam, one at the PXR crystal and the other before the electron beam dump. A double crystal scheme, based on a combination of a PXR crystal and a monochromator, produces a filtered PXR beam with a fixed exit location, as discussed later in this section.

The PXR beam exits through a collimator and an exit window. A power supply, RF modulator, a Klystron, and a control system feed the PXR system. The estimated dimensions of the PXR source are  $3 \times 3$  m<sup>2</sup>, similar to those of other tunable and compact x-ray machines, such as the inverse Compton scattering x-ray source [31]. In this design, the PXR crystal geometry can be based on either a regular or an advanced structure (Section 4.2). The PXR crystal has an assembled cooler and a heat sink to dissipate heat from its edges.

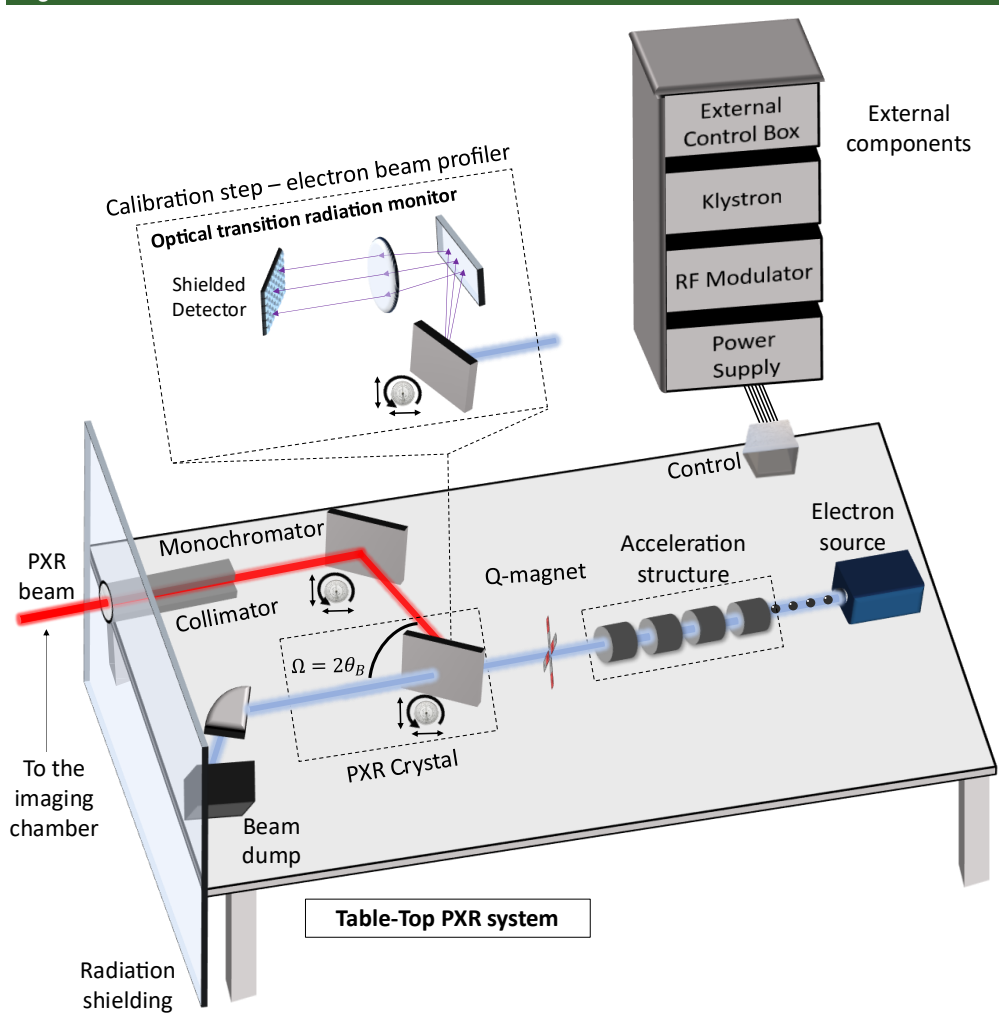
The setup shown in Fig. 11 produces not only PXR but also additional forms of electromagnetic radiation, primarily emitted in the forward direction. Bremsstrahlung radiation arises from electron acceleration in the different system components, including the electron gun, acceleration structures, collimators, exit window, and the crystal target. The crystal's periodic structure also gives rise to coherent bremsstrahlung, while a wide-band forward-directed transition radiation is produced at the surfaces of both the exit window and the crystal target.

Other types of radiation are emitted from the crystal target at large angles relative to the beam axis. Among these are optical transition radiation, emitted at the mirror angle from the entrance surface of the target, and two distinct types of x-ray radiation besides PXR. The first type is the isotropic characteristic x-ray radiation from the crystal atoms, characterized by fixed spectral peak energies. An additional type of radiation is produced during this process by the reflection of diffracted transition x-ray radiation at the Bragg frequency, which is coaxial to PXR reflection in the Bragg geometry [106].

A facility with an electron beam energy of up to approximately 100 MeV and a current of approximately 1 mA would support research and development applications for all these types of radiation, including PXR. These values are of particular relevance since they bring PXR to a regime where it dominates the overall emission and is desirable for x-ray phase-imaging applications. Such a facility should be equipped with goniometer stages with angular precision of less than  $0.1\gamma_e^{-1}$ , x-ray detectors and spectrometers, as well as flexible tuning knobs to control electron beam parameters such as its angular spread and brightness.

The optical transition radiation (OTR) subsystem monitors the electron beam crossing with the PXR crystal. Generally, several mechanisms can accomplish this: OTR screen, YAG, wire scanner screen, and Cherenkov radiation [263]. Here, we analyze the use of OTR, as it is broadly used in beam diagnostics in linear accelerators. Its linear intensity

Figure 11



Design for a compact system of parametric x-ray radiation (PXR). The compact PXR system contains the following components: an electron source and a linear acceleration structure; a set of apertures and magnetic lenses that focus a collimated electron beam on the PXR crystal; the PXR crystal that produces the x-ray beam; a monochromator that filters the noise floor; additional quadruple magnet lens after the PXR crystal that focuses the electron beam to a beam dump, with a deceleration structure to reduce neutron production; an optical transition radiation (OTR) subsystem that monitors the electron beam position and width on the PXR crystal (observed in the backward geometry to avoid detection along the electron path and avoid the forward bremsstrahlung radiation). During the calibration stage, a control system optimizes the x-ray radiation by analyzing the optical signal and adjusting the electron beam position and the crystal displacement to position the beam correctly on the target. Additional power and RF modulation mechanisms are located outside the shielded PXR environment. A goniometer rotation mechanism (accuracy of  $\sim 0.01^{\circ}$  [185]) and x-y displacement stages are used for the calibration process of both crystals. To optimize the x-ray beam quality, the monochromator crystal requires precise alignment relative to the PXR radiator, compensating for the slight difference between PXR frequency and Bragg frequency reflected by the monochromator (Eq. (3)) [142,232]. The estimated system size is roughly  $3 \times 3 \text{ m}^2$  [194]. Adapted from [146].

growth as a function of the beam current is a great advantage compared to fluorescent screens, which are subjected [264]. In addition, previous PXR experiments have used OTR for this purpose [160,210,224].

When considering high electron energy facilities, radiation safety is a central challenge to cope with due to the production of neutrons during the electron beam dump. The typical electron source energy required for a PXR source exceeds the neutron production threshold; thus, the PXR source must have a large and thick radiation shield to protect the operators and users. Several options can be employed to reduce the shielding requirements. One approach, proposed originally for ICS sources, involves decelerating the electron beam before the dump, enabling the system to be compact enough to fit within a sea container. This option is presented in Fig. 11 and has been proposed previously for a PXR source [145]. Another option is to use an electron beam energy below the neutron production threshold. Since the PXR emission energy does not depend on the incident electron energy, the PXR source scheme remains essentially the same. In this case, the PXR beam divergence would increase, yet it can be favorable for imaging applications due to the larger field of view. However, using electron source energies below 10 MeV for PXR imaging applications should be further researched.

#### 5.2. System Performance and X-Ray Source Characteristics

In Section 3.5.2, we have seen that in an ideal PXR system, the intrinsic spectral linewidth is inversely proportional to the number of crystallographic planes,  $\delta\omega/\omega \propto N^{-1}$ . In the following section, we analyze the factors contributing to the broadening of this intrinsic PXR linewidth,  $\delta\omega/\omega$ , and conclude by determining the realistic linewidth achievable considering all these factors.

The intrinsic PXR spectral linewidth  $\delta\omega/\omega$  is affected by several characteristics related to the source and setup, including the electron beam source quality, the PXR crystal material, and the experimental geometry [244]. These effects can be classified into three main categories: (1) Geometrical parameters, including the distance from the crystal to the detector  $R_{\rm d}$  and the detector collimation width  $D_d$ . (2) The crystal thickness and quality, especially its mosaicity, which represents the imperfection in the lattice translation throughout the crystal. (3) The electron beam quality, including its spot diameter  $D_{\rm e}$  and divergence  $\Delta\theta_{\rm e}$ .

The electron source quality parameters, such as the energy spread and emittance, affect the performance of all high-brightness x-ray mechanisms [151]. However, in contrast to other mechanisms, PXR in the ultra-relativistic regime is practically independent of the incident electron energy. Thus, the electron energy spread has a negligible impact on the intrinsic PXR linewidth  $\delta\omega/\omega$ . The linewidth still depends on the electron emittance, in addition to its strong dependence on the system geometry and the crystal Bragg plane and Bragg angle (Eq. (3)). The two subsections below elaborate on these considerations.

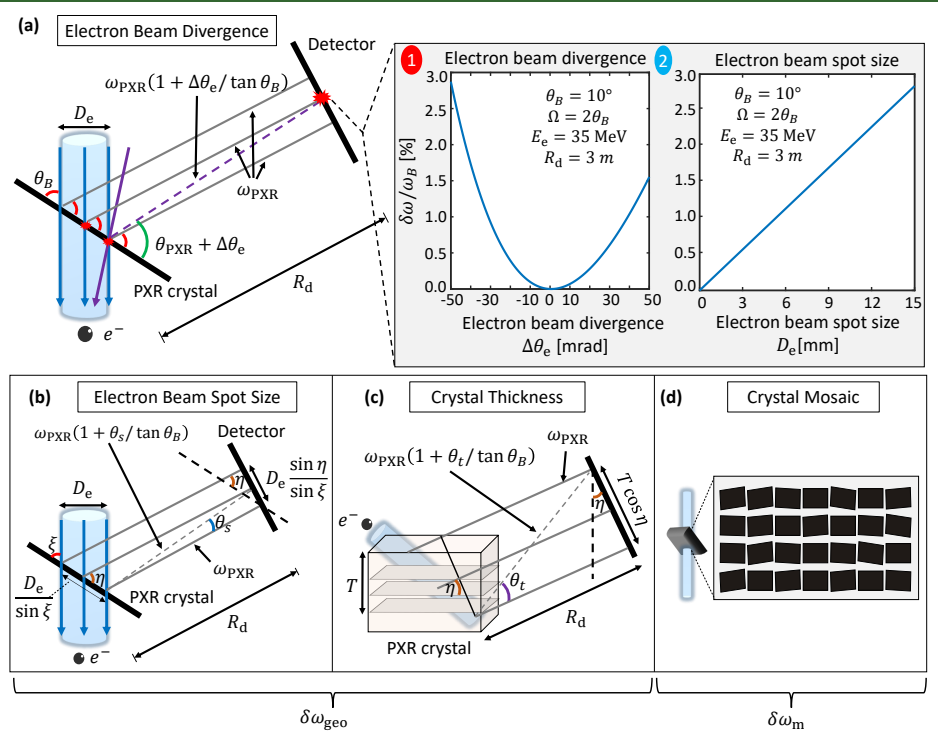
# 5.2.1. Effects of Geometry and Electron Beam Quality on the X-Ray Linewidth

When an incident electron impacts the crystal with a deviation angle  $\Delta\theta_e$ , both the Bragg angle  $(\theta_B)$  and the observation angle  $(\Omega)$  are shifted by the same amount,  $\Delta\theta_e$ . These parameters alter the PXR frequency, as can be captured by approximating Eq. (3):

$$\hbar\omega_{\rm PXR} = \frac{2\pi\hbar c}{d_{hkl}} \frac{\sin(\theta_B + \Delta\theta_{\rm e})}{1 - \beta\sqrt{\epsilon}\cos\left(\Omega + \Delta\theta_{\rm e}\right)} \approx \frac{2\pi\hbar c}{d_{hkl}} \frac{\sin\left(\theta_B + \Delta\theta_{\rm e}\right)}{2\sin^2\left[\left(\Omega + \Delta\theta_{\rm e}\right)/2\right]},$$
 (13)

which is valid for  $\Delta\theta_e \ll 1$ ,  $\Delta\theta_e \ll \theta_B$ , and  $\Omega \approx 2\theta_B$ . This approximation helps to extract the intrinsic PXR spectral linewidth  $(\delta\omega/\omega)$  broadening and its dependence on





Influence of experimental factors on the spectral x-ray linewidth  $\delta\omega/\omega$ . The dependence of the PXR linewidth,  $\delta\omega/\omega$ , on the electron beam divergence (a) and spot size (b), crystal thickness (c), and crystal mosaicity (d). A collimated electron beam impacts the PXR crystal with an angle  $\xi$  relative to its surface (panel (a) assumes that the crystal surface and the Bragg plane coincide). The PXR material's dipoles radiate into an angle  $\eta$  relative to the PXR crystal surface. The radiation arises from a confined volume in the PXR crystal, defined by the crystal thickness, electron beam trajectory, and its spot size. The impact of electron beam divergence and spot size on the PXR energy spread is shown in panels (a1) and (a2), respectively. The parameters used for producing the graphs are the electron beam energy of  $E_{\rm e}=35\,{\rm MeV}$ , the distance between the PXR crystal and the detector is  $R_{\rm d}=3\,{\rm m}$ , the Bragg angle is  $\theta_{\rm B}=10^{\circ}$ , and the observation angle is  $\Omega=2\theta_{\rm B}$ . The uncertainty in the location of the radiating dipole results in geometrical linewidth broadening, as the emission energy is related to the emission observation angle (Eq. (3)).

two primary factors: the first is related to electron beam divergence and its multiple scattering captured by uncertainties in  $\Delta\theta_e$ , and the second arises from geometrical uncertainties in the observation angle  $\Omega$ . Figure 12 illustrates the impact of these factors on the intrinsic PXR spectral linewidth  $(\delta\omega/\omega)$  broadening.

For the first factor, the uncertainty in  $\Delta\theta_e$  (Fig. 12(a)), the first-order derivative of the PXR energy with respect to  $\Delta\theta_e$  is zero in the central observation angle (the Bragg angle  $\Omega = 2\theta_B$ ):

$$\left. \frac{\partial \left( \hbar \omega_{\text{PXR}} \right)}{\partial \left( \Delta \theta_{\text{e}} \right)} \right|_{\Delta \theta_{\text{e}} = 0, \Omega = 2\theta_{B}} = 0. \tag{14}$$

Therefore, Eq. (14) implies that the first-order effect of the electron beam divergence vanishes, and only second-order effects contribute, i.e., the effect of multiple scattering on the intrinsic PXR linewidth broadening is relatively small. Consequently,

762

the second-order approximation to the intrinsic spectral linewidth broadening is  $\delta \omega_{\rm div}/\omega \approx \frac{1}{4} \frac{(\Delta \theta_{\rm e})^2}{\sin^2 \theta_B}$ , which is typically smaller than the other contributions for the intrinsic spectral linewidth broadening, as discussed further below.

The uncertainty in the observation angle  $\Omega$  originates from the geometrical factors of the electron beam spot size (Figs. 12(a2) and 12(b)), the thickness and absorption length of the crystal (Fig. 12(c)), and the numerical aperture captured by each individual pixel in the detector (also called detector collimation), as follows:

$$\Delta\Omega_{\rm beamSpotSize} = \frac{D_{\rm e}}{R_{\rm d}} \frac{\sin\eta}{\sin\xi},$$

$$\Delta\Omega_{\rm crystalThickness} = \frac{\min(T, L_{\rm abs}(\omega)\sin\eta)}{R_{\rm d}} \cos\eta,$$

$$\Delta\Omega_{\rm detectorCollimation} = \frac{D_{\rm d}}{R_{\rm d}},$$
(15)

where  $0 \le \xi \le \pi/2$  is the angle between the target surface and the velocity vector of the electron beam,  $0 \le \eta \le \pi/2$  is the angle between the target surface and the observation direction (see Fig. 12 for illustration), and  $L_{\rm abs}(\omega)$  represents the absorption length of the PXR photon with a frequency  $\omega$  (Eq. (10)). The term  $D_{\rm e} \frac{\sin \eta}{\sin \xi}$  describes the electron beam spot size on the target surface in the observation plane, while the term  $L_{\rm abs}(\omega) \sin \eta \cos \eta$  represents the effective thickness of the target visible to the detector in the observation plane. The term  $D_{\rm d}$  represents the dimension of a *single pixel* in the detector. Therefore, by combining all the terms in Eq. (15) leads to the following uncertainty in the observation angle:

$$\Delta\Omega_{\rm geo} = \sqrt{\Delta\Omega^2_{\rm beamSpotSize} + \Delta\Omega^2_{\rm crystalThickness} + \Delta\Omega^2_{\rm detectorCollimation}}.$$
 (16)

The linewidth broadening due to the geometrical angular uncertainty is [262]:

$$\frac{\delta \omega_{\text{geo}}}{\omega} = \frac{\Delta \Omega_{\text{geo}}}{\tan \left(\theta_B\right)},\tag{17}$$

where Eq. (17) applies both to Laue and Bragg geometries. In the limit of  $\Delta\Omega_{\rm geo} \rightarrow 0$ , we obtain  $\delta\omega/\omega \propto N^{-1}$ , where N is the number of crystallographic planes (see Section 3.5).

The first two terms in Eq. (15)—the electron beam size ( $\Delta\Omega_{\rm beamSpotSize}$ ) and the crystal thickness ( $\Delta\Omega_{\rm crystalThickness}$ )—are typically lower than  $10^{-3}$  in most state-of-the-art PXR setups. In addition, in modern imaging applications that use high-resolution detectors, the ratio between the detector's dimension,  $D_{\Omega}$ , to the distance between the PXR crystal and the detector,  $R_d$  (i.e., the detector's collimation term in Eq. (15)), is typically significantly smaller than the other two terms. Hence, the detector's collimation has a minimal impact on the broadening of the intrinsic PXR spectral linewidth  $\delta\omega/\omega$ . Considering all the geometrical terms in Eq. (15), the typical intrinsic PXR linewidth is on the order of  $\delta\omega/\omega\sim 1\%$ . Moreover, it is important to note that the broadening of the intrinsic linewidth depends on cot  $\theta_B$  (Eq. (17)). Thus, as higher PXR energies require lower Bragg angles (Eq. (3)), it is preferable to use Bragg planes with higher Miller indices (i.e., smaller interplane distances) to maintain higher Bragg angles and minimize the intrinsic PXR spectral linewidth.

### 5.2.2. Effect of Crystal Mosaicity on the X-Ray Linewidth

The crystal mosaicity is an additional parameter that affects the intrinsic PXR spectral linewidth (Fig. 12(d)). Mosaicism is the degree of imperfection in the lattice translation throughout the crystal [86]. Macroscopic crystals are often imperfect and composed of small perfect blocks with a distribution of orientations around an average value.

Since each mosaic block emits a PXR beam with a slightly different orientation and angle, the PXR beam is spatially broadened, leading to a PXR spectral linewidth broadening. Typically, the mosaic blocks have orientations distributed over an angular range of  $0.01^{\circ}$ – $0.1^{\circ}$  [86]. Graphite (HOPG), which has a high PXR yield, suffers from high mosaicity with an angular range of  $0.4^{\circ}$  [184]. The total broadening of the intrinsic linewidth, accounting for the geometrical factor, electron beam divergence, and the crystal mosaicity, is given by [262]

$$\frac{\delta\omega}{\omega_B} = \frac{\sqrt{\left(\Delta\Omega_{\rm geo}\right)^2 + \left(\Delta\theta_{\rm m}\right)^2}}{\tan\theta_B} + \frac{1}{4} \frac{(\Delta\theta_{\rm e})^2}{\sin^2\theta_B},\tag{18}$$

where  $\Delta\theta_m$  account for the crystal mosaicity. Note that mechanical tensions on the crystals can increase  $\Delta\theta_m$  and can also be used to induce intentional variation in the lattice translation throughout the crystal to facilitate x-ray focusing [73,74].

# 5.3. Optimization of the X-Ray Source Signal-to-Noise Ratio

The radiation emitted from the source includes the desired PXR and competing mechanisms such as bremsstrahlung and transition radiation. Achieving high x-ray beam quality requires filtering these competing mechanisms, as they act as broadband noise that diminishes the brightness of PXR [265]. One strategy to mitigate the noise involves optimizing the PXR experimental parameters by enlarging the PXR emission angle, thereby reducing the intensity of the bremsstrahlung and transition radiation in the detector plane. While bremsstrahlung and transition radiation are emitted in the forward direction, parallel to the electron velocity direction, within a narrow cone of  $\gamma_e^{-1}$ , PXR can be emitted at a large emission angle of  $\Omega \gg \gamma_e^{-1}$ . By enlarging the PXR emission angle, the bremsstrahlung and transition radiation become less intense in the detector plane [146].

While larger PXR angles can help reduce the noise floor, additional noise suppression is essential, especially at higher x-ray energies. A common approach involves using a double-crystal system (illustrated in Fig. 11) that acts as a bandpass filter, with its passband energy range aligned with the PXR spatial dispersion [185,266,267]. In this double-crystal system, the PXR crystal and monochromator are arranged in a nondispersive configuration (Fig. 13(a)), similar to those used for filtration in synchrotron facilities [268,269]. Unlike these conventional monochromator designs, where the x-ray beam passes through two crystals that are held parallel, in the PXR scheme, the electron beam only interacts with one crystal to produce an x-ray beam (i.e., the PXR radiator). This x-ray beam then impinges on the second crystal, which is aligned to reflect only the PXR energy, acting as a crystal monochromator. This process ensures that the x-ray beam exits in the same direction as the incoming electron beam (as shown in Figs. 11 and 13(a)), allowing for consistent beam extraction without moving the entire PXR source or the target, thus making it highly advantageous for stable x-ray production [186]. In other words, this setup solves the challenge of maintaining a fixed output port for x-ray extraction, independent of the choice of PXR emission angle and the crystal angle [177].

Generally, the rocking curve of a monochromator is very narrow, as described by the DuMond diagram (Fig. 13(c)) [226]. The DuMond diagram describes the monochromator transfer function and acceptance region as a function of the incident x-ray energy ( $\omega_B$ ) and the angle relative to the Bragg plane ( $\theta_B$ ). An incoming x-ray beam that satisfies the Bragg condition will be reflected from the monochromator at the same angle as the incident beam angle. However, an incident beam that is slightly off the Bragg

PXR Crystal

 $-\theta_{
m ph}$ 

 $\theta - \theta_B$  (rad)

 $\theta_{
m ph}$ 

Crystal monochromator for bandpass filtering of PXR. (a) Suppressing the noise floor with a monochromator. The PXR beam impacts the monochromator crystal in the Bragg geometry with a central angle  $\theta_B$  relative to the Bragg plane. Due to the PXR spatial dispersion shape, the corresponding frequencies for the emitted angles  $\left[\theta_B - \theta_{\rm ph}, \theta_B + \theta_{\rm ph}\right]$  are  $\left[\omega_B - \Delta\omega, \omega_B + \Delta\omega\right]$ , respectively, where  $\Delta\omega/\omega_B = \theta_{\rm ph}/\tan\theta_B$  (Eq. (6)). If the monochromator has the same parameters as the PXR crystal (i.e., the same material, Bragg angle, Bragg plane), its transfer function overlaps with the incoming beam's spatial dispersion. The non-dispersive arrangement between the PXR crystal and the monochromator preserves the PXR beam exit location under equal rotations of the PXR crystal and of the monochromator, removing the necessity to rotate the whole PXR machine or the target sample during the PXR energy tuning process. (b) The PXR spatial dispersion from a single electron. The intensity is zero in the center frequency  $\omega_R$  due to the PXR symmetry properties. The maximum intensity location is at the emission angles  $\theta_B + \theta_{\rm ph}$  and  $\theta_B - \theta_{\rm ph}$ . When fixing the emission angle, the intrinsic PXR linewidth  $\delta \omega / \omega$  scales as N<sup>-1</sup>, for  $\gamma_e \gg 1$  or else the electron mean-free-path limits the linewidth too. (c) The DuMond diagram of a crystal monochromator. The accepted linewidth for a fixed incident angle is the Darwin width  $\zeta_D$ . The slope of the acceptance region is  $1/\tan\theta_B$ , and the incident beam divergence is  $\theta_{\rm ph}$ ; thus, the emitted spectrum has a linewidth of  $\Delta \omega / \omega_B = \theta_{\rm ph} / \tan \theta_B$ . The monochromator transfer function contains the PXR's spatial dispersion. (d) Illustration of the non-dispersive crystal arrangement in symmetric Bragg geometry. The central axis of the electron beam (blue line) is reflected by the first crystal (the PXR crystal). Then, the x-ray beam would be reflected by the second crystal (the monochromator crystal) and would emerge parallel to the axis of the incident electron beam. An electron incident at an angle  $\Delta \theta_e$  relative to the central ray (purple line) will be Bragg reflected with an angle  $\theta_B$  +  $\Delta\theta_e$  relative to the Bragg plane and with the x-ray energy of  $\omega_B (1 + \Delta \theta_e / \tan \theta_B)$ . Consequently, the emitted x-ray beam will emerge parallel to the deviated incident electron. Panel (b) is adapted from [APL Photonics 6, 070803 (2021)] [161].

condition will be attenuated by the monochromator. Thus, the diffracted intensity of a polychromatic x-ray beam from a monochromator can drop by up to four orders of magnitude, considerably limiting the flux.

**Table 3.** Comparison between Parametric X-Ray (PXR), Inverse Compton Scattering (ICS), and Characteristic Radiation<sup>a</sup>

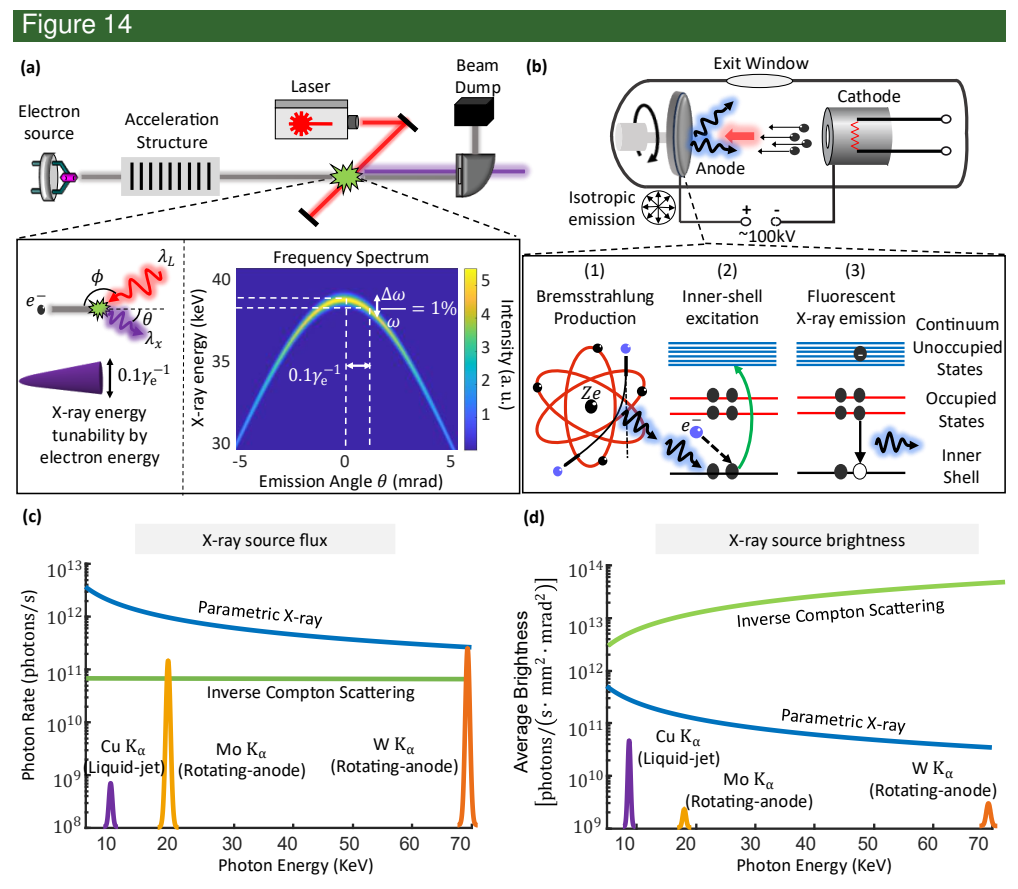
	Parameter	Characteristic X-Ray	Inverse Compton Scattering	Parametric X-Ray	
X-ray beam	Energy tunability	Limited by inner shell transition energies	Electron energy, laser wavelength	Crystal rotation, Bragg plane, PXR material	
	Energy linewidth	<0.1%	~1%	$\theta_D / \tan \theta_B$ (Eq. (6))	
	Emission cone	$4\pi$ sr	$0.1\gamma_{ m e}^{-1}$	$\gamma_{ m e}^{-1}$	
	Spatial dispersion shape	-	Parabolic (Fig. 14(a))	Chirp (Fig. 8), overlaps with a monochromator transfer function	
	Spectral yield	$10^{-7} - 10^{-6}$	10 <sup>-4</sup>	$10^{-5} - 10^{-4}$	
	Average brightness  [ photons   s mm² mrad² ]	$10^{10} - 10^{11}$	$10^{13} - 10^{14}$	$10^{11} - 10^{12}$	
Electron source	Energy	100 keV	8 MeV–50 MeV	50 MeV	
	Normalized emittance	No impact	Impacts the X-ray source emittance and energy linewidth	Less strict requirements than ICS	
	Energy spread	No impact	Impacts the X-ray energy linewidth	Negligible impact	
Machine	Dimensions	Mobile	Table-top	Table-top	
	Operational simplicity	Simple	Spatial and temporal alignment between the laser and electron beams	Spatial alignment only between the electron beam and PXR crystal	
	Neutron radiation safety	No requirements	Neutron shielding, an electron beam deceleration structure		

<sup>&</sup>lt;sup>a</sup>The red, orange, and green colors represent disadvantage, slight advantage, and advantage properties, respectively.

The effectiveness of the double-crystal system for the PXR filtration is possible due to the PXR spatial dispersion (Fig. 13(b)). As discussed in Section 3.5.2, the spatial dispersion of PXR and the transfer function of a crystal monochromator with matching parameters to the PXR crystals almost perfectly align, allowing for an efficient filtration process (Figs. 13(b) and 13(c)). However, according to Eq. (3), there is a slight difference between the PXR frequency and the Bragg frequency reflected by the monochromator [142,232], requiring a small compensation between the two. This difference can be compensated with precise adjustments and fine-tuning of the crystal alignment, i.e., the monochromator crystal is tilted relative to the PXR radiator with a precision on the order of  $\sim 0.01^{\circ}$  [185]. For example, this level of precision is possible by utilizing nano-piezo goniometers [270]. Thus, by carefully optimizing the crystal arrangement, the PXR signal passes through the monochromator with minimal attenuation, while the noise floor is largely filtered out [146,185]. This selective reflection enhances the overall efficiency of the PXR-based x-ray source.

# 6. COMPARISON OF THE LEADING COMPACT HARD X-RAY SOURCES

The leading mechanisms for hard x-ray generation at compact scales are ICS, characteristic radiation produced from an x-ray tube, and PXR. In this section, we compare these mechanisms using the metrics of spectral yield, flux, brightness, and practical application suitability. Specifically, for each mechanism, we analyze the energy tunability, source dimensions, aspects of radiation safety, operational simplicity, and requirements of the active components (i.e., the electron beam and laser sources). Table 3 summarizes this comparison.



Comparison between parametric x-ray (PXR) to inverse Compton scattering (ICS) and characteristic radiation. (a) Inverse Compton scattering x-ray source scheme. A relativistic electron beam collides head-on with a laser pulse, upconverting the laser photon energy to an x-ray photon. Within a narrow emission cone  $\sim 0.1 \gamma_e^{-1}$  in the forward direction, the x-ray beam energy linewidth is 1%. The spatial dispersion of the ICS beam is parabolic. (b) Characteristic radiation production from a rotating anode x-ray tube. Electrons are emitted by thermionic emission from a filament cathode and accelerated to <100 kV. They hit a rotating anode target, producing isotropic bremsstrahlung and characteristic radiation. (c) Flux comparison between PXR, ICS, and characteristic radiation. For the flux derivation, we assume the target angular aperture is 15 mrad. (d) Brightness comparison between PXR, ICS, and characteristic radiation: the characteristic brightness is calculated for the K-line linewidth, the PXR brightness is calculated within the linewidth defined by the emission cone, and the ICS brightness is calculated within 1% linewidth. Table 4 summarizes the experimental parameters used for producing the graphs.

Figure 14 compares the flux and brightness between the PXR, ICS, and characteristiclines x-ray tubes. The PXR source flux is the highest, particularly for lower x-ray energies, i.e., it may serve as a promising imaging technique for applications in this spectral range, such as mammography. The PXR flux decreases at higher energies due to a revield. For comparison, rotating-anode diffraction and liquid-iet x-ray tubes emit radiation mostly at fixed characteristic lines. At higher x-ray energies, their flux can exceed that of PXR sources. Notably, the flux from liquid-jet anodes is generally much lower than that from rotating anodes, which can operate at higher electron beam currents.

When comparing the brightness of the x-ray sources, both ICS and characteristic-lines x-ray tubes based on liquid-jet gain a significant advantage. The ICS brightness increases with the x-ray energy since the ICS beam divergence decreases proportionally to the inverse of the electron energy ( $\gamma_e^{-1}$ ). In contrast, the PXR angular divergence is independent of the emitted x-ray energy, depending instead of the electron beam energy. Altogether, imaging applications require a large field of view and thus the brightness alone is not the critical metric.

# 6.1. Comparison with Inverse Compton Scattering (ICS)

ICS is the up-conversion process of a low-energy laser photon to a high-energy x-ray photon by scattering from a relativistic electron. Figure 14(a) shows the interaction scheme with a near head-on collision between the laser and electron beams. The scattered x-rays emerge in the same direction as the electrons. The physical mechanism of ICS is nearly identical to spontaneous synchrotron emission in a static magnetic undulator as used at traditional synchrotron facilities. However, due to the much shorter micro-meter laser wavelength, relative to the centimeter-period undulator wavelength, the required electron energies to produce hard x-ray photons are orders of magnitude lower than in the large synchrotrons [32].

### 6.1.1. Spatial and Angular Distribution of ICS

The up-conversion ratio for low laser intensity and on-axis emission from a head-on collision is given by [32,33]

$$\lambda_x = \frac{\lambda_L}{4\gamma_e^2} \left( 1 + \gamma_e^2 \theta^2 + \frac{a_0^2}{2} \right),$$
 (19)

where  $\theta$  is the x-ray photon emission angle relative to the electron beam direction,  $a_0 = \frac{eE_0\lambda_L}{2\pi m_ec^2}$  is the dimensionless vector potential of the laser field,  $\lambda_L$  is the laser wavelength, and  $\lambda_x$  is the emitted x-ray wavelength. The dimensionless vector potential value should be well below unity and typically  $a_0 \leq 0.1$  (i.e., the linear ICS approximation) to avoid harmonic powers, and distortion of the energy linewidth [32].

Figure 14(a) shows the ICS parabolic spatial dispersion [32]. The up-conversion ratio (Eq. (19)) implies that all photons emitted within a narrow cone of  $\sim 0.1 \gamma_e^{-1}$  have an energy linewidth of 1%. While the low beam angular divergence is advantageous for high-brightness applications, it is a disadvantage for imaging applications that require a large field of view since it requires a long distance to the target. In addition, the ICS parabolic spatial dispersion does not overlap with the crystal monochromator transfer function, as opposed to the chirp shape of PXR spatial dispersion. Therefore, without appropriate treatment, the ICS beam would be significantly attenuated by the monochromator. A scheme based on a Kirkpatrick–Baez (KB) mirror combined with a double crystal monochromator for focusing and filtering the beam was proposed to cope with this challenge, resulting in a 60% flux reduction [31].

# 6.1.2. Yield of ICS

The total number of ICS photons produced over all angles and frequencies is determined by the cross-section between the electron beam and the laser photons:

$$N_x = \frac{N_{\rm e} N_L \sigma_T}{2\pi \left(\sigma_L^2 + \sigma_{\rm e}^2\right)},\tag{20}$$

where  $\sigma_T$  is the Thomson cross-section,  $N_{\rm e}$  is the total number of electrons,  $N_L$  is the total number of photons in the laser beam, and  $\sigma_L$  and  $\sigma_{\rm e}$  are the beam spot size at the interaction point of the laser and electron beam, respectively. For an ICS scheme with

	Parameter	Characteristic Line (W K <sub>a</sub> )	Characteristic Line (Mo $K_{\alpha}$ )	Characteristic Line (Cu K <sub>α</sub> )	Inverse Compton Scattering	Parametric X-Ray
Material	Target material	Tungsten rotating anode	Molybdenum rotating anode	Copper liquid-jet	-	HOPG/diamond
Electron source	Electron energy	100 keV	100 keV	100 keV	8-50 MeV	50 MeV
	Average electron current	500 mA	500 mA	2 mA	10 μΑ	1 mA
	Electron beam spot size	1 mm	1 mm	10 μm	2 μm	40 μm
	Average current density (mA/mm <sup>2</sup> )	500	500	20,000	2500	600
Laser source	Wavelength	-	-	=	515 nm	=
	Pulse energy	-	-	-	10 mJ	-
	Beam waist	-	-	-	5 μm	-
	Repetition rate	-	-	-	100 KHz	-

Table 4. Parameters Used for Flux and Brightness Calculation

a laser wavelength of  $\lambda_L$  = 515 nm, laser pulse energy of 10 mJ, a laser beam waist of 5 µm, and  $a_0$  = 0.1, the ICS yield is ~10<sup>-3</sup> photons/electron, accounting for the ICS emissions in all directions and all frequencies. However, due to its spatial dispersion, the ICS spectral yield, accounting only for photons emitted at 1% linewidth, is more than an order below [31]. Thus, the ICS spectral yield is comparable with the PXR yield from a HOPG/diamond crystal with an optimal geometry.

### 6.1.3. Challenges with ICS

The ICS scheme requires geometrical and temporal synchronization between high-quality electron and laser beams. For a scattering process such as ICS, the highest flux is produced by squeezing the electron and laser beams into a small spot size with a short duration. In this scheme, the electron source emittance determines the emitted x-ray beam emittance; thus, the electron source emittance must be low, typically a few orders of magnitude lower than the requirement for the PXR source (Section 5.2). Moreover, since the up-conversion ratio is directly proportional to the laser photon energy and the electron beam energy (Eq. (19)), the ICS source must use a low laser linewidth and a low electron beam energy spread to produce a low linewidth x-ray beam [32].

# 6.2. Comparison with Characteristic Radiation

Due to its simplicity, the characteristic radiation produced from an x-ray tube is the most widespread emission mechanism when a monoenergetic x-ray beam is necessary in a laboratory-scale facility. This emission occurs when an electron is accelerated from a hot cathode and impacts a target anode (Fig. 14(b)). The characteristic x-ray photon emission includes inner-shell electron photoionization followed by fluorescence emission. If the kinetic energy of the incident electron is larger than the inner-shell binding energy, it knocks out the inner-shell electron and produces a vacancy. The ionization process can occur either by a direct electron impact or a bremsstrahlung photon. Typically, the inner-shell ionization cross-section by a direct electron impact is two orders of magnitude higher than that of the bremsstrahlung inner-shell ionization cross-section [271]. A comparison of characteristic x-ray radiation yield and PXR yield excited by relativistic electrons in the Si crystal can be found in [106].

### 6.2.1. Yield of Characteristic Radiation

Following ionization, an electron from an outer shell fills the vacancy in the ionized inner shell. In this process, the energy between the two bound states is emitted either in a radiative manner with a characteristic x-ray photon (i.e., a fluorescence process) or by

K-Characteristic Edge Fluorescence  $L(\omega_c^-)$ Line Brightness Material (barns Energy  $(\mu m)$ Yield  $Y_f(Z)$ photons atom  $\left(\frac{1}{\text{s mm}^2\text{mrad}^2}\right)$ (keV) Copper  $3.4\times10^{10}$ 8.979 0.085 3 0.45 300 (liquid-jet anode) Gallium 0.045  $4.6 \times 10^{10}$ 10.36 6.6 0.52 300 (liquid-jet anode) Molybdenum 0.064 19.99 7.7 0.758 100  $9.5 \times 10^{8}$ (rotating-anode) Tungsten 69.52 20.7 0.953 50 0.063  $1.5 \times 10^{9}$ (rotating-anode)

Table 5. Characteristic X-Ray Parameters for Copper, Molybdenum, and Tungsten<sup>a</sup>

a non-radiative process. In the non-radiative process, another bound electron is emitted from the atom, a process known as Auger electron emission [271]. The fluorescence yield,  $Y_f(Z)$ , describes the probability of fluorescence emission as a function of the material's atomic number and can be approximated by [272]

$$Y_f(Z) = Z^4 / (Z^4 + a),$$
 (21)

where  $a = 1.12 \times 10^6$ . Experimental values for the fluorescence yield can be found in online databases [273]. The fluorescence yield increases for higher Z materials; thus, high-Z materials produce more intense characteristic lines.

The total number of emitted characteristic x-rays for the case of direct impact by a single incident electron is defined by the product of the ionization cross-section and the probability for fluorescence emission:

$$N_{chr}^{(t)} = \sigma_{K} n_{a} L\left(\omega_{c}\right) Y_{f}(Z), \qquad (22)$$

where  $\sigma_{\rm K}$  is the cross-section for inner-shell ionization by a direct electron impact for the K-line,  $Y_f(Z)$  is the fluorescence yield,  $n_a$  is the density of the material atoms, and  $L\left(\omega_c\right)$  is the effective interaction length between the incident electron to the material. Typical values for the ionization cross-section of the K-shell  $\sigma_{\rm K}$  are  $\sim 10^{-22} {\rm cm}^2$  for a 100-keV incident electron beam. Equation (22) captures the total number of characteristic x-ray photons emitted in all directions, yet the characteristic radiation is isotropic. Therefore, the x-ray flux collected by a detector with angular aperture  $\theta_D$  and electron source current I is given by

$$\dot{N}_{\rm chr} = N_{\rm chr}^{(t)} \theta_D^2 I/e.$$
 (23)

### 6.2.2. Characteristic Radiation from Different Materials

Table 5 shows the characteristic line emission for different materials, separated into rotating-anode and liquid-jet x-ray tubes. In the conventional solid anode technology, the surface temperature of the anode must be below the melting point to avoid damage. To cope with the thermal load, an x-ray source based on a liquid-jet anode can be used [67–69]. Since the target material is already molten, the requirement for maintaining the target below the melting point is not essential. The current densities achievable by the liquid-jet anode are higher by two orders of magnitude than those of a standard x-ray tube. However, the average current of the liquid-jet x-ray tube is lower than the rotating-anode x-ray tube. Therefore, rotating-anode and liquid-jet x-ray tubes have separate purposes: the liquid-jet anode is optimized for the x-ray source brightness, whereas the rotating anode is optimized for the x-ray source flux.

<sup>&</sup>lt;sup>a</sup>The  $\sigma_K$  values are valid for a 100-keV electron beam energy.

#### 6.2.3. Limitations of Characteristic Radiation

Characteristic radiation is the simplest operational source among the three machines since it requires a low-energy electron beam (<100 keV) without the necessity for any complicated calibration processes. Moreover, its dimensions are the smallest, and the required safety shielding is the least strict due to the low electron acceleration energies (<100 keV). However, the main disadvantages of the characteristic radiation source are the lack of energy tunability and its isotropic emission. The inner shell energies of the target material anode define the emitted x-ray energies. Therefore, the x-ray application defines the anode's material as a function of the desired x-ray energy. For example, copper (8 keV), molybdenum (20 keV), and tungsten (69 keV) are used for x-ray crystallography, mammography, CT, and dental imaging, respectively. This limitation restricts the use of characteristic radiation for many applications, such as K-edge absorption.

### 7. OUTLOOK AND FUTURE RESEARCH DIRECTIONS

Developing a compact and coherent hard x-ray source has been a long-standing challenge and a major research focus in modern physics. This review has examined some of the most promising approaches for achieving this goal, emphasizing sources based on the coherent interaction between free electrons and matter, particularly the PXR mechanism. Recent years have seen significant progress in this field, indicating the potential for transforming these mechanisms into viable practical sources. Notably, the coherent interaction between free electrons and engineered materials has emerged as a promising method for generating tunable, focused x-ray radiation without the need for large-scale facilities. The PXR mechanism, which arises from the coherent excitation of free electrons traversing periodic crystal structures, offers superior spatial coherence, high intensity in a narrow direction, and narrow bandwidth, compared with state-of-the-art x-ray tubes. Recent advances in material engineering techniques have enabled the precise tuning of crystal structures at the atomic scale, allowing for further customization and optimization of the emitted x-ray properties.

Indeed, PXR is a prospective source of quasi-coherent hard x-rays obtainable using relatively modest electron acceleration. Although the PXR source brightness is not as high as x-rays in large facilities (Fig. 3), it has many practical advantages: (1) Its relatively large field of view allows a short distance between the PXR source and the target, facilitating a more compact imaging environment. (2) It was demonstrated in practical applications, such as K-Edge imaging, phase-contrast imaging using differentialenhanced imaging, and computed tomography. (3) Its energy is tunable using crystal rotation, permitting considerable flexibility in selecting the required x-ray energy. Overall, the PXR source can serve for biomedical imaging with a quasi-monochromatic and directional beam, reducing the radiation dose while improving the contrast.

### Prospects for Phase-Contrast Imaging Using PXR

Future work should include research on additional characteristics of the PXR mechanism that are especially important for medical imaging applications. Experiments with lower electron source energies (<10–15 MeV) should be conducted. So far, PXR experiments for imaging applications have shown promising results using electron energies above 50 MeV [72,144,147,149]. However, a PXR source with electron energies below the neutron production threshold has many advantages, mainly less strict radiation shielding requirements and the greater availability of compact electron sources. For example, a medical linear accelerator uses a 20-MeV electron beam for radiotherapy [274]. The main challenges to overcome for lowering the electron beam energy are the higher electron scattering, the x-ray angular divergence, and the x-ray beam linewidth. Yet, these challenges are less severe for lower x-ray energy applications (e.g., mammography). Another approach for radiation reduction is to use an energy-recovery system [145].

Other research directions could use a PXR source with higher average electron beam currents to obtain *in-vivo* imaging. This experiment can also include a study of the PXR beam quality while moving the PXR crystal to help mitigate the electron-induced heat load. While this scheme has the potential to significantly increase the usable PXR flux, it may involve undesired artifacts such as blurring. An additional experimental validation should include the x-ray yield gain due to the usage of advanced crystal geometries in a broad energy spectrum and for different crystal materials.

Prospects for Novel Developments in the PXR Mechanism

Recently, a PXR source based on a laser-plasma electron beam source has been demonstrated [75]. Electron sources based on laser-plasma accelerators usually have high energy spread and large divergence. However, the electron beam energy spread has only a small effect on the PXR emission spectrum. This scheme permits the integration of next-generation plasma-based sources into the PXR scheme, enabling high electron beam energies with compact source dimensions.

Another interesting development would include coherent PXR emission from electrons periodically modulated into micro-bunches matched to the emission wavelength. This approach enables going beyond the traditional PXR scheme analyzed above, in which the emission intensity scales linearly with the electron bunch charge. When the electrons in the bunch emit coherently, the scaling can be quadratic with respect to the number of electrons within a pulse [3]. Recent work proposed testing a scheme of micro-bunched electrons by an XFEL, creating PXR in an extremely asymmetric diffraction configuration, for which the number of produced photons was predicted to be comparable to the XFEL emission [138]. Success in such experiments will pave the way for developing new types of FEL facilities that utilize coherent electron interactions with matter. Future facilities of this kind could rely on PXR with both natural atomic crystals and artificial photonic crystals, to create radiation in a wide range of wavelengths from microwave and optical to x-rays [275,276].

Future research can enhance the PXR yield by accumulating radiation from multiple simultaneous PXR reflections in the same direction and with the same frequency. These emission channels add up coherently even when generated from different crystallographic planes of the crystal. This kind of concept has appeared in studies of the "row effect" [170,225,233] and the "plane effect" [241]. Both effects could be particularly significant at low incident electron beam energies.

An attractive prospect of PXR is the ability to generate multiple x-ray beams. Crystals typically have several crystallographic planes oriented in different directions, resulting in the simultaneous emission of multiple PXR channels, each corresponding to a different plane [192]. Thus, PXR offers a unique opportunity to create a facility capable of producing several x-ray beams simultaneously. This facility can function similarly to a storage ring, where multiple x-ray beams are emitted simultaneously from different stations. However, in this case, all PXR beams originate from a single crystal. A key advantage of such a multi-PXR beam facility is the relative coherence of all the beams, as they are produced by the same electrons interacting with the same crystal structure. This coherence offers opportunities for interferometry and pump-probe experiments with femtosecond and even attosecond time delays, depending on the pulsed nature of the incident electron beam.

An exciting research direction focuses on the fundamental study of evanescent PXR [277]. This approach aims to explore x-ray evanescent waves generated by an x-ray beam interacting at a grazing angle with a material surface. Previous studies produced evanescent x-rays through characteristic x-ray radiation, where accelerated charged particles interacted at grazing angles with an amorphous target surface, resulting in isotropic emission. In the proposed PXR evanescent scheme, the standard PXR mechanism is employed, where the emitted PXR beam forms at a grazing angle relative to the surface of the PXR crystal. This beam can be generated using either Bragg or Laue geometries. Unlike characteristic x-ray radiation, PXR offers significant advantages due to its highly directional nature and the ability to experimentally tune its energy and polarization. In addition, advancing the understanding of evanescent PXR could enable control over its angular distribution, unlocking potential practical applications. One promising application is the development of x-ray optics that eliminate the need for external optical components.

Finally, an intriguing development in the PXR mechanism that can be incorporated into future PXR sources is x-ray focusing by bent crystals [73,74,191]. Conventional optical focusing components used in the x-ray spectrum are highly lossy. In contrast, a coherent interaction between the electron and the bent crystal produces a PXR beam whose phase front is curved, causing the x-ray beam to self-focus and potentially replacing the need for additional x-ray optical components.

### **FUNDING**

United States-Israel Binational Science Foundation (BSF) (2022144); the Israel Science Foundation (ISF) (385/23).

### **ACKNOWLEDGMENT**

A.V.S. is thankful for the funding through the MSCA4Ukraine project #1233244, which is funded by the European Union. L.J.W. acknowledges support from the National Research Foundation, Singapore (Project ID NRF2020-NRF-ISF004-3525) and the Ministry of Education, Singapore, under its AcRF Tier 2 programme (Award No. MOE-T2EP50222-0012).

#### **DISCLOSURES**

The authors declare no conflicts of interest.

### **DATA AVAILABILITY**

The data and codes that support the findings of this study are available from the corresponding author upon reasonable request.

### **REFERENCES**

- 1. W. Röntgen, "On a new kind of rays," Science 3, 227–231 (1896).
- 2. C. Feng and H.-X. Deng, "Review of fully coherent free-electron lasers," Nucl. Sci. Tech. 29, 160 (2018).
- 3. C. Pellegrini, A. Marinelli, and S. Reiche, "The physics of x-ray free-electron lasers," Rev. Mod. Phys. 88, 15006 (2016).

- 4. N. H. Burnett, H. A. Baldis, M. C. Richardson, *et al.*, "Harmonic generation in CO<sub>2</sub> laser target interaction," Appl. Phys. Lett. **31**, 172–174 (1977).
- 5. A. McPherson, G. Gibson, H. Jara, *et al.*, "Studies of multiphoton production of vacuum-ultraviolet radiation in the rare gases," J. Opt. Soc. Am. B **4**, 595 (1987).
- 6. M. Ferray, A. L'Huillier, X. F. Li, *et al.*, "Multiple-harmonic conversion of 1064 nm radiation in rare gases," J. Phys. B: At. Mol. Opt. Phys. **21**, L31–L35 (1988).
- 7. X. F. Li, A. L'Huillier, M. Ferray, *et al.*, "Multiple-harmonic generation in rare gases at high laser intensity," Phys. Rev. A **39**, 5751–5761 (1989).
- 8. M. Lewenstein, P. Balcou, M. Y. Ivanov, *et al.*, "Theory of high-harmonic generation by low-frequency laser fields," Phys. Rev. A **49**, 2117–2132 (1994).
- 9. J. Seres, E. Seres, A. J. Verhoef, *et al.*, "Source of coherent kiloelectronvolt x-rays," Nature **433**, 596 (2005).
- 10. C. Winterfeldt, C. Spielmann, and G. Gerber, "Colloquium: optimal control of high-harmonic generation," Rev. Mod. Phys. **80**, 117–140 (2008).
- 11. T. Popmintchev, M.-C. Chen, A. Bahabad, *et al.*, "Phase matching of high harmonic generation in the soft and hard x-ray regions of the spectrum," Proc. Natl. Acad. Sci. **106**, 10516–10521 (2009).
- 12. T. Popmintchev, M.-C. Chen, D. Popmintchev, *et al.*, "Bright coherent ultrahigh harmonics in the keV x-ray regime from mid-infrared femtosecond lasers," Science **336**, 1287–1291 (2012).
- 13. O. Jahn, V. E. Leshchenko, P. Tzallas, *et al.*, "Towards intense isolated attosecond pulses from relativistic surface high harmonics," Optica **6**, 280 (2019).
- 14. A. Gorlach, M. E. Tzur, M. Birk, *et al.*, "High-harmonic generation driven by quantum light," Nat. Phys. **19**, 1689–1696 (2023).
- 15. D. Castelvecchi and K. Sanderson, "Physicists who built ultrafast 'attosecond' lasers win Nobel prize," Nature **622**, 225–227 (2023).
- 16. E. J. Takahashi, P. Lan, O. D. Mücke, *et al.*, "Attosecond nonlinear optics using gigawatt-scale isolated attosecond pulses," Nat. Commun. **4**, 2691 (2013).
- 17. T. Tajima and J. M. Dawson, "Laser electron accelerator," Phys. Rev. Lett. 43, 267–270 (1979).
- 18. C. Joshi, W. B. Mori, T. Katsouleas, *et al.*, "Ultrahigh gradient particle acceleration by intense laser-driven plasma density waves," Nature **311**, 525–529 (1984).
- 19. M. Kando, Y. Fukuda, A. S. Pirozhkov, *et al.*, "Demonstration of laser-frequency upshift by electron-density modulations in a plasma wakefield," Phys. Rev. Lett. **99**, 135001 (2007).
- 20. V. Petrillo, L. Serafini, and P. Tomassini, "Ultrahigh brightness electron beams by plasma-based injectors for driving all-optical free-electron lasers," Phys. Rev. ST Accel. Beams 11, 70703 (2008).
- 21. E. Esarey, C. B. Schroeder, and W. P. Leemans, "Physics of laser-driven plasmabased electron accelerators," Rev. Mod. Phys. **81**, 1229–1285 (2009).
- 22. S. Corde, K. T. Phuoc, G. Lambert, *et al.*, "Femtosecond x rays from laser-plasma accelerators," Rev. Mod. Phys. **85**, 1–48 (2013).
- 23. C. Thaury, E. Guillaume, A. Döpp, *et al.*, "Demonstration of electron beam focusing by a laser-plasma lens," Nat. Commun. **6**, 6860 (2015).
- 24. D. E. Rivas, A. Borot, D. E. Cardenas, *et al.*, "Next generation driver for attosecond and laser-plasma physics," Sci. Rep. **7**, 5224 (2017).
- 25. A. R. Maier, N. Kajumba, A. Guggenmos, *et al.*, "Water-window x-ray pulses from a laser-plasma driven undulator," Sci. Rep. **10**, 5634 (2020).
- 26. C. Emma, J. Van Tilborg, R. Assmann, *et al.*, "Free electron lasers driven by plasma accelerators: status and near-term prospects," High Power Laser Sci. Eng. **9**, e57 (2021).

- 27. F. Albert, "Principles and applications of x-ray light sources driven by laser Wakefield acceleration," Phys. Plasmas **30**, 050902 (2023).
- 28. A. Döpp, L. Hehn, J. Götzfried, *et al.*, "Quick x-ray microtomography using a laser-driven betatron source," Optica **5**, 199 (2018).
- 29. B. Hornberger, J. Kasahara, R. Ruth, *et al.*, "Inverse Compton scattering x-ray source for research, industry and medical applications," in *International Conference on X-Ray Lasers* 2020 (SPIE, 2021), Vol. **11886**, pp. 51–60.
- 30. V. Muşat, A. Latina, and G. D'Auria, "A high-energy and high-intensity inverse Compton scattering source based on CompactLight technology," Photonics 9, 308 (2022).
- 31. W. S. Graves, J. Bessuille, P. Brown, *et al.*, "Compact x-ray source based on burst-mode inverse Compton scattering at 100 kHz," Phys. Rev. ST Accel. Beams 17, 120701 (2014).
- 32. W. J. Brown and F. V. Hartemann, "Three-dimensional time and frequency-domain theory of femtosecond x-ray pulse generation through Thomson scattering," Phys. Rev. ST Accel. Beams **7**, 60703 (2004).
- 33. S. K. Ride, E. Esarey, and M. Baine, "Thomson scattering of intense lasers from electron beams at arbitrary interaction angles," Phys. Rev. E **52**, 5425–5442 (1995).
- 34. B. H. Schaap, C. W. Sweers, P. W. Smorenburg, *et al.*, "Ponderomotive bunching of a relativistic electron beam for a superradiant Thomson source," Phys. Rev. Accel. Beams **26**, 74401 (2023).
- 35. A. W. Sáenz, H. Überall, and J. U. Andersen, *Coherent Radiation Sources* (Springer, 1985).
- 36. A. Potylitsyn, *Electromagnetic Radiation of Electrons in Periodic Structures* (Springer Science Business Media, 2011), Vol. **243**.
- 37. Z. Duan, B.-I. Wu, J. Lu, *et al.*, "Cherenkov radiation in anisotropic double-negative metamaterials," Opt. Express **16**, 18479–18484 (2008).
- 38. Z. Duan, B.-I. Wu, S. Xi, *et al.*, "Research progress in reversed Cherenkov radiation in double-negative metamaterials," Prog. Electromagn. Res. **90**, 75–87 (2009).
- 39. Z. Duan, Y. Wang, X. Mao, *et al.*, "Experimental demonstration of double-negative metamaterials partially filled in a circular waveguide," Prog. Electromagn. Res. **121**, 215–224 (2011).
- 40. L. J. Wong, I. Kaminer, O. Ilic, *et al.*, "Towards graphene plasmon-based free-electron infrared to x-ray sources," Nat. Photonics **10**, 46–52 (2016).
- 41. Z. Su, B. Xiong, Y. Xu, *et al.*, "Manipulating Cherenkov radiation and Smith–Purcell radiation by artificial structures," Adv. Opt. Mater. **7**, 1801666 (2019).
- 42. G. Rosolen, L. J. Wong, N. Rivera, *et al.*, "Metasurface-based multi-harmonic free-electron light source," Light: Sci. Appl. 7, 64 (2018).
- 43. A. Pizzi, G. Rosolen, L. J. Wong, *et al.*, "Graphene metamaterials for intense, tunable, and compact extreme ultraviolet and X-ray sources," Adv. Sci. 7, 1901609 (2020).
- 44. R. J. Parmee, C. M. Collins, W. I. Milne, *et al.*, "X-ray generation using carbon nanotubes," Nano Converg. **2**, 1 (2015).
- 45. V. Karagodsky and L. Schächter, "High efficiency x-ray source based on inverse Compton scattering in an optical Bragg structure," Plasma Phys. Control Fusion 53, 014007 (2011).
- 46. V. Karagodsky, D. Schieber, and L. Schächter, "Enhancing x-ray generation by electron-beam—laser interaction in an optical Bragg structure," Phys. Rev. Lett. **104**, 024801 (2010).

- L. Schächter and W. D. Kimura, "Vacuum channeling radiation by relativistic electrons in a transverse field of a laser-based Bessel beam," Phys. Rev. Lett. 114, 195501 (2015).
- 48. Z. Toroker and L. Schächter, "Deep saturation of a Cerenkov wakefield amplified by an active medium," Phys. Rev. Spec. Top.-Accel. Beams **18**, 071301 (2015).
- 49. T. Plettner and R. L. Byer, "Proposed dielectric-based microstructure laser-driven undulator," Phys. Rev. Spec. Top.-Accel. Beams 11, 030704 (2008).
- 50. W. S. Graves, W. Brown, F. X. Kaertner, *et al.*, "MIT inverse Compton source concept," Nucl. Instrum. Methods Phys. Res. A **608**, S103–S105 (2009).
- F. Albert and A. G. R. Thomas, "Applications of laser Wakefield acceleratorbased light sources," Plasma Phys. Control Fusion 58, 103001 (2016).
- 52. D. Zhang, A. Fallahi, M. Hemmer, *et al.*, "Segmented terahertz electron accelerator and manipulator (STEAM)," Nat. Photonics **12**, 336–342 (2018).
- 53. B. H. Schaap, P. W. Smorenburg, and O. J. Luiten, "Few-cycle vortices from superradiant nonlinear Thomson scattering by a relativistic chirped mirror," Phys. Rev. Res. 5, L032034 (2023).
- 54. N. Rivera, L. J. Wong, J. D. Joannopoulos, *et al.*, "Light emission based on nanophotonic vacuum forces," Nat. Phys. **15**, 1284–1289 (2019).
- 55. L. J. Wong and I. Kaminer, "Prospects in x-ray science emerging from quantum optics and nanomaterials," Appl. Phys. Lett. **119**, 130502 (2021).
- 56. L. J. Wong, N. Rivera, C. Murdia, *et al.*, "Control of quantum electrodynamical processes by shaping electron wavepackets," Nat. Commun. **12**, 1700 (2021).
- 57. J. Lim, S. Kumar, Y. S. Ang, *et al.*, "Quantum interference between fundamentally different processes is enabled by shaped input wavefunctions," Adv. Sci. **10**, 2205750 (2023).
- 58. L. W. W. Wong, X. Shi, A. Karnieli, *et al.*, "Free-electron crystals for enhanced x-ray radiation," Light: Sci. Appl. **13**, 29 (2024).
- 59. S. Kumar, J. Lim, N. Rivera, *et al.*, "Strongly correlated multielectron bunches from interaction with quantum light," Sci. Adv. **10**, eadm9563 (2024).
- 60. S. Huang, R. Duan, N. Pramanik, *et al.*, "Multicolor x-rays from free electron-driven van der Waals heterostructures," Sci. Adv. **9**, eadj8584 (2023).
- 61. M. Shentcis, A. K. Budniak, X. Shi, *et al.*, "Tunable free-electron x-ray radiation from van der Waals materials," Nat. Photonics **14**, 686–692 (2020).
- 62. S. Huang, R. Duan, N. Pramanik, *et al.*, "Enhanced versatility of table-top x-rays from van der Waals structures," Adv. Sci. **9**, 2105401 (2022).
- 63. A. Karnieli, D. Roitman, M. Liebtrau, *et al.*, "Cylindrical metalens for generation and focusing of free-electron radiation," Nano Lett. **22**, 5641–5650 (2022).
- 64. Y. Yang, C. Roques-Carmes, S. E. Kooi, *et al.*, "Photonic flatband resonances for free-electron radiation," Nature **613**, 42–47 (2023).
- 65. H. Labriet, C. Nemoz, M. Renier, *et al.*, "Significant dose reduction using synchrotron radiation computed tomography: first clinical case and application to high resolution CT exams," Sci. Rep. **8**, 12491 (2018).
- 66. W. R. Hendee, E. R. Ritenour, and K. R. Hoffmann, *Medical Imaging Physics*, 4th ed. (Wiley-Liss, 2003), Vol. **30**, p. 536.
- 67. O. Hemberg, M. Otendal, and H. M. Hertz, "Liquid-metal-jet anode electron-impact x-ray source," Appl. Phys. Lett. **83**, 1483–1485 (2003).
- 68. T. Tuohimaa, M. Otendal, and H. M. Hertz, "Phase-contrast x-ray imaging with a liquid-metal-jet-anode microfocus source," Appl. Phys. Lett. **91**, 074104 (2007).
- 69. M. Otendal, T. Tuohimaa, U. Vogt, *et al.*, "A 9keV electron-impact liquid-gallium-jet x-ray source," Rev. Sci. Instrum. **79**, 16102 (2008).
- 70. S. W. Wilkins, T. E. Gureyev, D. Gao, *et al.*, "Phase-contrast imaging using polychromatic hard x-rays," Nature **384**, 335–338 (1996).

- 71. M. Endrizzi, "X-ray phase-contrast imaging," Nucl. Instrum. Methods Phys. Res. A **878**, 88–98 (2018).
- 72. Y. Takahashi, Y. Hayakawa, T. Kuwada, *et al.*, "Parametric x-ray radiation as a novel source for x-ray imaging," X-Ray Spectrom. **41**, 210–215 (2012).
- 73. X. Shi, M. Shentcis, Y. Kurman, *et al.*, "Free-electron-driven x-ray caustics from strained van der Waals materials," Optica **10**, 292 (2023).
- 74. X. Shi, Y. Kurman, M. Shentcis, *et al.*, "Free-electron interactions with van der Waals heterostructures: a source of focused x-ray radiation," Light: Sci. Appl. **12**, 148 (2023).
- 75. A. Curcio, M. Ehret, J. A. Perez-Hernandez, *et al.*, "Observation of tunable parametric x-ray radiation emitted by laser-plasma electron beams interacting with crystalline structures," Phys. Rev. Accel. Beams **25**, 63403 (2022).
- 76. V. L. Ginzburg, "Quantum theory of radiation of electron uniformly moving in medium," Zh. Eksp. Teor. Fiz. **10**, 589 (1940).
- 77. R. T. Cox, "Momentum and energy of photon and electron in the Čerenkov radiation," Phys. Rev. **66**, 106–107 (1944).
- 78. V. L. Ginzburg, "Radiation by uniformly moving sources (Vavilov–Cherenkov effect, transition radiation, and other phenomena)," Phys. Uspekhi **39**, 973–982 (1996).
- 79. I. Kaminer, M. Mutzafi, A. Levy, *et al.*, "Quantum Čerenkov radiation: spectral cutoffs and the role of spin and orbital angular momentum," Phys. Rev. X 6, 011006 (2016).
- 80. I. Kaminer, S. E. Kooi, R. Shiloh, *et al.*, "Spectrally and spatially resolved Smith-Purcell radiation in plasmonic crystals with short-range disorder," Phys. Rev. X 7, 011003 (2017).
- 81. K. B. Korotchenko, Y. L. Pivovarov, and Y. Takabayashi, "Quantum effects for parametric x-ray radiation during channeling: theory and first experimental observation," JETP Lett. **95**, 433–437 (2012).
- 82. S. Huang, R. Duan, N. Pramanik, *et al.*, "Quantum recoil in free-electron interactions with atomic lattices," Nat. Photonics **17**, 224–230 (2023).
- 83. A. V. Shchagin, "Current status of parametric x-ray radiation research," Radiat. Phys. Chem. **61**, 283–291 (2001).
- 84. V. Baryshevsky, I. Feranchuk, and A. Ulyanenkov, "Parametric x-ray radiation in crystals: theory, experiments and applications," Springer Tr. Mod. Phys. **213**, 1 (2005).
- 85. E. Prat, R. Abela, M. Aiba, *et al.*, "A compact and cost-effective hard x-ray free-electron laser driven by a high-brightness and low-energy electron beam," Nat. Photonics **14**, 748–754 (2020).
- 86. J. Als-Nielsen and D. McMorrow, *Elements of Modern X-Ray Physics*, 2nd ed. (John Wiley Sons, 2011).
- 87. L. Zhang, Z. Li, D. Liu, *et al.*, "Entangled x-ray photon pair generation by free-electron lasers," Phys. Rev. Lett. **131**, 073601 (2023).
- 88. X. Shi, R. Ruimy, A. Balanov, *et al.*, "Electron-heralded quantum x-ray source," in *CLEO: Fundamental Science* (Optica Publishing Group, 2024), p. FM4B-5.
- 89. I. Freund and B. F. Levine, "Parametric conversion of X rays," Phys. Rev. Lett. 23, 854–857 (1969).
- 90. P. Eisenberger and S. L. McCall, "x-ray parametric conversion," Phys. Rev. Lett. **26**, 684–688 (1971).
- 91. S. Shwartz and S. E. Harris, "Polarization entangled photons at x-ray energies," Phys. Rev. Lett. **106**, 080501 (2011).
- 92. S. Shwartz, R. N. Coffee, J. M. Feldkamp, *et al.*, "X-ray parametric down-conversion in the Langevin regime," Phys. Rev. Lett. **109**, 013602 (2012).

- 93. L. Zhang, L. Zhao, H. Xu, *et al.*, "Terahertz quantum illumination using free-electron lasers," Phys. Rev. Appl. **21**, 064021 (2024).
- 94. R. R. Lindberg, K.-J. Kim, Y. Shvyd'Ko, *et al.*, "Performance of the x-ray free-electron laser oscillator with crystal cavity," Phys. Rev. Spec. Top.-Accel. Beams **14**, 010701 (2011).
- 95. K. Li, J. Yan, C. Feng, *et al.*, "High brightness fully coherent x-ray amplifier seeded by a free-electron laser oscillator," Phys. Rev. Accel. Beams **21**, 40702 (2018).
- 96. B. Adams, G. Aeppli, T. Allison, *et al.*, "Scientific opportunities with an x-ray free-electron laser oscillator," arXiv (2019).
- 97. K.-J. Kim and Y. V. Shvyd'ko, "Tunable optical cavity for an x-ray free-electron-laser oscillator," Phys. Rev. Spec. Top.-Accel. Beams **12**, 30703 (2009).
- 98. E. A. Nanni, W. S. Graves, and D. E. Moncton, "Nanomodulated electron beams via electron diffraction and emittance exchange for coherent x-ray generation," Phys. Rev. Accel. Beams **21**, 014401 (2018).
- 99. W. S. Graves, F. X. Kaertner, D. E. Moncton, *et al.*, "Intense super-radiant x-rays from a compact source using a nanocathode array and emittance exchange," arXiv (2012).
- 100. J. Gea-Banacloche, G. T. Moore, R. R. Schlicher, et al., "Proposal for a compact FEL with electromagnetic-wave undulator," Nucl. Instrum. Methods Phys. Res. A 272, 199–205 (1988).
- A. Bacci, C. Maroli, V. Petrillo, *et al.*, "Compact x-ray free-electron laser based on an optical undulator," Nucl. Instrum. Methods Phys. Res. A 587, 388–397 (2008).
- 102. A. Balanov, R. Ruimy, and I. Kaminer, "Toward high-gain laser-driven electron undulators," Optica 12, 360 (2025).
- 103. W. Knulst, O. J. Luiten, M. J. van der Wiel, *et al.*, "Observation of narrow-band Si L-edge Čerenkov radiation generated by 5 MeV electrons," Appl. Phys. Lett. **79**, 2999–3001 (2001).
- 104. W. Knulst, M. J. van der Wiel, O. J. Luiten, *et al.*, "High-brightness, narrowband, and compact soft x-ray Cherenkov sources in the water window," Appl. Phys. Lett. **83**, 4050–4052 (2003).
- 105. V. L. Ginzburg and I. M. Frank, "Radiation of a uniformly moving electron due to its transition from one medium into another," J. Phys. (USSR) **9**, 353 (1945).
- 106. I. Chaikovska, R. Chehab, X. Artru, et al., "Characteristic, parametric, and diffracted transition x-ray radiation for observation of accelerated particle beam profile," Nucl. Instrum. Methods Phys. Res. B 402, 75–78 (2017).
- 107. A. V. Berdnichenko, A. V. Budko, V. V. Kolodochkin, et al., "Influence of the reflectivity of a crystal on the angular distribution of diffracted transition radiation of relativistic electrons," J. Instrum. 19, C05043 (2024).
- 108. J. U. Andersen, E. Bonderup, and R. H. Pantell, "Channeling radiation," Ann. Rev. Nucl. Part. Sci. 33, 453–504 (1983).
- 109. S. Bellucci, S. Bini, V. M. Biryukov, *et al.*, "Experimental study for the feasibility of a crystalline undulator," Phys. Rev. Lett. **90**, 034801 (2003).
- 110. C. A. Brau, B.-K. Choi, J. D. Jarvis, *et al.*, "Channeling radiation as a source of hard x-rays with high spectral brilliance," Synchrotron Radiat. News **25**, 20–24 (2012).
- 111. U. Timm, "Coherent Bremsstrahlung of electrons in crystals," Fortschr. Der Phys. 17, 765–808 (1969).
- 112. S. M. Cavaletto, Z. Harman, C. Ott, *et al.*, "Broadband high-resolution x-ray frequency combs," Nat. Photonics **8**, 520–523 (2014).
- 113. S. Suckewer and P. Jaeglé, "X-ray laser: past, present, and future," Laser Phys. Lett. **6**, 411–436 (2009).

- 114. G. Chapline and L. Wood, "X-ray lasers," Phys. Today 28, 40–48 (1975).
- 115. J. D. Jackson, *Classical Electrodynamics*, 3rd ed. (John Wiley Sons, 1998), p. 832.
- 116. V. A. Bazylev, V. I. Glebov, E. I. Denisov, *et al.*, "Cherenkov radiation as an intensive x-ray source, Zh," Eksp. Teor. Fiz., Pis' Ma Red. (USSR) **24**, 371 (1976).
- 117. K.-J. Kim, Y. Shvyd'ko, and S. Reiche, "A proposal for an x-ray free-electron laser oscillator with an energy-recovery Linac," Phys. Rev. Lett. **100**, 244802 (2008).
- 118. R. Margraf, R. Robles, A. Halavanau, *et al.*, "Low-loss stable storage of 1.2 Å x-ray pulses in a 14 m Bragg cavity," Nat. Photonics **17**, 878–882 (2023).
- 119. A. Momose, "Recent advances in x-ray phase imaging," Jpn. J. Appl. Phys. 44, 6355 (2005).
- 120. L. Young, K. Ueda, M. Gühr, *et al.*, "Roadmap of ultrafast x-ray atomic and molecular physics," J. Phys. B: At. Mol. Opt. Phys. **51**, 032003 (2018).
- 121. M. Holler, M. Guizar-Sicairos, E. H. R. Tsai, *et al.*, "High-resolution non-destructive three-dimensional imaging of integrated circuits," Nature **543**, 402–406 (2017).
- 122. T. H. Maiman, "Stimulated optical radiation in ruby," Nature **187**, 493–494 (1960).
- 123. J. Hecht, "The history of the x-ray laser," Opt. Photonics News 19, 26 (2008).
- 124. A. Halavanau, A. Benediktovitch, A. A. Lutman, *et al.*, "Population inversion x-ray laser oscillator," Proc. Natl. Acad. Sci. U.S.A. **117**, 15511–15516 (2020).
- 125. P. A. Cerenkov, "Visible emission of clean liquids by action of  $\gamma$  radiation," Dokl. Akad. Nauk SSSR **2**, 451–454 (1934).
- 126. S. J. Smith and E. M. Purcell, "Visible light from localized surface charges moving across a grating," Phys. Rev. **92**, 1069–1069 (1953).
- 127. Y. B. Fainberg and N. A. Khizhnyak, "Energy losses of charged particles passing through layered dielectric," Zh. Eksper. Teor. Fiz. **32**, 883 (1957).
- 128. E. J. Williams, "Nature of the high energy particles of penetrating radiation and status of ionization and radiation formulae," Phys. Rev. 45, 729–730 (1934).
- 129. W. Heitler, The Quantum Theory of Radiation (Courier Corporation, 1984).
- 130. H. Überall, "High-energy interference effect of bremsstrahlung and pair production in crystals," Phys. Rev. **103**, 1055–1067 (1956).
- 131. M. A. Kumakhov, "On the theory of electromagnetic radiation of charged particles in a crystal," Phys. Lett. A 57, 17–18 (1976).
- 132. R. W. Terhune and R. H. Pantell, "X-ray and  $\gamma$ -ray emission from channeled relativistic electrons and positrons," Appl. Phys. Lett. **30**, 265–268 (1977).
- 133. A. Shchagin, G. Kube, A. Potylitsyn, *et al.*, "Frequency splitting in undulator radiation from solid-state crystalline undulator," J. Instrum. **19**, C05045 (2024).
- 134. V. G. Baryshevsky and I. D. Feranchuk, "A comparative analysis of various mechanisms for the generation of x-rays by relativistic particles," Nucl. Inst. Methods Phys. Res. A **228**, 490–495 (1985).
- 135. F. J. García de Abajo, "Colloquium: light scattering by particle and hole arrays," Rev. Mod. Phys. **79**, 1267–1290 (2007).
- 136. Y. Hayakawa, Y. Takahashi, T. Kuwada, *et al.*, "x-ray imaging using a tunable coherent x-ray source based on parametric x-ray radiation," J. Instrum. **8**, C08001 (2013).
- 137. A. N. Didenko, B. N. Kalinin, S. Pak, *et al.*, "Observation of monochromatic x-ray radiation from 900 MeV electrons transmitting through a diamond crystal," Phys. Lett. A **110**, 177–179 (1985).
- 138. I. D. Feranchuk, N. Q. San, and O. D. Skoromnik, "Superradiant parametric x-ray emission," Phys. Rev. Accel. Beams 25, 120702 (2022).

- 139. A. V. Shchagin and G. Kube, "Frequency of parametric x-ray radiation," Problems At. Sci. Technol. 4, 85–87 (2023).
- 140. V. Alekseev, A. Eliseyev, E. Irribarra, *et al.*, "Parametric x-ray radiation in polycrystals," Probl. Atom. Sci. Tech. **122**, 187–190 (2019).
- 141. V. I. Alekseev, A. N. Eliseyev, E. Irribarra, *et al.*, "Parametric x-ray radiation from powders," Phys. Lett. A **383**, 770–773 (2019).
- 142. A. V. Shchagin, "Fresnel coefficients for parametric x-ray (Cherenkov) radiation," Phys.-Usp. **58**, 819–827 (2015).
- 143. K. B. Korotchenko, Y. L. Eikhorn, and S. B. Dabagov, "Fine features of parametric x-ray radiation by relativistic electrons and ions," Phys. Lett. B **774**, 470–475 (2017).
- 144. H. Okada, T. Kaneda, K. Sekiya, *et al.*, "Basic study of parametric x-ray radiation for clinical diagnosis using 125 MeV linear particle accelerator," J. Hard Tissue Biol. **24**, 299–302 (2015).
- 145. J. Hyun, M. Satoh, M. Yoshida, *et al.*, "Compact and intense parametric x-ray radiation source based on a linear accelerator with cryogenic accelerating and decelerating copper structures," Phys. Rev. Accel. Beams **21**, 14701 (2018).
- 146. A. Balanov, A. Gorlach, and I. Kaminer, "Breaking the barriers of electron-driven x-ray radiation in crystals," APL Photonics **9**, 076101 (2024).
- 147. Y. Hayakawa, K. Hayakawa, M. Inagaki, *et al.*, "Computed tomography for light materials using a monochromatic x-ray beam produced by parametric x-ray radiation," Nucl. Instrum. Methods Phys. Res. B **309**, 230–236 (2013).
- 148. Y. Hayakawa, K. Hayakawa, M. Inagaki, *et al.*, "Element-sensitive computed tomography by fine tuning of PXR-based x-ray source," Nucl. Instrum. Methods Phys. Res. B **355**, 251–256 (2015).
- 149. Y. Hayakawa, K. Hayakawa, T. Kaneda, et al., "Simultaneous K-edge subtraction tomography for tracing strontium using parametric x-ray radiation," Nucl. Instrum. Methods Phys. Res. B 402, 228–231 (2017).
- 150. A. Opanasenko, V. Mytrochenko, V. Zhaunerchyk, *et al.*, "Design study of a low-emittance high-repetition rate thermionic RF gun," Phys. Rev. Accel. Beams **20**, 053401 (2017).
- 151. P. Musumeci, J. Giner Navarro, J. B. Rosenzweig, *et al.*, "Advances in bright electron sources," Nucl. Instrum. Methods Phys. Res. A **907**, 209–220 (2018).
- 152. Y. Hayakawa, K. Hayakawa, M. Inagaki, *et al.*, "Geometrical effect of target crystal on PXR generation as a coherent x-ray source," in *AIP Conference Proceedings* (2010), pp. 677–680.
- 153. I. D. Feranchuk and S. I. Feranchuk, "Grazing incidence parametric x-ray radiation from the relativistic electron beam moving in parallel to the superlattice surface," Eur. Phys. J. Appl. Phys. **38**, 135–140 (2007).
- 154. O. D. Skoromnik, V. G. Baryshevsky, A. P. Ulyanenkov, *et al.*, "Radical increase of the parametric x-ray intensity under condition of extremely asymmetric diffraction," Nucl. Instrum. Methods Phys. Res. B **412**, 86–92 (2017).
- 155. A. N. Eliseev, A. S. Kubankin, R. M. Nazhmudinov, et al., "Observation of the enhancement of parametric radiation under conditions of the grazing incidence of relativistic electrons on the crystal surface," JETP Lett. 90, 438–440 (2009).
- 156. T. Akimoto, M. Tamura, J. Ikeda, *et al.*, "Generation and use of parametric x-rays with an electron linear accelerator," Nucl. Instrum. Methods Phys. Res. A **459**, 78–86 (2001).
- 157. Y. Adishev, V. Zabaev, V. Kaplin, *et al.*, "Parametric x-ray radiation generated by 5.7-MeV electrons in a pyrolytic-graphite crystal," Phys. At. Nucl. **66**, 420–422 (2003).

- 158. D. I. Adejshvili, S. V. Blazhevich, B. F. Boldyshev, *et al.*, "Hard x-ray spectra of high-energy electrons in crystal at Bragg angle," Dokl. Akad. Nauk. SSSR **298**, 844 (1988).
- 159. V. L. Morokhovskii and A. V. Shchagin, "Study of the coherence properties of parametric radiation," Sov. Phys. Tech. Phys. **35**, 623 (1990).
- 160. Y. Hayakawa, K. Hayakawa, M. Inagaki, et al., "Advanced applications of PXR at LEBRA, Nihon University," in *International Conference on Charged* and Neutral Particles Channeling Phenomena II (SPIE, 2007), Vol. 6634, pp. 346–355.
- 161. A. Balanov, A. Gorlach, and I. Kaminer, "Temporal and spatial design of x-ray pulses based on free-electron–crystal interaction," APL Photonics **6**, 70803 (2021).
- 162. G. M. Garibyan and C. Yang, "Quantum microscopic theory of radiation by a charged particle moving uniformly in a crystal," Sov. Phys. JETP **34**, 495 (1972).
- 163. V. G. Baryshevsky and I. D. Feranchuk, "The x-ray radiation of ultrarelativistic electrons in a crystal," Phys. Lett. A **57**, 183–185 (1976).
- 164. L. A. Vardanyan, G. M. Garibyan, and C. Yang, "Radiation of an ultrarelativistic charge in an absorbing plate with taking into account multiple scattering," Izv. Akad. Nauk Arm. SSR Ser. Fiz. 11, 329 (1976).
- 165. V. G. Baryshevsky and I. D. Feranchuk, "Parametric x-rays from ultrarelativistic electrons in a crystal: theory and possibilities of practical utilization," J. Phys. France **44**, 913–922 (1983).
- 166. V. G. Baryshevsky and I. D. Feranchuk, "Transition radiation of  $\gamma$  rays in a crystal," Sov. Phys. JETP **34**, 502 (1972).
- 167. M. L. Ter-Mikaelian, "High-energy electromagnetic processes in condensed media" (Wiley-Interscience, 1972). *Translated from Russian: Vliyanie Sredy na Elektromagnitnye Protsessy Pri Vysokikh Energiyakh*, Erevan: IzdAN ArmSSR, (1969).
- 168. V. G. Baryshevsky, V. A. Danilov, O. L. Ermakovich, *et al.*, "Angular distribution of parametric x-rays," Phys. Lett. A **110**, 477–479 (1985).
- 169. I. D. Feranchuk and A. V. Ivashin, "Theoretical investigation of the parametric x-ray features," J. Phys. France **46**, 1981–1986 (1985).
- 170. A. V. Shchagin, V. I. Pristupa, and N. A. Khizhnyak, "A fine structure of parametric x-ray radiation from relativistic electrons in a crystal," Phys. Lett. A **148**, 485–488 (1990).
- 171. H. Nitta, "Kinematical theory of parametric x-ray radiation," Phys. Lett. A **158**, 270–274 (1991).
- 172. A. Caticha, "Quantum theory of the dynamical Cherenkov emission of X rays," Phys. Rev. B **45**, 9541–9550 (1992).
- 173. I. Endo, M. Harada, T. Kobayashi, *et al.*, "Parametric x radiation from thick crystals," Phys. Rev. E Stat. Phys. Plasmas Fluids Relat. Interdiscip. Top. **51**, 6305–6308 (1995).
- 174. S. Asano, I. Endo, M. Harada, *et al.*, "How intense is parametric x radiation?" Phys. Rev. Lett. **70**, 3247–3250 (1993).
- 175. V. V. Morokhovskii, K. H. Schmidt, G. Buschhorn, *et al.*, "Polarization of parametric X radiation," Phys. Rev. Lett. **79**, 4389–4392 (1997).
- 176. A. V. Shchagin, "Linear polarization of parametric x-rays," Phys. Lett. A **247**, 27–36 (1998).
- 177. H. Nitta, "Dynamical effect on parametric x-ray radiation," J. Phys. Soc. Jpn. **69**, 3462–3465 (2000).
- 178. D. Pugachov, G. Buschhorn, R. Kotthaus, *et al.*, "Polarization properties of coherent polarization radiation of relativistic electrons in a crystal," Phys. Lett. A **286**, 70–75 (2001).

- 179. P. Rullhusen, X. Artru, and P. Dhez, *Novel Radiation Sources Using Relativistic Electrons: From Infrared to X-Rays* (World Scientific, 1998), Vol. **4**.
- K.-H. Brenzinger, C. Herberg, B. Limburg, et al., "Investigation of the production mechanism of parametric x-ray radiation," Z. Phys. A: Hadrons Nucl. 358, 107–114 (1997).
- 181. A. V. Shchagin and X. K. Maruyama, *Parametric X-Rays, in Accelerator-Based Atomic Physics Techniques and Applications*, edited by S. M. Shafroth and J. C. Austin (AIP, 1997), pp. 279–307.
- 182. B. Sones, Y. Danon, and R. C. Block, "Lithium fluoride (LiF) crystal for parametric x-ray (PXR) production," Nucl. Instrum. Methods Phys. Res. B **227**, 22–31 (2005).
- 183. B. Sones, Y. Danon, and R. C. Block, "X-ray imaging with parametric x-rays (PXR) from a lithium fluoride (LiF) crystal," Nucl. Instrum. Methods Phys. Res. A **560**, 589–597 (2006).
- 184. B. A. Sones, *Production of Intense, Tunable, Quasi-Monochromatic X-Rays Using the RPI Linear Accelerator*, Ph.D. thesis (2004).
- 185. Y. Hayakawa, I. Sato, K. Hayakawa, *et al.*, "Simulations to the project of a PXR based x-ray source composed of an electron linac and a double-crystal system," Nucl. Instrum. Methods Phys. Res. B **227**, 32–40 (2005).
- 186. Y. Hayakawa, I. Sato, K. Hayakawa, *et al.*, "Status of the parametric x-ray generator at LEBRA, Nihon University," Nucl. Instrum. Methods Phys. Res. B **252**, 102–110 (2006).
- 187. Y. Hayakawa, I. Sato, K. Hayakawa, *et al.*, "Tunable monochromatic X-ray source based on parametric X-ray radiation at LEBRA, Nihon University," AIP Conf. Proc. **879**, 123 (2007).
- 188. Z. Parsa and A. V. Shchagin, "Parametric x-ray radiation as source of pulsed, polarized, monochromatic, tunable x-ray beam," in *AIP Conference Proceedings* (American Institute of Physics, 1997), Vol. **396**, pp.135–143.
- 189. Y. Takabayashi, "Parametric x-ray radiation as a beam size monitor," Phys. Lett. A **376**, 2408–2412 (2012).
- 190. Y. Takabayashi and K. Sumitani, "New method for measuring beam profiles using a parametric x-ray pinhole camera," Phys. Lett. A **377**, 2577–2580 (2013).
- 191. A. V. Shchagin, "Focusing of parametric x-ray radiation," J. Exp. Theor. Phys. Lett. **80**, 469–473 (2004).
- 192. A. V. Shchagin, N. A. Khizhnyak, R. B. Fiorito, *et al.*, "Parametric x-ray radiation for calibration of x-ray space telescopes and generation of several x-ray beams," Nucl. Instrum. Methods Phys. Res. B **173**, 154–159 (2001).
- 193. A. V. Shchagin, V. M. Sanin, V. V. Sotnikov, *et al.*, "Location of heavy elements by monochromatic x-ray beam," Problems of Atomic Science and Technology, Series Nuclear Physics Investigations **42**, 194 (2004).
- 194. A. V. Shchagin, "Possibilities for measurement of nano-crystallites size with use of parametric x-ray radiation," in *Journal of Physics: Conference Series* (IOP Publishing, 2010), Vol. **236**, p. 012020.
- 195. Y. N. Adishchev, V. V. Kaplin, A. P. Potylitsin, *et al.*, "Influence of Kα absorption in (111) Ge crystal on spectral yield of parametric x-rays," Phys. Lett. A **147**, 326–328 (1990).
- 196. I. Endo, D. Iseki, T. Ohnishi, *et al.*, "On the origin of mysterious x-ray spectral peaks observed at the REFER electron ring," Nucl. Instrum. Methods Phys. Res. B **217**, 666–670 (2004).
- 197. Y. Takabayashi, I. Endo, K. Ueda, *et al.*, "Observation of intense PXR from textured polycrystal," Nucl. Instrum. Methods Phys. Res. B **243**, 453–456 (2006).
- 198. E. A. Bogomazova, B. N. Kalinin, G. A. Naumenko, et al., "Diffraction of real

- and virtual photons in a pyrolytic graphite crystal as source of intensive quasi-monochromatic x-ray beam," Nucl. Instrum. Methods Phys. Res. B **201**, 276–291 (2003).
- 199. R. B. Fiorito, D. W. Rule, X. K. Maruyama, *et al.*, "Observation of higher order parametric x-ray spectra in mosaic graphite and single silicon crystals," Phys. Rev. Lett. **71**, 704–707 (1993).
- 200. K. Y. Amosov, M. Y. Andreyashkin, V. A. Verzilov, *et al.*, "Parametric X-radiation in a mosaic crystal of pyrolytic," JETP Lett. C/C of Pis'ma V Zhurnal Eksperimental'noi Teoreticheskoi Fiziki **60**, 518 (1994).
- 201. Y. Takabayashi, K. B. Korotchenko, Y. L. Pivovarov, *et al.*, "Angular distributions of parametric x-ray radiation from a diamond crystal," Nucl. Instrum. Methods Phys. Res. B **402**, 79–82 (2017).
- 202. Y. N. Adischev, S. N. Arishev, A. V. Vnukov, *et al.*, "Angular distribution of x-ray radiation by 500 MeV electrons in a tungsten crystal," Nucl. Instrum. Methods Phys. Res. B **201**, 114–122 (2003).
- 203. B. Sonesi, Y. Danon, and E. Blain, "Feasibility studies of parametric x-rays use in a medical environment," AIP Conf. Proc. **1099**, 468 (2009).
- 204. S. Blazhevich, A. Chepurnov, V. Grishin, *et al.*, "Polarization bremsstrahlung of relativistic electrons in aluminium," Phys. Lett. A **254**, 230–232 (1999).
- 205. V. P. Afanasenko, V. G. Baryshevsky, O. T. Gradovsky, *et al.*, "Detection of parametric x-ray radiation of a GaAs monocrystal," Phys. Lett. A **141**, 311–313 (1989).
- 206. V. G. Baryshevsky, I. D. Feranchuk, and A. P. Ulyanenkov, "*Interpretation of Experimental Results BT—Parametric X-Ray Radiation in Crystals: Theory, Experiment and Applications*," edited by V. G. Baryshevsky, I. D. Feranchuk, and A. P. Ulyanenkov, eds. (Springer, 2005), pp. 73–104.
- 207. I. Lobach, A. Benediktovitch, I. Feranchuk, *et al.*, "Parametric x-rays from a polycrystalline target," Nucl. Instrum. Methods Phys. Res. B **360**, 75–80 (2015).
- V. I. Alekseev, A. N. Eliseev, E. F. Irribarra, *et al.*, "Diagnostics of nanodisperse polycrystals based on the polarization bremsstrahlung of relativistic electrons,"
   J. Surf. Invest.: X-Ray, Synchrotron Neutron Tech. 8, 347–350 (2014).
- 209. V. V. Kaplin, S. R. Uglov, V. V. Sohoreva, *et al.*, "Parametric x-rays generated by electrons in multilayer mirrors mounted inside a betatron," Nucl. Instrum. Methods Phys. Res. B **267**, 777–780 (2009).
- 210. B. A. Sones, "Production of Intense, Tunable, Quasi-Monochromatic X-Rays Using the RPI Linear Accelerator," Ph.D. Thesis (2004).
- 211. I. D. Feranchuk, A. Ulyanenkov, J. Harada, *et al.*, "Parametric x-ray radiation and coherent bremsstrahlung from nonrelativistic electrons in crystals," Phys. Rev. E Stat. Phys. Plasmas Fluids Relat. Interdiscip. Top. **62**, 4225–4234 (2000).
- 212. V. G. Baryshevsky, K. G. Batrakov, I. D. Feranchuk, *et al.*, "Coherent bremsstrahlung and parametric x-ray radiation from nonrelativistic electrons in a crystal," Tech. Phys. Lett. **32**, 392–395 (2006).
- 213. T. S. Curry, J. E. Dowdey, and R. C. Murry, *Christensen's Physics of Diagnostic Radiology* (Lippincott Williams Wilkins, 1990).
- 214. P. A. Prosekov, V. L. Nosik, and A. E. Blagov, "Methods of coherent x-ray diffraction imaging," Crystallogr. Rep. 66, 867–882 (2021).
- 215. S. Marchesini, H. Chapman, S. Hau-Riege, *et al.*, "Coherent x-ray diffractive imaging: applications and limitations," Opt. Express 11, 2344–2353 (2003).
- 216. T. Li, A. J. Senesi, and B. Lee, "Small angle x-ray scattering for nanoparticle research," Chem. Rev. 116, 11128–11180 (2016).
- 217. F. de Groot, "High-resolution x-ray emission and x-ray absorption spectroscopy," Chem. Rev. **101**, 1779–1808 (2001).

- 218. Y. N. Adishchev, A. S. Artemov, S. V. Afanasiev, *et al.*, "Detection of parametric x-ray radiation from moderately relativistic protons in crystals," J. Exp. Phys. Lett. **81**, 241–244 (2005).
- 219. V. P. Afanasenko, V. G. Baryshevsky, R. F. Zuevsky, *et al.*, "Detection of proton parametric x-ray radiation in silicon," Phys. Lett. A **170**, 315–318 (1992).
- 220. A. G. Afonin, G. I. Britvich, Y. A. Chesnokov, *et al.*, "Observation of parametric x-ray radiation excited by 50 GeV protons and identification of background radiation origin," Problems of Atomic Science and Technology **86**, 315–319 (2013).
- 221. A. V. Shchagin, G. Kube, S. A. Strokov, *et al.*, "Surface-barrier detector with smoothly tunable thickness of depleted layer for study of ionization loss and dechanneling length of negatively charged particles channeling in a crystal," Nucl. Instrum. Methods Phys. Res. A **1059**, 168930 (2024).
- 222. M. L. Ter-Mikhaelyan, "Electromagnetic radiative processes in periodic media at high energies," Phys. Usp. 44, 571–596 (2001).
- 223. Y. Hayakawa, K. Hayakawa, M. Inagaki, *et al.*, "Improvement in the performance of the x-ray source based on parametric x-ray radiation using a wedge-shaped target crystal," Nuovo Cim. C **34**, 253 (2011).
- 224. R. B. Fiorito, D. W. Rule, M. A. Piestrup, *et al.*, "Polarized angular distributions of parametric x radiation and vacuum-ultraviolet transition radiation from relativistic electrons," Phys. Rev. E **51**, R2759–R2762 (1995).
- 225. A. V. Shchagin and N. A. Khizhnyak, "Differential properties of parametric x-ray radiation from a thin crystal," Nucl. Instrum. Methods Phys. Res. B **119**, 115–122 (1996).
- 226. A. Authier, *Dynamical Theory of X-Ray Diffraction* (Oxford University Press on Demand, 2004), Vol. **11**.
- 227. A. Caticha, "Transition-diffracted radiation and the Cerenkov emission of x rays," Phys. Rev. A **40**, 4322–4329 (1989).
- 228. V. G. Baryshevsky and O. M. Lugovskaj, "On parametric x-ray radiation," Phys. At. Nucl. **66**, 409–415 (2003).
- 229. A. V. Shchagin, "Areas of applicability of kinematic and dynamic theories of parametric x-ray radiation," Problems of Atomic Science and Technology **87**, 315–319 (2015).
- 230. A. V. Shchagin, "Diffraction, extraction and focusing of parametric x-ray radiation, channeling radiation and crystal undulator radiation from a bent crystal," in *Advanced Radiation Sources and Applications: Proceedings of the NATO Advanced Research Workshop*, held in Nor-Hamberd, Yerevan, Armenia, August 29–September 2, 2004 (Springer, 2006), pp. 27–45.
- 231. A. Shchagin, G. Kube, A. Potylitsyn, et al., "Doppler effect in vacuum, homogeneous, and periodical media in x-ray range," Nucl. Instrum. Methods Phys. Res. A 1072, 170235 (2025).
- 232. A. V. Shchagin, "Diffraction in forward direction of parametric x-ray radiation from relativistic particles of moderate energy," in *International Conference on Charged and Neutral Particles Channeling Phenomena II* (SPIE, 2007), Vol. **6634**, pp. 401–409.
- 233. A. V. Shchagin, V. I. Pristupa, and N. A. Khizhnyak, "Parametric x-ray radiation from relativistic electrons in a crystal in the vicinity of and at angular distance from a Bragg direction," Nucl. Instrum. Methods Phys. Res. B 99, 277–280 (1995).
- 234. S. V. Blazhevich, G. L. Bochek, V. B. Gavrikov, *et al.*, "First observation of interference between parametric x-ray and coherent bremsstrahlung," Phys. Lett. A **195**, 210–212 (1994).

- 235. V. L. Kleiner, N. N. Nasonov, and A. G. Safronov, "Interference between parametric and coherent bremsstrahlung radiation mechanisms of a fast charged particle in a crystal," Phys. Status Solidi (b) **181**, 223–231 (1994).
- 236. J. Gardelle, L. Courtois, P. Modin, *et al.*, "Observation of coherent Smith-Purcell radiation using an initially continuous flat beam," Phys. Rev. Spec. Top. Accel. Beams **12**, 110701 (2009).
- 237. Y. Neo, H. Shimawaki, T. Matsumoto, *et al.*, "Smith-Purcell radiation from ultraviolet to infrared using a Si field emitter," J. Vac. Sci. Technol. B **24**, 924–926 (2006).
- 238. S. E. Korbly, A. S. Kesar, J. R. Sirigiri, *et al.*, "Observation of frequency-locked coherent terahertz Smith-Purcell radiation," Phys. Rev. Lett. **94**, 054803 (2005).
- 239. Y. Ye, F. Liu, M. Wang, *et al.*, "Deep-ultraviolet Smith–Purcell radiation," Optica **6**, 592 (2019).
- 240. S. Tsesses, G. Bartal, and I. Kaminer, "Light generation via quantum interaction of electrons with periodic nanostructures," Phys. Rev. A **95**, 13832 (2017).
- 241. A. V. Shchagin, "Parametric x-rays at the right angle to the particle beam," Phys. Lett. A **262**, 383–388 (1999).
- 242. A. V. Shchagin, "Investigations and properties of PXR, in electron-photon interaction in dense media," edited by H. Wiedemann, *NATO Science Series, II Mathematics, Physics and Chemistry*, (Kluwer Academic Publishers, 2002), pp. 133–151.
- 243. M. L. Ter-Mikaelian, *High-Energy Electromagnetic Processes in Condensed Media* (John Wiley Sons, 1972).
- 244. K.-H. Brenzinger, B. Limburg, H. Backe, *et al.*, "How narrow is the linewidth of parametric x-ray radiation?," Phys. Rev. Lett. **79**, 2462–2465 (1997).
- 245. T. Hahn, U. Shmueli, and J. C. W. Arthur, *International Tables for Crystallography* (Reidel Dordrecht, 1983), Vol. 1.
- 246. Parametrization of F0 (the Non-Dispersive Part of the Atomic Scattering Factor) vs Sin(Theta/Lambda), https://www.classe.cornell.edu.
- 247. V. G. Baryshevsky, I. D. Feranchuk, A. O. Grubich, *et al.*, "Theoretical interpretation of parametric x-ray spectra," Nucl. Instrum. Methods Phys. Res. A **249**, 306–319 (1986).
- 248. K. Y. Amosov, B. N. Kalinin, A. P. Potylitsin, *et al.*, "Influence of temperature on parametric x-ray intensity," Phys. Rev. E **47**, 2207–2209 (1993).
- 249. H. Yamada, "Novel x-ray source based on a tabletop synchrotron and its unique features," Nucl. Instrum. Methods Phys. Res. B **199**, 509–516 (2003).
- 250. V. K. Neil, R. K. Cooper, and L. S. Hall, "Further theoretical studies of the beam breakup instability," Part. Accel. 9, 213 (1979).
- 251. Y. Tang, T. P. Hughes, C. A. Ekdahl, *et al.*, "BBU calculations for beam stability experiments on DARHT-2," in *Proceedings of the European Particle Accelerator Conference* (2006), pp. 1–23.
- 252. J. E. Coleman, D. C. Moir, C. A. Ekdahl, *et al.*, "Limitations of increasing the intensity of a relativistic electron beam," in *Proceedings of the Particle Accelerator Conference* (2013), p. 484.
- 253. V. V. Mitrochenko, "Thermionic RF gun with high duty factor," in *Proceedings* of the 1997 Particle Accelerator Conference (1997), Vol. 3, pp. 2817–2819.
- 254. H. P. Bluem, D. Dowell, A. M. M. Todd, et al., "High brightness thermionic electron gun performance," in *Proceedings of the 50th Advanced ICFA Beam Dynamics Workshop on Energy Recovery Linacs (ERL '11)* (2011).
- 255. R. W. Wood, "Note on 'focus tubes' for producing x-rays," Lond. Edinb. Dubl. Phil. Mag. J. Sci. 41, 382–383 (1896).

- 256. E. Krestel, *The X-Ray Tube*, in *Imaging Systems for Medical Diagnostics* (Siemens Aktiengesellschaft, 1990), pp. 222–246.
- 257. J. Hrdý, "Double crystal monochromator for synchrotron radiation with decreased radiation power density," Rev. Sci. Instrum. **63**, 459–460 (1992).
- 258. J. H. Hubbell and S. M. Seltzer, *Tables of X-Ray Mass Attenuation Coefficients and Mass Energy-Absorption Coefficients 1 KeV to 20 MeV for Elements Z= 1 to 92 and 48 Additional Substances of Dosimetric Interest* (National Inst. of Standards and Technology-PL, 1995).
- 259. H. A. Bethe, "Molière's theory of multiple scattering," Phys. Rev. **89**, 1256–1266 (1953).
- 260. J. Beringer, J. F. Arguin, R. M. Barnett, et al., Phys. Rev. D 86, 010001 (2012).
- 261. V. G. Baryshevskii, A. O. Grubich, and L. T. Hai, "The effect of multiple scattering on parametric x-rays," *Zh. Eksp. Teor. Fiz.* **94**, 51 (1988).
- 262. A. P. Potylitsin, "Influence of beam divergence and crystal mosaic structure upon parametric x-ray radiation characteristics," arXiv (1994).
- 263. H. Koziol, Beam Diagnostics for Accelerators, CERN (2001).
- 264. U. Iriso, G. Benedetti, and F. Perez, "Experience with YAG and OTR screens at ALBA, DIPAC 2009," 9th European Workshop on Beam Diagnostics and Instrumentation for Particle Accelerators (JACoW Publishing, 2009).
- 265. M. Johnson and D. Mcnabb, Comparison of Techniques to Reduce Bremsstrahlung Background Radiation from Monoenergetic Photon Beams, Report No. UCRL-TR-222530 (2006).
- 266. J. Rubio-Zuazo, V. Collado-Negro, C. Heyman, *et al.*, "A double crystal x-ray monochromator for the SpLine diffraction and absorption synchrotron bending magnet beamline at the ESRF," J Phys Conf Ser **425**, 052005 (2013).
- 267. M. Okui, N. Yato, A. Watanabe, *et al.*, "Double crystal monochromator controlled by integrated computing on BL07A in New SUBARU, Japan," *AIP Conference Proceedings* (2016), Vol. **1741**, p. 30033.
- 268. A. Souvorov, M. Drakopoulos, A. Freund, *et al.*, "Fixed exit double-crystal monochromator with one single cooled crystal," Nucl. Instrum. Methods Phys. Res. A **413**, 427–430 (1998).
- 269. J. Rubio-Zuazo, V. Collado-Negro, C. Heyman, *et al.*, "A double crystal x-ray monochromator for the SpLine diffraction and absorption synchrotron bending magnet beamline at the ESRF," J. Phys. Conf. Ser. **425**, 052005 (2013).
- 270. W. Guan, A. Lockwood, B. J. Inkson, *et al.*, "A piezoelectric goniometer inside a transmission electron microscope goniometer," Microsc. Microanal. **17**, 827–833 (2011).
- 271. M. de Bruin, "Glossary of terms used in nuclear analytical chemistry," Pure Appl. Chem. **54**, 1533–1554 (1982).
- 272. A. G. Michette and C. J. Buckley, *X-Ray Science and Technology* (Institute of Physics, 1993).
- 273. L. Martins, P. Amaro, S. Pessanha, *et al.*, "Overview and calculation of x-ray K-shell transition yields for comprehensive data libraries," X-Ray Spectrom. **49**, 398–423 (2020).
- 274. A. K. Jaradat and P. J. Biggs, "Measurement of the neutron leakage from a dedicated intraoperative radiation therapy electron linear accelerator and a conventional linear accelerator for 9, 12, 15(16), and 18(20) MeV electron energies," Med. Phys. **35**, 1711–1717 (2008).
- 275. V. G. Baryshevsky, "Spontaneous and induced radiation by electrons/positrons in natural and photonic crystals. Volume free electron lasers (VFELs): from microwave and optical to x-ray range," Nucl. Instrum. Methods Phys. Res. B **355**, 17–23 (2015).

- 276. V. G. Baryshevsky, "Klystron type crystal-based x-ray volume free electron laser," Phys. Rev. Accel. Beams 27, 120701 (2024).
- 277. A. Shchagin, "Excitation of evanescent wave by parametric x-ray radiation," in 5th International Conference on Charged and Neutral Particle Channeling Phenomena (2012), p. 97.



Amnon Balanov is a Ph.D. student in the School of Electrical Engineering at Tel Aviv University. His research addresses theoretical and computational challenges in structural biology, with a particular focus on cryo-electron microscopy (cryo-EM) and the statistical and algorithmic foundations of single-particle reconstruction. He earned a B.Sc. in Computer Engineering, Mathematics, and Physics (2014) and an M.Sc. in Electrical Engineering (2024) from the Technion—Israel Institute of Technology. His master's research focused on the

design of compact and tunable x-ray sources, drawing on concepts from laser physics, free electron—matter interactions, and crystal-based radiation. He is motivated by fundamental interdisciplinary problems at the intersection of applied mathematics, physics, and engineering.



Alexey Gorlach is a physicist and doctoral candidate at the Technion—Israel Institute of Technology, specializing in quantum optics and nanophotonics. He holds an undergraduate degree in theoretical physics from Belarusian State University and is currently pursuing a Ph.D. in nanotechnology and nanoscience at the Technion. Gorlach's research focuses on high-harmonic generation, photoninduced near-field electron microscopy, and the development of quantum light sources. His work has been published in prominent

scientific journals, including *Nature Physics* and *Physical Review Letters*. He has coauthored influential studies on quantum-optical effects in extreme nonlinear optics and free-electron quantum optics.



**Vladimir G. Baryshevsky** is a Belarusian physicist and the founding director of the Research Institute for Nuclear Problems at Belarusian State University, where he currently holds the position of principal research scientist. He earned his Ph.D. in 1965 and his Doctor of Science degree in 1974 and was appointed professor in 1977. Renowned for his groundbreaking work in nuclear optics, high-energy physics, and the electromagnetic radiation of relativistic particles in natural and photonic crystals, he founded the scien-

tific school of Nuclear Optics of Polarized Media. He has authored over 400 scientific papers and several influential monographs. His accomplishments include two officially registered scientific discoveries in the USSR and numerous national awards, among them the State Prize of the Republic of Belarus in Science and Technology.



**Ilya D. Feranchuk** is a theoretical physicist and professor at the Belarusian State University, where he has served since 1974 and headed the Department of Theoretical Physics and Astrophysics from 2002 to 2017. He received his degree in nuclear physics from BSU in 1969 and became a full professor in 1986. His research spans quantum electrodynamics, coherent radiation processes in crystals, and non-perturbative methods in quantum theory. Notably, he co-predicted the phenomenon of parametric x-ray radiation from

relativistic particles in crystals. Professor Feranchuk has authored over 270 scientific

publications and several monographs, and his work has been recognized with the State Prize of the Republic of Belarus in Science and Technology.



**Hideo Nitta** is Professor Emeritus of Physics and Specially Appointed Professor at Tokyo Gakugei University. His research interests lie in theoretical physics, with a focus on radiation physics and the foundations of quantum mechanics. In recent years, he has been actively engaged in physics education and educational research. He has served as committee member, vice-chair, and chair of the IU-PAP Commission on Physics Education (C14), and currently serves as President of the Physics Education Society of Japan.



Yasushi Hayakawa is a professor affiliated with the Institute of Quantum Science at Nihon University and the administrator of the Laboratory for Electron Beam Research and Application (LEBRA). He received a Doctor of Science from Kyoto University in 1998, followed by a position at Nihon University. He studied and designed a double-crystal system for a novel x-ray source based on parametric x-ray radiation (PXR); the first light of PXR from the source was observed in 2004. He has been involved in the development of PXR

applications while providing PXR beams for users studies. In particular, he has successfully demonstrated analyzer-based x-ray imaging techniques using PXR beams, which is one of the major applications of PXR at the LEBRA facility.



**Alexander V. Shchagin** is a Ukrainian physicist holding the degree of Candidate of Physical-Mathematical Sciences (equivalent to a Ph.D.), awarded by Moscow State University in 2002 for his dissertation on the differential properties of parametric x-ray radiation. He is a senior scientist at the Kharkiv Institute of Physics and Technology (Ukraine) and a researcher at Deutsches Elektronen-Synchrotron (DESY) in Hamburg, Germany. His research spans nuclear physics, parametric and characteristic x-ray radiation, ioniza-

tion losses of relativistic particles, optical and x-ray transition radiation, and the development of pyroelectric and piezoelectric particle and x-ray sources. He has contributed to the DARKSIDE collaboration in the search for dark matter. Dr. Shchagin has collaborated with scientists from the USA, Canada, Japan, France, Germany, the UK, Russia, Armenia, and Ukraine, and has over 100 peer-reviewed publications.



**Yuichi Takabayashi** is a Chief Researcher at the SAGA Light Source in Japan. He received a Ph.D. in Physics from the University of Tokyo in 2002, following the completion of his M.S. and B.S. degrees at the same university in 1999 and 1997, respectively. From 2002 to 2004, he was a postdoctoral fellow at Hiroshima University, Japan. His research interests lie in accelerator and radiation physics, with a particular focus on synchrotron radiation, undulator radiation, channeling radiation, parametric x-ray radiation, transi-

tion radiation, edge radiation, and Cherenkov radiation. Additionally, he is involved in investigating optical vortices (orbital angular momentum) produced by these types of radiation.



Yaron Danon, Edward E. Hood Jr. Chair in Nuclear Engineering at Rensselaer Polytechnic Institute (RPI), directs the Nuclear Engineering Program and the Gaerttner Electron Linear Accelerator (LINAC) Center, specializing in neutron-induced reactions and nuclear data measurement. His research advances novel radiation detectors and pyroelectric crystal-based accelerators, pioneering x-ray and neutron sources powered by crystal heating. With over 240 peer-reviewed publications, he mentors graduate students and

teaches courses on radiation technology, linear accelerators, and nuclear reactor physics.



Liang Jie Wong is an Associate Professor in the School of Electrical and Electronic Engineering at Nanyang Technological University, Singapore. He earned his Ph.D. and M.Sc. degrees in Electrical Engineering and Computer Science from the Massachusetts Institute of Technology (MIT) and his B.S. in the same field from the University of California, Berkeley. A former National Science Scholar and postdoctoral fellow in MIT's Department of Mathematics, Dr. Wong was awarded the prestigious Nanyang Assistant

Professorship and the MOE Inauguration Grant START Award in 2019. In 2024, he was recognized as one of ten Global Winners in the Physical Sciences category of the Falling Walls Breakthrough of the Year Awards. His research centers on x-ray photonics and free electron-driven quantum science. He also serves as Deputy Director of the CN Yang Scholars Programme, Associate Editor of *Optics Express*, and Technical Committee Member of CLEO USA and was an elected member of the NTU School Board from 2022 to 2024.



**Ido Kaminer** is a physicist and electrical engineer at the Technion—Israel Institute of Technology, where he leads the AdQuanta Lab in the Faculty of Electrical and Computer Engineering. His research lies at the intersection of photonics, quantum optics, and free-electron physics, with a focus on light–matter interactions at ultrafast and quantum scales. He earned his B.Sc. in Electrical Engineering and Physics and his Ph.D. in Physics from the Technion, and completed a postdoctoral fellowship at MIT. Prof. Kaminer is

known for pioneering work in free-electron quantum optics and macroscopic quantum electrodynamics, and his research has been recognized with numerous awards, including the Blavatnik Award in Physical Sciences Engineering (Israel, 2021), the Adolph Lomb Medal (2022), the Schmidt Science Polymath Award (2022), and the Stanisław Lem European Research Prize (2023). He is a member of the Israeli Young Academy.